國立臺灣大學電機資訊學院電機工程學系

碩士論文

Department of Electrical Engineering
College of Electrical Engineering and Computer Science
National Taiwan University

Master Thesis

應用於表面式永磁同步馬達故障情境之功率硬體迴路模擬

Power Hardware-in-the-Loop Emulation for Surface Permanent Magnet Synchronous Motor Under Fault Scenarios

鍾佳銘
Jia-Ming Zhong

指導教授：陳耀銘 博士
Advisor: Yaow-Ming Chen, Ph.D.

中華民國 112 年 6 月

June 2023

doi:10.6342/NTU202302551

國立臺灣大學碩士學位論文
口試委員會審定書
MASTER'S THESIS ACCEPTANCE CERTIFICATE
NATIONAL TAIWAN UNIVERSITY

應用於表面式永磁同步馬達故障情境

之功率硬體迴路模擬

Power Hardware-in-the-Loop Emulation for Surface Permanent Magnet Synchronous Motor Under Fault Scenarios

本論文係 鍾佳銘 君（學號 R10921025）在國立臺灣大學電機工程學系完成之碩士學位論文，於民國112 年 6月 29日承下列考試委員審查通過及口試及格，特此證明。

The undersigned, appointed by the Department of Electrical Engineering on 29th June, 2023 have examined a Master's thesis entitled above presented by Jia-Ming, Zhong (student ID R10921025) candidate and hereby certify that it is worthy of acceptance.

口試委員 Oral examination committee:

張淵智　楊士進

陳昇然　陳耀銘

（指導教授 Advisor）

系主任 Director: 李建模

致謝

在回顧過去的兩年光陰時，心中充滿著複雜的情緒。有歡笑和喜悅，也有失落和悔恨。但沒有痛苦與悲傷，因為我知道我做了對的決定，那就是來到 EEPro。

在這段時光裡，首先要感謝的就是實驗室的大家長，指導教授陳耀銘博士。謝謝您總會要求我要好好地思考自己到底想要什麼，也給了我最大限度的自由，讓我可以利用實驗室的資源去做自己想做的事。且不論是什麼事，您都給予了我最大的支持和認同，這讓我對前進不再迷惘，也因此我才能在實驗室不斷成長精進自己。

感謝就讀博士班的承戰學長和嘉洲學長。尤其是嘉洲學長，基本上從我進實驗室後您就一直都是我的直屬學長，台達計畫的大小事都是由您手把手將我提拔上來的。而之後我在做自己的研究時也多次受到學長的幫忙，真的非常謝謝你的指教，祝你以後能找到發揮你電機跟大氣專業的工作。

感謝碩士班畢業的哲彥、訢甯與承翰。尤其是承翰，在學時常與我分享各種我從來就沒聽過的跨領域知識，畢業後在我向您求救時，也能替我解答問題。我只能說在我心中你永遠是我大哥，也是我心中最接近周世宗柴榮的存在，希望你的理想與抱負能在不久後的將來實現。

感謝即將去英國發展的昇翰，雖然您不是實驗室的成員，但在我眼裡您早就是我碩班期間中不可或缺的一份子。這兩年來時常受到您的照顧，研究上面不用講，您給予的意見對我而言都是非常棒的回饋。還有就是包含業界工作以及出國念博的各種資訊與經驗分享，真的是讓我受益良多。

感謝實驗室的快樂伙伴們學儒、文彥、志誠、明圜、芳儀、子萱、啟元、建亨，正因有你們在，讓我枯燥的研究生活瞬間變得有趣了起來。且不管在學業上抑或是各種神奇事情上都給了我很大的啟發。跟你們在實驗室討論時我常常會感受到自己的無知，而這份情感最終也轉變成了我努力精進自己的原動力之一。

感謝我高中及大學甚至到了研究所都同一所學校的芊穎，一直以來在我心情低落或者是對未來迷惘的時候，都能當我最好的討論對象。不管是跟你出去吃飯或喝酒的時光，都讓我難以忘懷。希望未來你能過著你想過的生活，能活出你想要的人生，"黑皮"的度過每一天。

最後，要謝的人還有一直在背後默默支持我的父母親以及願意撥冗參加論文口試的各個評審委員們，只能說要感謝的人太多了，不如謝天吧。

doi:10.6342/NTU202302551

中文摘要

本論文主旨在於使用功率硬體迴路(Power Hardware-in-the-Loop, PHIL)技術，實現對於表面式永磁同步馬達(Surface Permanent Magnet Synchronous Motor, SPMSM)在不同故障情境下的實時模擬。論文主要分為兩個部份，第一部分是針對SPMSM 常見的故障情境，包含電阻不平衡(Resistance Unbalance, R-Unbalance)、欠相故障(Open-Phase Fault, OPF)以及匝間短路故障(Inter-Turn Short-Circuit Fault, ISCF)，進行模型的建立以及簡化。

第二部分則是當待測馬達驅動器(Motor driver Under Test, MUT)使用磁場導向控制(Field-Oriented Control, FOC)時， PHIL 會經由故障情境之馬達模型產生具有諧波成分的參考電流。由於此參考電流無法只透過比例積分(Proportional-Integral; PI)控制器達成無穩態誤差，因此本文提出了具耦合項之比例積分諧振(Coupling-Proportional-Integral-Resonant, CPIR)控制器，以改善 PHIL 電流控制器的效能。

最後，這些論述的成果將透過 MATLAB & Simulink 模擬進行初步驗證，並同時在硬體實驗上取得相對應的成果，以證明實作及模擬皆與理論相符。本論文從實測數據驗證了 PHIL 在使用 CPIR 控制後，直交軸上兩倍頻電流的誤差在 R-Unbalance 情境下從 17.64%降到 0.43%，在 OPF 情境下從 17.21%降到 0.39%，在 ISCF 情境下從 15.70%降到 0.47%。另外，實測結果的三相電流及數值模擬的三相電流之均方根誤差(Root-Mean-Square Error, RMSE)，在使用了 CPIR 控制後，R-Unbalance 情境下從 18.31%降到 14.36%，OPF 情境下從 17.21%降到 7.94%，ISCF 情境下從 20.29%降到 18.34%。此外，為了公正評估 PHIL 模擬實際馬達的能力，本論文提出了使用總諧波失真再加上雜訊(Total Harmonic Distortion plus Noise,THD+N)來進行計算的相似指數(Simularity Index, SI)。透過 SI 可比較實測結果的三相電流以及數值模擬的三相電流的相似程度。在使用了 CPIR 控制後，R-Unbalance 情境下 SI 從 86.42%升到 97.33%，OPF 情境下 SI 從 55.64%升到 84.31%，ISCF 情境下 SI 從 61.43%升到 64.07%。透過上述三種比較數據可驗證使用 CPIR 控制的 PHIL 在故障情境下的實時模擬效能。

關鍵字：功率硬體迴路、電子式馬達模擬器、動態馬達模擬器、永磁同步馬達、電阻不平衡、欠相故障、匝間短路故障、馬達驅動器、磁場導向控制

doi:10.6342/NTU202302551

ABSTRACT

The objective of this thesis is to realize the emulation of Surface Permanent Magnet Synchronous Motor (SPMSM) under different fault scenarios using Power Hardware-in-the-Loop (PHIL) technology. This thesis is divided into two main parts. The first part involves the development and simplification of models for common SPMSM fault scenarios, including Resistance Unbalance(R-Unbalance), Open-Phase Fault (OPF), and Inter-Turn Short-Circuit Fault (ISCF).

The second part focuses on the emulation of faulty motors using a Motor Driver Under Test (MUT) with Field-Oriented Control (FOC). The motor model considering fault conditions generates the reference currents with harmonic components, where the conventional Proportional-Integral (PI) control cannot achieve zero steady-state error. To improve the performance of the PHIL current control, this thesis proposes a new method called Coupling-Proportional-Integral-Resonant (CPIR) control.

Finally, the derived PMSM fault models and the proposed CPIR control are preliminarily verified using MATLAB & Simulink simulations. Also, hardware experiments are conducted to validate that both simulation and experiment results are consistent. Furthermore, this thesis provides a comprehensive analysis of the error at second order harmonic of the controller. It is evident that the implementation of CPIR control leads to a significant reduction in the error at second order harmonic in various fault scenarios. Specifically, in the case of R-Unbalance scenario, the error drops from 17.64% to 0.43%, in the OPF scenario, it decreases from 17.21% to 0.39%, and in the ISCF scenario, it diminishes from 15.70% to 0.47%. Additionally, a comparison is conducted between the root-mean-square errors (RMSE) of the three-phase current measured from hardware experiments and the three-phase current obtained from

doi:10.6342/NTU202302551

numerical simulation. The results demonstrate notable improvements with the application of CPIR control. In the R-Unbalance scenario, RMSE decreases from 18.31% to 14.36%, in the OPF scenario, it drops from 17.21% to 7.94%, and in the ISCF scenario, it goes from 20.29% to 18.34%. To further assess the effectiveness of the PHIL-based motor test-bench, this thesis proposes the use of the Similarity Index (SI), calculated based on the Total Harmonic Distortion plus Noise (THD+N), to quantify the similarity between the three-phase currents of experimental and numerical simulation. The results reveal substantial enhancements in similarity with the adoption of CPIR control. In the R-Unbalance scenario, the SI increases from 86.42% to 97.33%, in the OPF scenario, the SI rises from 55.64% to 84.31%, and in the ISCF scenario, it elevates from 61.43% to 64.07%. These three hardware result comparisons confirm the effectiveness of PHIL under fault scenarios.

Keywords: Power hardware-in-the-loop (PHIL), Electric motor emulator (EME), Dynamic motor emulator (DME), Permanent magnet synchronous motor (PMSM), Resistance unbalance (R-Unbalance), Open-phase fault (OPF), Inter-turn short-circuit fault (ISCF), Motor driver, Field-oriented control (FOC)

doi:10.6342/NTU202302551

Table of Contents

doi:10.6342/NTU202302551

doi:10.6342/NTU202302551

doi:10.6342/NTU202302551

List of Figures

doi:10.6342/NTU202302551

doi:10.6342/NTU202302551

doi:10.6342/NTU202302551

doi:10.6342/NTU202302551

doi:10.6342/NTU202302551

doi:10.6342/NTU202302551

doi:10.6342/NTU202302551

doi:10.6342/NTU202302551

doi:10.6342/NTU202302551

List of Tables

doi:10.6342/NTU202302551

Chapter 1 Introduction

1.1 Background

Power Hardware-in-the-Loop (PHIL) is a technology that allows engineers to evaluate the dynamic performance of a physical system, especially for electric motor, without using the real physical system. By using PHIL instead of the real motor, several advantages can be obtained. First, PHIL can achieve energy recovering by utilizing common-DC-bus structure, which means that the total loss of energy is highly reduced by using PHIL. For applications such as burn-in test, performing the test with PHIL is a great alternative to a real motor from the perspective of saving energy. Second, PHIL offers substantial time and cost savings in the testing and validation of real-world electromechanical systems. By providing a virtual motor, engineers can quickly and easily test different scenarios and configurations without wasting time to replace the specific machine. Third, PHIL allows engineers to conduct comprehensive tests on complex electromechanical systems, including challenging scenarios like fault conditions, transient response analysis to sudden load changes, and evaluation of system behavior under extreme environmental conditions. Such tests may not be feasible or safe to conduct on the physical system due to the risk of damage, potential safety issues, or the high building cost of the systems for special purpose. With the discussion above, it can be concluded that PHIL technology offers a more efficient, cost-effective, and secure approach to testing. That is also why PHIL is a blooming research topic in the Power Electronics area.

The block diagram in Fig. 1.1 illustrates a motor drive test-bench using PHIL technology. In this test-bench, the motor drive being tested is referred to as the Motor Driver Under Test (MUT), while the PHIL serves as the electronic testing equipment.

doi:10.6342/NTU202302551

The PHIL can be divided into four main components.

First, the power stage is the primary part of the PHIL that is responsible to produce an output voltage that controls the flow of currents through the coupling network, allowing for precise emulation of the reference currents calculated by the motor model, and the power stage draws the power from the MUT. Second, the coupling network is responsible for separating the power stage of PHIL from the MUT, while also working as the control plant for the PHIL. Additionally, different topologies of coupling network may reduce current harmonics and increase the accuracy of emulation. Next, the voltage signals sensed at the interface are transmitted to the motor model. Based on the mathematical model of the selected scenario, the motor model calculates the reference currents, such as dq-axis currents, for the current control. The motor model also generates additional information about the motor, such as angular velocity and rotor angle. Lastly, the current controller generates gate signals that control the power stage, enabling the PHIL to emulate the behavior of a motor based on the commands calculated by the motor model.

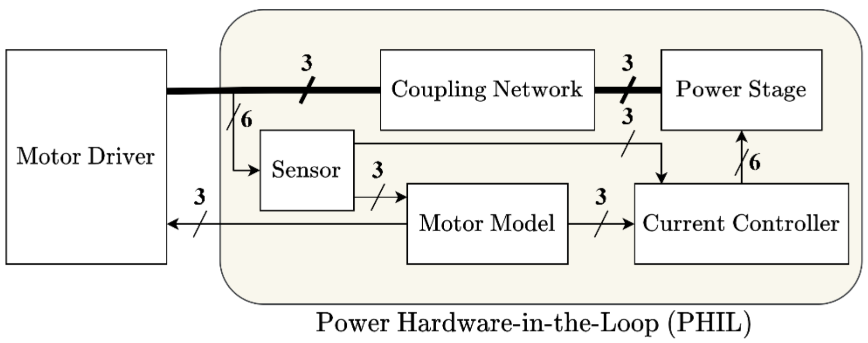

Fig. 1.1 The block diagram of PHIL-based motor test-bench.

1.2 Paper review and Motivation

Nowadays, research in the field of PHIL can be roughly categorized into three areas: power stage topologies, control system, and modeling for different types of motors and

doi:10.6342/NTU202302551

mechanical load conditions.

First, the power stage of the PHIL is commonly implemented using a three-phase three-wire inverter due to its simplicity, as noted in [1], [2]. However, to ensure the power stage can operate under all possible scenarios, the power rating of the PHIL must be equal to or higher than that of the motor driver. To achieve this, researchers have proposed various improvements. For instance, in [3], a multilevel inverter for PHIL implementation is presented, while [4] proposes the adoption of multilevel double-star chopper-cell inverter for PHIL.

Next, there are two different aspects for the control system in the PHIL: coupling network, which is the control plant for the PHIL, and the controller. For the coupling network, RL filter is the most commonly-used topology in the PHIL, as noted in [5]. However, to further reduce the current harmonics produced by the inverter of PHIL, other coupling network topologies such as LC filter, LCL filter, and transformer-based coupling network are discussed in [6]. For the controller, the well-known decoupling Proportional-Integral (PI) control in dq frame is the most used and easy way to implement. To eliminate the nonlinear effect of different coupling network, state feedback linearization and coupling network state equation control are adopted, as noted in [1].

Last, the modeling of different motors, such as PMSM, reluctance motor, and induction motor are presented in [8]-[10]. Moreover, different mechanical load conditions are discussed in [11]-[13]. However, there are just a few papers discuss about the fault scenario, as noted in [14] and [15], and the implementation of the fault emulation usually requires a look-up table, which makes the calculation of the motor model complicated.

Therefore, the objective of this thesis is to implement the simplified dynamic models of various faults through numerical method to compute the reference currents, and to propose a new control that enhances the performance compared to the traditional one.

doi:10.6342/NTU202302551

1.3 Outline

This thesis can be divided into six chapters and an appendix, where the contents of each sections can be briefly described as follows:

In Chapter 2, Surface Permanent Magnet Synchronous Motor (SPMSM) is first introduced. The dq-axis SPMSM model is derived by utilizing the Park Transform. This chapter provides an overview of different common faulty motor scenarios and presents derivations for each scenario. These scenarios include Resistance Unbalance (R-Unbalance), Open-Phase Fault (OPF), and Inter-Turn Short-Circuit Fault (ISCF).

In Chapter 3, the PHIL control plant in dq-axis is derived in the first part. Afterward, a design procedure for the traditional decoupling PI control is provided. Then, the basic concepts of Dual Synchronous Reference Frame (DSRF) control and the derivation of the proposed Coupling-Proportional-Integral-Resonant (CPIR) control is presented. Eventually, how to digitalize and implement the controllers used in the proposed CPIR control is shown in the last part.

In Chapter 4, the simulation environment of the motor driver test-bench using PHIL is introduced. More importantly, the simulation results for different scenarios using PI and CPIR control are shown.

In Chapter 5, the implementation of the motor driver test-bench using PHIL, including hardware and firmware development, is presented. Afterward, the experiment results for different scenarios using PI and CPIR control are shown.

In Chapter 6, the achievements of this thesis are briefly summarized. Besides, the research possibilities for the future are also presented as future works.

Last but not least, Appendix provides an overview of the widely-used control method for motor driving called Field-Oriented Control (FOC). Moreover, an example of utilizing the PHIL-based test-bench to verify the control design for a motor driver is

doi:10.6342/NTU202302551

presented. This demonstrates how the PHIL-based test-bench can greatly facilitate test for engineers, providing faster and more efficient way to perform the test compared to traditional methods.

doi:10.6342/NTU202302551

Chapter 2 Motor Models of SPMSM

2.1 Surface Permanent Magnet Synchronous Motor

2.1.1 Introduction to SPMSM

SPMSM is a synchronous motor configuration characterized by a rotor featuring permanent magnets mounted on its surface, which is integrated with a stator comprising windings. The rotor utilizes permanent magnets to create a magnetic field around the rotor, and the stator winding generates a rotating magnetic field, interacting with the permanent magnets in the rotor to produce torque.

SPMSM have various favorable characteristics, such as high power density, high efficiency, and versatility in different industries, including electric vehicles, industrial machinery, and household appliances. In order to operate in high-performance applications, accurate speed and torque control are necessary. Therefore, a mathematical model of SPMSM is required to implement a precise control design.

Refers to the contents in [16], the three-phase voltages across the stator windings can be expressed as:

$$\begin{bmatrix} v_a \\ v_b \\ v_c \end{bmatrix} = \begin{bmatrix} R_s & 0 & 0 \\ 0 & R_s & 0 \\ 0 & 0 & R_s \end{bmatrix} \begin{bmatrix} i_a \\ i_b \\ i_c \end{bmatrix} + \frac{d}{dt} \begin{bmatrix} \varphi_a \\ \varphi_b \\ \varphi_c \end{bmatrix} + \begin{bmatrix} v_n \\ v_n \\ v_n \end{bmatrix} \tag{2.1}$$

where v_a, v_b, v_c, i_a, i_b, i_c, R_s, φ_a, φ_b, φ_c, and v_n are the three-phase stator voltage, stator current, stator resistance, magnetic flux, and neutral voltage, respectively. Additionally, the magnetic flux in each phase can be further expressed as:

$$\begin{bmatrix} \varphi_a \\ \varphi_b \\ \varphi_c \end{bmatrix} = \begin{bmatrix} L_{aa} & L_{ab} & L_{ac} \\ L_{ba} & L_{bb} & L_{bc} \\ L_{ca} & L_{cb} & L_{cc} \end{bmatrix} \begin{bmatrix} i_a \\ i_b \\ i_c \end{bmatrix} + \begin{bmatrix} \varphi_{am} \\ \varphi_{bm} \\ \varphi_{cm} \end{bmatrix} \tag{2.2}$$

where L_{aa}, L_{bb}, and L_{cc} are the self-inductance, L_{ab}, L_{ac}, L_{ba}, L_{bc}, L_{ca}, and L_{cb} are the mutual inductance, and φ_{am}, φ_{bm}, and φ_{cm} are the magnetic fluxes produced by

doi:10.6342/NTU202302551

the rotor. Note that for SPMSM, all the self-inductance values and mutual inductance values are equal to L_s and M_s, respectively.

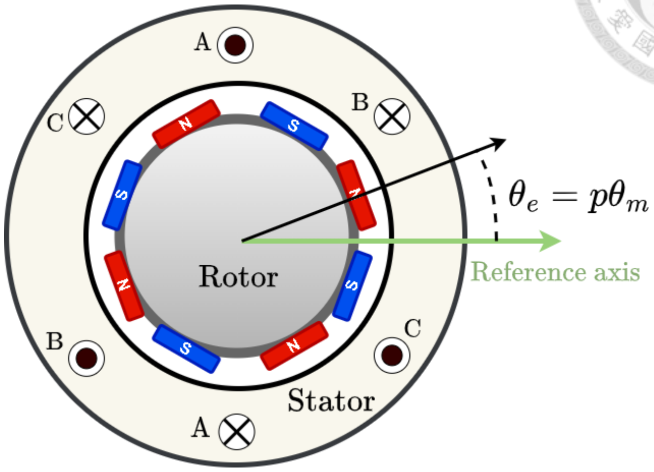

Fig. 2.1 The sectional view of a SPMSM showing mechanical angle (θ_m) and the electrical angle (θ_e).

The sectional view of a SPMSM is illustrated in Fig. 2.1. It can be seen that the SPMSM, as its name suggests, features permanent magnets mounted on the rotor surface. Moreover, the stator of the SPMSM contains three-phase coils that generate the necessary magnetic fields when supplied with three-phase currents. It is important to note that the mechanical angle (θ_m) is defined as zero degrees when the magnetic field produced by the permanent magnets aligns with the positive direction of the magnetic field, which is the reference axis in Fig. 2.1, generated by the A-phase current flowing through the A-phase coils in this thesis. Additionally, the relationship between electrical angle (θ_e) and mechanical angle is shown in Fig. 2.1, where p is the number of pole pairs for a SPMSM.

Based on this definition, the magnetic fluxes produced by the rotor can be expressed as (2.3) with the assumption that the rotor only creates a sinusoidal-shaped magnetic field.

$$\begin{bmatrix} \varphi_{am} \\ \varphi_{bm} \\ \varphi_{cm} \end{bmatrix} = \varphi_{pm} \begin{bmatrix} \cos\theta_e \\ \cos(\theta_e - 2\pi/3) \\ \cos(\theta_e + 2\pi/3) \end{bmatrix} = \varphi_{pm} \begin{bmatrix} \cos(p\theta_m) \\ \cos(p\theta_m - 2\pi/3) \\ \cos(p\theta_m + 2\pi/3) \end{bmatrix} \quad (2.3)$$

where φ_{pm}, θ_e, p, and θ_m are the flux linkage of permanent magnet, electrical angle,

doi:10.6342/NTU202302551

pole pairs, and mechanical angle, respectively.

Substituting the results of (2.2) and (2.3) into (2.1) yields the abc-axis mathematical model of SPMSM which is represented as:

$$\begin{bmatrix} v_a \\ v_b \\ v_c \end{bmatrix} = \begin{bmatrix} R_s & 0 & 0 \\ 0 & R_s & 0 \\ 0 & 0 & R_s \end{bmatrix} \begin{bmatrix} i_a \\ i_b \\ i_c \end{bmatrix} + \begin{bmatrix} L_s & -M_s & -M_s \\ -M_s & L_s & -M_s \\ -M_s & -M_s & L_s \end{bmatrix} \frac{d}{dt} \begin{bmatrix} i_a \\ i_b \\ i_c \end{bmatrix} + \begin{bmatrix} e_a \\ e_b \\ e_c \end{bmatrix} + \begin{bmatrix} v_n \\ v_n \\ v_n \end{bmatrix} \tag{2.4}$$

where the e_a, e_b, and e_c are the three-phase back-EMF, and can be express as:

$$\begin{bmatrix} e_a \\ e_b \\ e_c \end{bmatrix} = \frac{d}{dt} \begin{bmatrix} \varphi_{am} \\ \varphi_{bm} \\ \varphi_{cm} \end{bmatrix} = -\omega_e \varphi_{pm} \begin{bmatrix} \sin\theta_e \\ \sin(\theta_e - 2\pi/3) \\ \sin(\theta_e + 2\pi/3) \end{bmatrix} = -p\omega_m \varphi_{pm} \begin{bmatrix} \sin\theta_e \\ \sin(\theta_e - 2\pi/3) \\ \sin(\theta_e + 2\pi/3) \end{bmatrix}. \tag{2.5}$$

Note that ω_e is the electrical angular velocity, and ω_m is the mechanical angular velocity.

Based on (2.4), the three-phase SPMSM equivalent circuit can be illustrated in Fig. 2.2. By utilizing the equivalent circuit, the precise physical meanings can be obtained, which will be beneficial for subsequent derivations and analyses.

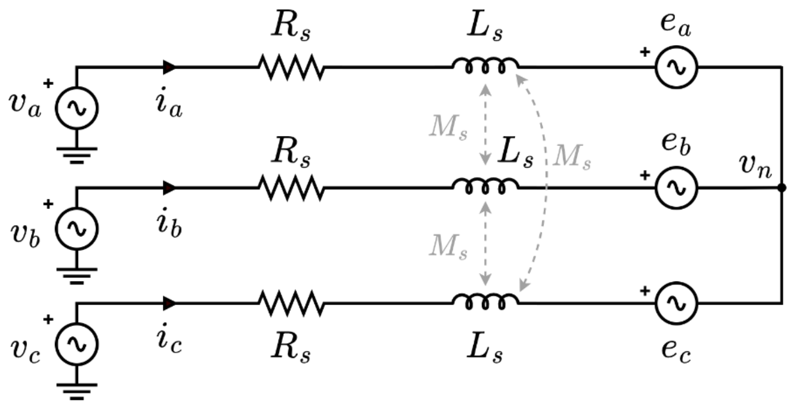

Fig. 2.2 The three-phase SPMSM equivalent circuit.

The electromagnetic torque (T_e) is produced when the magnetic field of the rotor interacts with the magnetic field on the stator, which is generated by the flow of three-phase AC current through the windings. Based on this, the electromagnetic torque can be expressed as:

doi:10.6342/NTU202302551

$$T_e = \frac{e_a i_a + e_b i_b + e_c i_c}{\omega_e}. \tag{2.6}$$

By Substituting (2.5) into (2.6), the expression for electromagnetic torque in terms of three-phase current can be obtained:

$$T_e = -\mathrm{p}\varphi_{pm}[i_a \sin\theta_e + i_b \sin(\theta_e - 2\pi/3) + i_c \sin(\theta_e + 2\pi/3)]. \tag{2.7}$$

Once the electromagnetic torque is derived, the mechanical angular velocity (ω_m) can be determined by the SPMSM mechanical dynamic equation:

$$T_e - T_L = J\frac{d\omega_m}{dt} + B\omega_m \tag{2.8}$$

where T_L is the load torque caused by the mechanical system connected to the motor, J is the inertia of the motor, and B is the friction coefficient.

2.1.2 Park Transfromation

In many research papers related to PMSM, the Park Transform, also known as Direct-Quadrature-Zero Transformation, is often employed to simplify the three-phase motor model and then using this results to implement the control design. This section provides a derivation of the dq-axis motor model.

First, assuming that the three-phase voltage (v_{abc}) and current (i_{abc}) have the same amplitude and frequency, but each phase is shifted by 120 degrees relative to each other. Afterward, the time-domain functions can be expressed in (2.9) and (2.10), respectively:

$$v_{abc} = \begin{bmatrix} v_a \\ v_b \\ v_c \end{bmatrix} = \sqrt{2}V_{rms}\begin{bmatrix} \cos(\omega t) \\ \cos(\omega t - 2\pi/3) \\ \cos(\omega t + 2\pi/3) \end{bmatrix} \tag{2.9}$$

$$i_{abc} = \begin{bmatrix} i_a \\ i_b \\ i_c \end{bmatrix} = \sqrt{2}I_{rms}\begin{bmatrix} \cos(\omega t) \\ \cos(\omega t - 2\pi/3) \\ \cos(\omega t + 2\pi/3) \end{bmatrix} \tag{2.10}$$

where ω is the angular velocity. For the motor driving application, ω is referred to the

doi:10.6342/NTU202302551

electrical rotational velocity (ω_e), and ωt, which is the angle for the three-phase voltage and current, is referred to the electrical angle (θ_e).

Based on this definition, the Park Transform matrix ($\boldsymbol{P}$) can be written as:

$$\boldsymbol{P} = \frac{2}{3}\begin{bmatrix} \cos(\theta_e) & \cos\left(\theta_e - \frac{2\pi}{3}\right) & \cos\left(\theta_e + \frac{2\pi}{3}\right) \\ -\sin(\theta_e) & -\sin\left(\theta_e - \frac{2\pi}{3}\right) & -\sin\left(\theta_e + \frac{2\pi}{3}\right) \\ \frac{1}{2} & \frac{1}{2} & \frac{1}{2} \end{bmatrix}. \tag{2.11}$$

By utilizing the Park Transform matrix ($\boldsymbol{P}$), the voltages and currents in dq0 coordinates, v_{dq0} and i_{dq0}, can be written as (2.12) and (2.13), respectively.

$$v_{dq0} = \begin{bmatrix} v_d \\ v_q \\ v_0 \end{bmatrix} = \boldsymbol{P} v_{abc} \tag{2.12}$$

$$i_{dq0} = \begin{bmatrix} i_d \\ i_q \\ i_0 \end{bmatrix} = \boldsymbol{P} i_{abc} \tag{2.13}$$

To transfer the voltages and currents in dq0 coordinates back to abc coordinates, the Inverse Park Transform matrix ($\boldsymbol{P}^{-1}$) is needed and presented as:

$$\boldsymbol{P}^{-1} = \begin{bmatrix} \cos(\theta_e) & -\sin(\theta_e) & 1 \\ \cos\left(\theta_e - \frac{2\pi}{3}\right) & -\sin\left(\theta_e - \frac{2\pi}{3}\right) & 1 \\ \cos\left(\theta_e + \frac{2\pi}{3}\right) & -\sin\left(\theta_e + \frac{2\pi}{3}\right) & 1 \end{bmatrix}. \tag{2.14}$$

By utilizing the Inverse Park Transform matrix ($\boldsymbol{P}^{-1}$), the abc-axis voltage (v_{abc}) and current (i_{abc}) can be written as (2.15) and (2.16), respectively.

$$v_{abc} = \begin{bmatrix} v_a \\ v_b \\ v_c \end{bmatrix} = \boldsymbol{P}^{-1} v_{dq0} \tag{2.15}$$

$$i_{abc} = \begin{bmatrix} i_a \\ i_b \\ i_c \end{bmatrix} = \boldsymbol{P}^{-1} i_{dq0} \tag{2.16}$$

doi:10.6342/NTU202302551

2.1.3 Derivation of dq-axis motor model

Since the motor used in this thesis is a three-phase motor with three wires, there is no neutral line present. As a result, the zero-axis components can be neglected, and the constraint equation can be written as:

$$i_a + i_b + i_c = \frac{di_a}{dt} + \frac{di_b}{dt} + \frac{di_c}{dt} = 0. \tag{2.17}$$

The dq-axis motor model can be derived by applying the Park Transform matrix ($\boldsymbol{P}$) to the abc-axis model shown in (2.4). The derivation procedures are shown below:

$$\boldsymbol{P}\begin{bmatrix} v_a \\ v_b \\ v_c \end{bmatrix} = \boldsymbol{P}\begin{bmatrix} R_s & 0 & 0 \\ 0 & R_s & 0 \\ 0 & 0 & R_s \end{bmatrix}\begin{bmatrix} i_a \\ i_b \\ i_c \end{bmatrix} + \boldsymbol{P}\frac{d}{dt}\left(\begin{bmatrix} L_s & -M_s & -M_s \\ -M_s & L_s & -M_s \\ -M_s & -M_s & L_s \end{bmatrix}\begin{bmatrix} i_a \\ i_b \\ i_c \end{bmatrix}\right) + \boldsymbol{P}\begin{bmatrix} e_a \\ e_b \\ e_c \end{bmatrix} + \boldsymbol{P}\begin{bmatrix} v_n \\ v_n \\ v_n \end{bmatrix}. \tag{2.18}$$

For the resistance part, the results can be expressed as:

$$\boldsymbol{P}\begin{bmatrix} R_s & 0 & 0 \\ 0 & R_s & 0 \\ 0 & 0 & R_s \end{bmatrix}\begin{bmatrix} i_a \\ i_b \\ i_c \end{bmatrix} = \left(\boldsymbol{P}\begin{bmatrix} R_s & 0 & 0 \\ 0 & R_s & 0 \\ 0 & 0 & R_s \end{bmatrix}\boldsymbol{P}^{-1}\right)\left(\boldsymbol{P}\begin{bmatrix} i_a \\ i_b \\ i_c \end{bmatrix}\right) = R_s\begin{bmatrix} i_d \\ i_q \end{bmatrix}. \tag{2.19}$$

Utilizing the product rule, the inductance part can be written as:

$$\boldsymbol{P}\frac{d}{dt}\left(\begin{bmatrix} L_s & -M_s & -M_s \\ -M_s & L_s & -M_s \\ -M_s & -M_s & L_s \end{bmatrix}\begin{bmatrix} i_a \\ i_b \\ i_c \end{bmatrix}\right) = \frac{d}{dt}\left(\boldsymbol{P}\begin{bmatrix} L_s & -M_s & -M_s \\ -M_s & L_s & -M_s \\ -M_s & -M_s & L_s \end{bmatrix}\begin{bmatrix} i_a \\ i_b \\ i_c \end{bmatrix}\right) - \frac{d\boldsymbol{P}}{dt}\begin{bmatrix} L_s & -M_s & -M_s \\ -M_s & L_s & -M_s \\ -M_s & -M_s & L_s \end{bmatrix}\begin{bmatrix} i_a \\ i_b \\ i_c \end{bmatrix}. \tag{2.20}$$

After that, the results of (2.20) can be further derived as:

$$\frac{d}{dt}\left(\boldsymbol{P}\begin{bmatrix} L_s & -M_s & -M_s \\ -M_s & L_s & -M_s \\ -M_s & -M_s & L_s \end{bmatrix}\begin{bmatrix} i_a \\ i_b \\ i_c \end{bmatrix}\right) = (L_s + M_s)\begin{bmatrix} \frac{di_d}{dt} \\ \frac{di_d}{dt} \end{bmatrix} \tag{2.21}$$

$$\frac{d\boldsymbol{P}}{dt}\begin{bmatrix} L_s & -M_s & -M_s \\ -M_s & L_s & -M_s \\ -M_s & -M_s & L_s \end{bmatrix}\begin{bmatrix} i_a \\ i_b \\ i_c \end{bmatrix} = p\omega_m(L_s + M_s)\begin{bmatrix} -i_q \\ i_d \end{bmatrix}. \tag{2.22}$$

doi:10.6342/NTU202302551

For the back-EMF and neutral voltage parts, the results can be expressed as:

$$\boldsymbol{P}\begin{bmatrix} e_a \\ e_b \\ e_c \end{bmatrix} = \begin{bmatrix} 0 \\ p\omega_m\varphi_{pm} \end{bmatrix} \tag{2.23}$$

$$\boldsymbol{P}\begin{bmatrix} v_n \\ v_n \\ v_n \end{bmatrix} = \begin{bmatrix} 0 \\ 0 \end{bmatrix}. \tag{2.24}$$

By combining the results from (2.18) to (2.24), the dq-axis motor model is yielded as shown in (2.25) and the equivalent circuit of dq-axis motor model is illustrated in Fig. 2.3.

$$\begin{bmatrix} v_d \\ v_q \end{bmatrix} = R_s\begin{bmatrix} i_d \\ i_q \end{bmatrix} + (L_s + M_s)\frac{d}{dt}\begin{bmatrix} i_d \\ i_q \end{bmatrix} + p\omega_m(L_s + M_s)\begin{bmatrix} -i_q \\ i_d \end{bmatrix} + \begin{bmatrix} 0 \\ p\omega_m\varphi_{pm} \end{bmatrix} \tag{2.25}$$

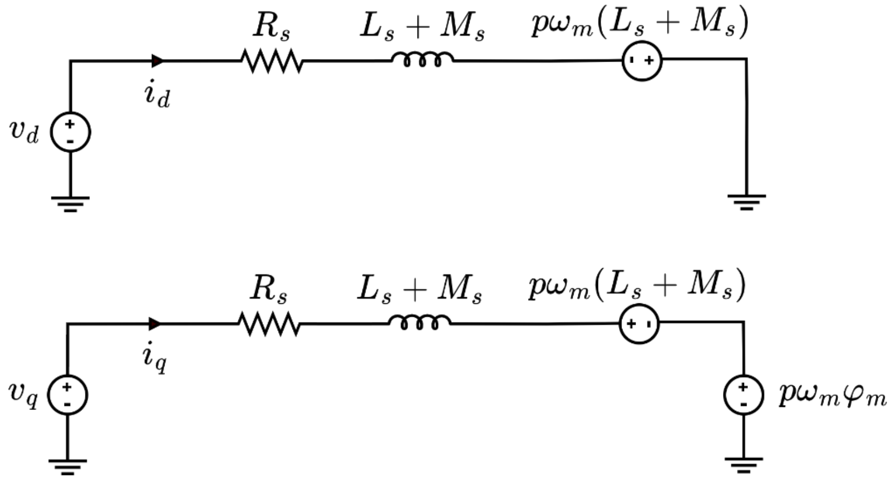

Fig. 2.3 The equivalent circuit of dq-axis motor model.

The primary advantage of dq-axis motor model is the simplicity. However, from the derivation above, it can be found that this advantage relies on the assumption of a balanced motor model. In the case of a fault scenario, the dq-axis model becomes more complex and lacks physical meaning compared to the abc-axis motor model.

Due to this reason, the derivations of different fault scenarios in this thesis are all conducted in abc coordinates.

doi:10.6342/NTU202302551

2.2 R-Unbalance Motor Model

2.2.1 Introduction to R-Unbalance Scenario

Resistance Unbalance (R-Unbalance) scenario is a common fault that can occur in PMSM, where the three-phase resistance are different from each other. In motor applications, the three-phase resistance can be divided into two part: the stator and the cables.

For the stator, the most common reasons causing the unbalance are the inevitable manufacturing defects for all the motor manufactories and the unequal winding temperatures which may occur due to harsh working environment [17], [18].

On the other hand, for the cables, if the motor operates in special conditions such as a deep drilling platform, the three-phase cables connected to the motor may have different lengths, leading to unbalanced resistances [19].

The unbalanced resistances result in torque disturbance and unbalanced currents, which are commonly known as negative sequence current in the field of Power Systems [20]-[23]. It worth noting that the negative sequence current exists in the other two fault senarios due to the same reason. Moreover, the consequences of this fault can be severe, causing significant performance degradation and possible damage to the motor if left unaddressed.

2.2.2 Derivation of R-Unbalance Motor Model

For the R-Unbalance motor model, it is assumed that all the motor parameters, such as self-inductance and flux linkage of the permanent magnet, are the same as the ones under balanced scenario except the three-phase resistance.

The three-phase SPMSM equivalent circuit under R-Unbalance scenario is

doi:10.6342/NTU202302551

illustrated in Fig. 2.4. By utilizing the equivalent circuit, the mathematical equations can be written as (2.26).

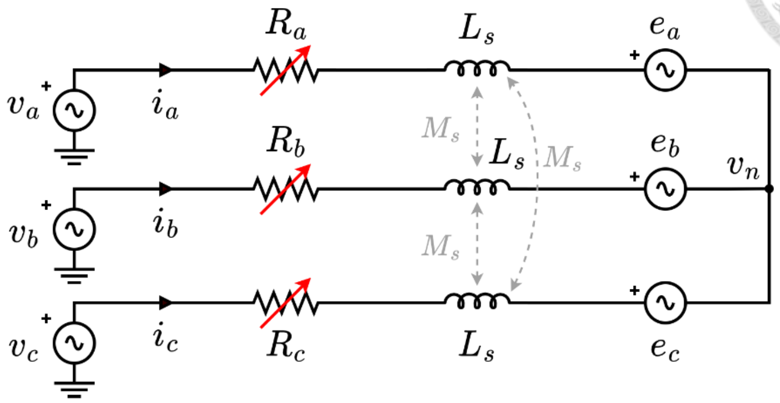

Fig. 2.4 The three-phase SPMSM equivalent circuit under R-Unbalance.

$$\begin{bmatrix} v_a \\ v_b \\ v_c \end{bmatrix} = \begin{bmatrix} R_a & 0 & 0 \\ 0 & R_b & 0 \\ 0 & 0 & R_c \end{bmatrix} \begin{bmatrix} i_a \\ i_b \\ i_c \end{bmatrix} + \begin{bmatrix} L_s & -M_s & -M_s \\ -M_s & L_s & -M_s \\ -M_s & -M_s & L_s \end{bmatrix} \frac{d}{dt} \begin{bmatrix} i_a \\ i_b \\ i_c \end{bmatrix} + \begin{bmatrix} e_a \\ e_b \\ e_c \end{bmatrix} + \begin{bmatrix} v_n \\ v_n \\ v_n \end{bmatrix} \qquad (2.26)$$

where the three-phase back-EMF, e_a, e_b, e_c, are the same with the results shown in (2.5) and $R_a, R_b,\ R_c$ are the three-phase resistance.

Utilizing the constraint equation shown in (2.27), the neutral voltage (v_n) can be derived as:

$$i_a + i_b + i_c = \frac{di_a}{dt} + \frac{di_b}{dt} + \frac{di_c}{dt} = 0 \qquad (2.27)$$

$$v_n = \frac{1}{3}(v_a + v_b + v_c) + \frac{1}{3}(R_a - R_b)i_b + \frac{1}{3}(R_a - R_c)i_c. \qquad (2.28)$$

Since numerical methods are employed to compute the reference current for PHIL in the MCU, a state-space form motor model is required for the implementation of numerical methods. Moreover, a further simplified model is preferred, which can conserve the computational resources of the MCU.

Due to this reason, the simplified motor model for R-Unbalance scenario is derived in state-space form by combining (2.26), (2.27), and (2.28). The results can be expressed as:

doi:10.6342/NTU202302551

$$\begin{cases} \dfrac{d}{dt}\begin{bmatrix} i_b \\ i_c \end{bmatrix} = \boldsymbol{A}\begin{bmatrix} i_b \\ i_c \end{bmatrix} + \boldsymbol{B}\begin{bmatrix} v_a \\ v_b \\ v_c \end{bmatrix} + \boldsymbol{C} \\ \dfrac{di_a}{dt} = -\left(\dfrac{di_b}{dt} + \dfrac{di_c}{dt}\right) \end{cases} \tag{2.29}$$

where the $\boldsymbol{A}$, $\boldsymbol{B}$, and $\boldsymbol{C}$ matrices are shown in (2.30), (2.31), and (2.32), respectively:

$$\boldsymbol{A} = \begin{bmatrix} \dfrac{-2R_b - R_a}{3(L_s + M_s)} & \dfrac{R_c - R_a}{3(L_s + M_s)} \\ \dfrac{R_b - R_a}{3(L_s + M_s)} & \dfrac{-2R_c - R_a}{3(L_s + M_s)} \end{bmatrix} \tag{2.30}$$

$$\boldsymbol{B} = \begin{bmatrix} -\dfrac{1}{3(L_s + M_s)} & \dfrac{2}{3(L_s + M_s)} & -\dfrac{1}{3(L_s + M_s)} \\ -\dfrac{1}{3(L_s + M_s)} & -\dfrac{1}{3(L_s + M_s)} & \dfrac{2}{3(L_s + M_s)} \end{bmatrix} \tag{2.31}$$

$$\boldsymbol{C} = \frac{p\omega_m\varphi_{pm}}{L_s + M_s}\begin{bmatrix} sin(\theta_e - 2/3\,\pi) \\ sin(\theta_e + 2/3\,\pi) \end{bmatrix}. \tag{2.32}$$

2.3 OPF Motor Model

2.3.1 Introduction to OPF Scenario

Open-Phase Fault (OPF) is a severe type of fault that can cause significant performance degradation in PMSM, and this fault occurs when one of the three phases of the motor becomes disconnected, either due to a failure in the motor windings or in the power supply cables.

When OPF occurs, the current in the open phase becomes zero, while the currents in the other two phases increase to maintain the output torque. As a result, the motor operates in a highly unbalanced state, leading to several issues such as overloading and overheating of the motor [24], [25].

In fact, OPF can be considered as one of the worst-case condition of R-Unbalance scenario. Therefore, the impacts of OPF can lead to greater mechanical stress on the

doi:10.6342/NTU202302551

motor, and can cause the rotor to deviate from its optimal position, leading to a further decrease in motor efficiency.

2.3.2 Derivation of OPF Motor Model

For the OPF motor model used in this thesis, assuming that phase A is disconnected and all the motor parameters are the same as the ones under balanced scenario.

The three-phase SPMSM equivalent circuit under OPF is illustrated in Fig. 2.5. By utilizing the equivalent circuit, the mathematical equations can be written as (2.33):

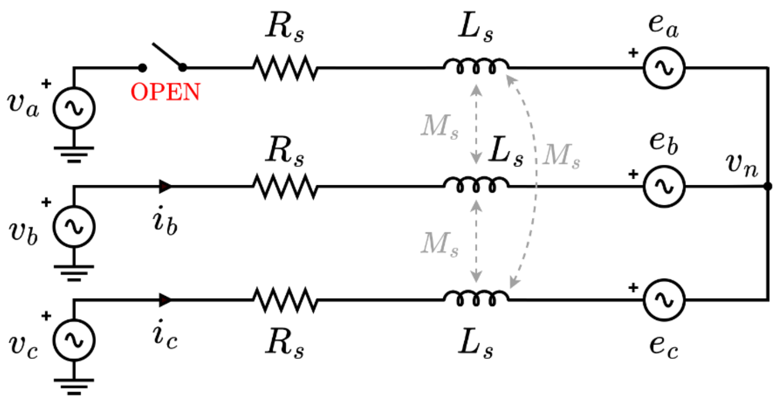

Fig. 2.5 The three-phase SPMSM equivalent circuit under OPF.

$$\begin{bmatrix} v_b \\ v_c \end{bmatrix} = \begin{bmatrix} R_s & 0 \\ 0 & R_s \end{bmatrix} \begin{bmatrix} i_b \\ i_c \end{bmatrix} + \begin{bmatrix} L_s & -M_s \\ -M_s & L_s \end{bmatrix} \frac{d}{dt} \begin{bmatrix} i_b \\ i_c \end{bmatrix} + \begin{bmatrix} e_b \\ e_c \end{bmatrix} + \begin{bmatrix} v_n \\ v_n \end{bmatrix} \tag{2.33}$$

where the B-phase and C-phase back-EMF, e_b, e_c, are the same with the results shown in (2.5).

Utilizing the constraint equations for OPF shown in (2.34), the neutral voltage (v_n) can be derived as (2.35).

$$\begin{cases} i_a = 0 \\ i_b + i_c = \dfrac{di_b}{dt} + \dfrac{di_c}{dt} = 0 \end{cases} \tag{2.34}$$

$$v_n = \frac{1}{2}(v_b + v_c) \tag{2.35}$$

Due to the same reason as the one explained in Section 2.2.2 , the simplified motor

doi:10.6342/NTU202302551

model for OPF is derived in state-space form by combining (2.33), (2.34), and (2.35). The results can be expressed as:

$$\begin{cases} \dfrac{d}{dt}\begin{bmatrix} i_a \\ i_b \end{bmatrix} = \boldsymbol{A}\begin{bmatrix} i_a \\ i_b \end{bmatrix} + \boldsymbol{B}\begin{bmatrix} v_a \\ v_b \\ v_c \end{bmatrix} + \boldsymbol{C} \\ \dfrac{di_c}{dt} = -\dfrac{di_b}{dt} \end{cases} \tag{2.36}$$

where the ***A***, ***B***, and ***C*** matrices are shown in (2.37), (2.38), and (2.39), respectively:

$$\boldsymbol{A} = \begin{bmatrix} 0 & 0 \\ 0 & \dfrac{-R_s}{(L_s - M_s)} \end{bmatrix} \tag{2.37}$$

$$\boldsymbol{B} = \begin{bmatrix} 0 & 0 & 0 \\ 0 & \dfrac{1}{2(L_s - M_s)} & -\dfrac{1}{2(L_s - M_s)} \end{bmatrix} \tag{2.38}$$

$$\boldsymbol{C} = \frac{p\omega_m \varphi_{pm}}{L_s - M_s}\begin{bmatrix} 0 \\ sin(\theta_e - 2/3\,\pi) \end{bmatrix}. \tag{2.39}$$

2.4 ISCF Motor Model

2.4.1 Introduction to ISCF Scenario

Inter-Turn Short-Circuit Fault (ISCF) is the most common and the worst fault that can occur in PMSM, accounting for approximately 30-40% of all failures. This fault occurs when part of the turns in a specific winding slot become shorted, and the causes of this fault can be attributed to voltage stress, thermal stress, mechanical vibration, and insulation failure [26].

When ISCF occurs, an extremely high fault current flows through the shorted turns, resulting in circulating currents in a particular phase that can be more than 10 times higher than the rated current. This excessive current flow can cause a significant increase in temperature, which may demagnetize the permanent magnets irreversibly and further degrade the surrounding insulation material. Consequently, the winding may lose its insulation property, which can cause more severe damage to the motor.

doi:10.6342/NTU202302551

Currently, different modeling methodologies for ISCF have been presented and verified in previous studies [26]-[32]. However, the existing methods typically assume a sinusoidal-shaped phase voltage input, which cannot capture the presence of switching harmonics in the fault current [33]. Although switching harmonics may not be crucial for fault diagnosis in motor driving, they cannot be neglected for PHIL applications, where the goal is to emulate the motor as accurately as possible. Therefore, the motor model for ISCF derived in this thesis takes the effect of switching into account, and the results are presented in Chapter 4 and Chapter 5 .

2.4.2 Derivation of ISCF Motor Model

For the ISCF motor model in this thesis, it is assumed that the fault is occurred in phase A. That is to say, there is a shorted path between the turns in phase A. In this thesis, a resistor is chosen as the impedance model for the shorted path due to its simplicity Finally, the three-phase SPMSM equivalent circuit under ISCF can be illustrated as Fig. 2.6. By utilizing the equivalent circuit shown in Fig. 2.6, the mathematical equations can be written as (2.40):

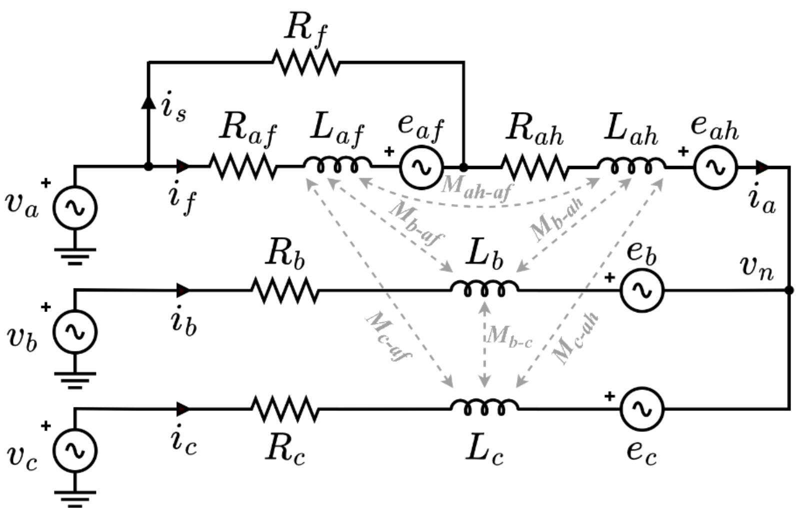

Fig. 2.6 The three-phase SPMSM equivalent circuit under ISCF.

doi:10.6342/NTU202302551

$$\begin{bmatrix} v_a \\ v_b \\ v_c \\ 0 \end{bmatrix} = \boldsymbol{R}\begin{bmatrix} i_a \\ i_b \\ i_c \\ i_s \end{bmatrix} + \boldsymbol{L}\frac{d}{dt}\begin{bmatrix} i_a \\ i_b \\ i_c \\ i_s \end{bmatrix} + \boldsymbol{e} + \begin{bmatrix} v_n \\ v_n \\ v_n \\ 0 \end{bmatrix} \tag{2.40}$$

where the i_s is the current flow in the short path and the $\boldsymbol{R}$, $\boldsymbol{L}$, and $\boldsymbol{e}$ matrices are shown in (2.41), (2.42), and (2.43), respectively:

$$\boldsymbol{R} = \begin{bmatrix} R_{ah} + R_{af} & 0 & 0 & -R_{af} \\ 0 & R_b & 0 & 0 \\ 0 & 0 & R_c & 0 \\ R_{af} & 0 & 0 & -R_f - R_{af} \end{bmatrix} \tag{2.41}$$

$$\boldsymbol{L} = \begin{bmatrix} L_{ah} + L_{af} + 2M_{ah-af} & M_{b-ah} + M_{b-af} & M_{c-ah} + M_{c-af} & -L_{af} - M_{ah-af} \\ M_{b-ah} + M_{b-af} & L_b & M_{b-c} & -M_{b-af} \\ M_{c-ah} + M_{c-af} & M_{b-c} & L_c & -M_{c-af} \\ L_{af} + M_{ah-af} & M_{b-af} & M_{c-af} & -L_{af} \end{bmatrix} \tag{2.42}$$

$$\boldsymbol{e} = \begin{bmatrix} e_{ah} + e_{af} \\ e_b \\ e_c \\ e_{af} \end{bmatrix}. \tag{2.43}$$

In the resistance matrix $\boldsymbol{R}$, R_{ah}, R_{af}, R_f, R_b, and R_c, are the A-phase resistance of remaining healthy coils, A-phase resistance of shorted turns, fault resistance in the short path, B-phase resistance, and C-phase resistance, respectively.

In the inductance matrix $\boldsymbol{L}$, L_{ah}, L_{af}, L_b, L_c, M_{ah-af}, M_{b-ah}, M_{b-af}, M_{c-ah}, M_{c-af}, and M_{b-c} are the A-phase self-inductance of remaining healthy coils, A-phase self-inductance of shorted turns, B-phase self-inductance, C-phase self-inductance, mutual inductance between healthy coils and shorted turns in phase A, mutual inductance between B-phase coils and healthy coils in phase A, mutual inductance between B-phase coils and shorted turns in phase A, mutual inductance between C-phase coils and healthy coils in phase A, mutual inductance between C-phase coils and shorted turns in phase A, and mutual inductance between B-phase coils and C-phase coils, respectively.

In the back-EMF matrix $\boldsymbol{e}$, e_{ah}, e_{af}, e_b, and e_c are the A-phase back-EMF of

doi:10.6342/NTU202302551

remaining healthy coils, A-phase back-EMF of shorted turns, B-phase back-EMF, and C-phase back-EMF, respectively.

Assuming that N_{fault} turns have been shorted out of N_{total} in phase A for the emulated SPMSM, and the fault index (Δ) is defined as:

$$\Delta = \frac{N_{fault}}{N_{total}}. \tag{2.44}$$

Utilizing the fault index (Δ) with the basic concepts from Circuit Theory, the parameters in $\boldsymbol{R}$, $\boldsymbol{L}$, and $\boldsymbol{e}$ matrices can be expressed as (2.45), (2.46), and (2.47), respectively:

$$\begin{bmatrix} R_{ah} \\ R_{af} \\ R_b \\ R_c \end{bmatrix} = \begin{bmatrix} (1-\Delta)R_s \\ \Delta R_s \\ R_s \\ R_s \end{bmatrix} \tag{2.45}$$

$$\begin{bmatrix} L_{ah} \\ L_{af} \\ L_b \\ L_c \\ M_{ah-af} \\ M_{b-ah} \\ M_{b-af} \\ M_{c-ah} \\ M_{c-af} \\ M_{b-c} \end{bmatrix} = \begin{bmatrix} (1-\Delta)^2\, L_s \\ \Delta^2 L_s \\ L_s \\ L_s \\ (1-\Delta)\Delta L_s \\ -(1-\Delta)M_s \\ -\Delta M_s \\ -(1-\Delta)M_s \\ -\Delta M_s \\ -M_s \end{bmatrix} \tag{2.46}$$

$$\begin{bmatrix} e_{ah} \\ e_{af} \\ e_b \\ e_c \end{bmatrix} = \begin{bmatrix} -(1-\Delta)p\omega_m\varphi_{pm}sin\theta_e \\ -\Delta p\omega_m\varphi_{pm}sin\theta_e \\ -p\omega_m\varphi_{pm}sin(\theta_e - 2\pi/3) \\ -p\omega_m\varphi_{pm}sin(\theta_e + 2\pi/3) \end{bmatrix}. \tag{2.47}$$

By substituting all the parameters shown above, the dynamic equations of ISCF can be written as:

doi:10.6342/NTU202302551

$$\begin{bmatrix} v_a \\ v_b \\ v_c \\ 0 \end{bmatrix} = \begin{bmatrix} R_s & 0 & 0 & -\Delta R_s \\ 0 & R_s & 0 & 0 \\ 0 & 0 & R_s & 0 \\ \Delta R_s & 0 & 0 & -R_f - \Delta R_s \end{bmatrix} \begin{bmatrix} i_a \\ i_b \\ i_c \\ i_s \end{bmatrix}$$
$$+ \begin{bmatrix} L_s & -M_s & -M_s & -\Delta L_s \\ -M_s & L_s & -M_s & \Delta M_s \\ -M_s & -M_s & L_s & \Delta M_s \\ \Delta L_s & -\Delta M_s & -\Delta M_s & -\Delta^2 L_s \end{bmatrix} \frac{d}{dt} \begin{bmatrix} i_a \\ i_b \\ i_c \\ i_s \end{bmatrix}$$
$$-p\omega_m \varphi_{pm} \begin{bmatrix} sin\theta_e \\ \sin(\theta_e - 2\pi/3) \\ \sin(\theta_e + 2\pi/3) \\ \Delta sin\theta_e \end{bmatrix} + \begin{bmatrix} v_{\mathrm{n}} \\ v_{\mathrm{n}} \\ v_{\mathrm{n}} \\ 0 \end{bmatrix}. \tag{2.48}$$

Utilizing the constraint equation shown in (2.49), the neutral voltage (v_n) can be derived as (2.50):

$$i_a + i_b + i_c = \frac{di_a}{dt} + \frac{di_b}{dt} + \frac{di_c}{dt} = 0 \tag{2.49}$$

$$v_n = \frac{1}{3}(v_a + v_b + v_c) + \frac{\Delta R_s}{3} i_s + \frac{\Delta}{3}(L_s - 2M_s)\frac{di_s}{dt}. \tag{2.50}$$

After applying further simplification of the equations with the aid of (2.49), (2.50), the simplified state-space form motor model for ISCF is derived as:

$$\begin{cases} \frac{d}{dt}\begin{bmatrix} i_b \\ i_c \\ i_s \end{bmatrix} = \boldsymbol{A}\begin{bmatrix} i_b \\ i_c \\ i_s \end{bmatrix} + \boldsymbol{B}\begin{bmatrix} v_a \\ v_b \\ v_c \end{bmatrix} + \boldsymbol{C} \\ \frac{di_a}{dt} = -\left(\frac{di_b}{dt} + \frac{di_c}{dt}\right) \end{cases} \tag{2.51}$$

where the $\boldsymbol{A}$, $\boldsymbol{B}$, and $\boldsymbol{C}$ matrices are shown in (2.52), (2.53), and (2.54), respectively:

$$\boldsymbol{A} = \begin{bmatrix} \frac{-R_s}{L_s + M_s} & 0 & \frac{R_f(L_s + M_s) + \Delta R_s[(L_s + M_s) - \Delta L_s]}{\Delta(L_s - 2M_s)(L_s + M_s)} \\ 0 & \frac{-R_s}{L_s + M_s} & \frac{R_f(L_s + M_s) + \Delta R_s[(L_s + M_s) - \Delta L_s]}{\Delta(L_s - 2M_s)(L_s + M_s)} \\ 0 & 0 & \frac{\Delta R_s(2\Delta - 3) - 3R_f}{\Delta^2(L_s - 2M_s)} \end{bmatrix} \tag{2.52}$$

doi:10.6342/NTU202302551

$$\boldsymbol{B} = \begin{bmatrix} \frac{-L_s}{(L_s-2M_s)(L_s+M_s)} & \frac{(L_s-M_s)}{(L_s-2M_s)(L_s+M_s)} & \frac{M_s}{(L_s-2M_s)(L_s+M_s)} \\ \frac{-L_s}{(L_s-2M_s)(L_s+M_s)} & \frac{M_s}{(L_s-2M_s)(L_s+M_s)} & \frac{(L_s-M_s)}{(L_s-2M_s)(L_s+M_s)} \\ \frac{2}{\Delta(L_s-2M_s)} & \frac{-1}{\Delta(L_s-2M_s)} & \frac{-1}{\Delta(L_s-2M_s)} \end{bmatrix} \quad (2.53)$$

$$\boldsymbol{C} = \frac{p\omega_m\varphi_{pm}}{L_s+M_s}\begin{bmatrix} sin(\theta_e - 2/3\,\pi) \\ sin(\theta_e + 2/3\,\pi) \\ 0 \end{bmatrix}. \quad (2.54)$$

Another factor that differs from the other scenarios for the ISCF is electromagnetic torque (T_e). Since the A-phase winding is separated into two different windings by the shorted turns, there are two back-EMF sources, e_{af} and e_{ah}, shown in Fig. 2.6. Based on the theorem in Section 2.1.1 , the electromagnetic torque can be expressed as:

$$T_e = \frac{e_{ah}i_a + e_{af}i_f + e_b i_b + e_c i_c}{\omega_e}. \quad (2.55)$$

By Substituting the results from (2.47) into (2.55), and using the relationship between i_f, i_a, and i_s shown in (2.56), the expression for electromagnetic torque in terms of three-phase current can be expressed as (2.57).

$$i_f = i_a - i_s \quad (2.56)$$

$$T_e = -\mathrm{p}\varphi_{pm}[(i_a - \Delta i_s)\sin\theta_e + i_b\sin(\theta_e - 2\pi/3) + i_c\sin(\theta_e + 2\pi/3)] \quad (2.57)$$

2.5 Numerical Methods

Once the motor model has been derived for each fault scenario, the dynamic equations can be expressed in state-space form. These equations can then be utilized for motor model calculations in simulations and MCU by employing numerical methods. With the help of numerical methods, the motor model can be effectively implemented, providing accurate and efficient calculations in both simulation environments and real-time MCU applications. Consequently, the selection of an appropriate numerical method

doi:10.6342/NTU202302551

is a crucial consideration for PHIL implementation.

The class diagram of common numerical methods is illustrated in Fig. 2.7.

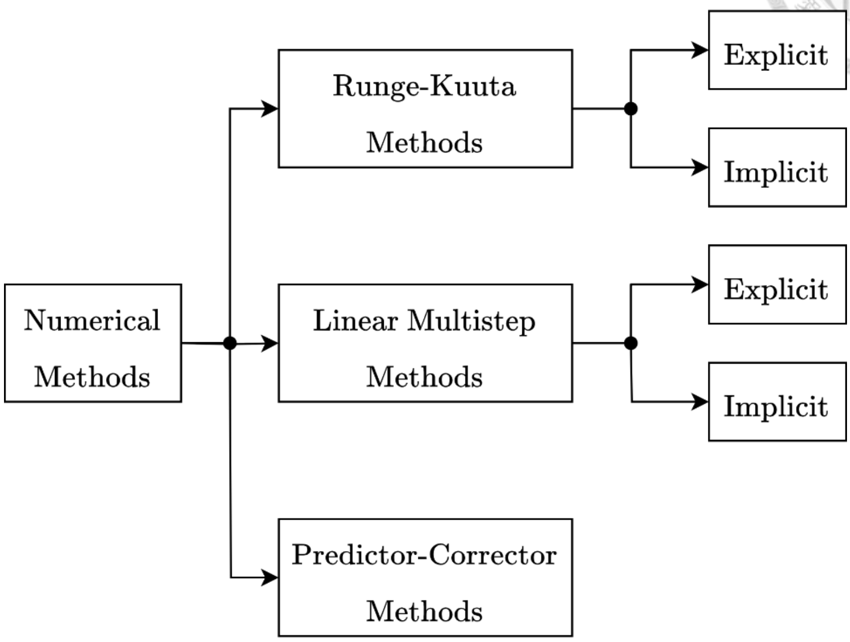

Fig. 2.7 The class diagram of common numerical methods.

The numerical methods can be broadly classified into three groups: Runge-Kutta methods, linear multistep methods, and predictor-corrector methods [34]. Furthermore, the first two methods can be further categorized based on whether they are explicit or implicit.

In this thesis, the theoretical discussion on the selection of numerical methods will not be covered. However, it is important to note that the choice of a numerical method involves a trade-off between stability and accuracy of nonlinear effects, considering the limited computational resources available. That is to say, employing a more complex numerical method ensures accurate modeling of nonlinear effects, but it comes at the expense of increased computational resources. As a result, the time step of the numerical method needs to be larger, which may impact the stability and overall accuracy of the model. On the other hand, by employing a simpler numerical method, the time step can

doi:10.6342/NTU202302551

be shortened as much as possible to enhance the stability and overall accuracy, despite the fact that the accuracy for nonlinear effects is reduced.

By trial and error, the modified Euler's method, which is often referred to second order Runge-Kutta method, is adopted in this thesis [35]. The discrete-time expression can be expressed as:

$$\begin{aligned}\widetilde{K}[n] &= K[n] + hf(K[n]) \\ K[n+1] &= K[n] + \frac{h}{2}\left[f(K[n]) + f\left(\widetilde{K}[n]\right)\right]\end{aligned} \tag{2.58}$$

where function f is the derivative of the model and it can be simply expressed as:

$$f(K) = \frac{dK}{dt}. \tag{2.59}$$

Note that h is the time step, $K[n]$ is the model result in current step, $\widetilde{K}[\mathrm{n}]$ is a predicted result of the model, and $K[n]$ is the model result in future step. Since the modified Euler's method use the predicted value to correct the result in future step, this method can also be regarded as a simple predictor-corrector method.

Last but not least, it is important to note that with the numerical method presented in this section, the model calculation can be implement, which means the reference currents for the PHIL current control are obtained. Therefore, the subsequent step involves designing the PHIL current control. Moreover, to achieve a better performance of the motor emulation, a new control method is proposed and the discussions are presented in the next chapter.

doi:10.6342/NTU202302551

Chapter 3 Control Methods of PHIL

With the motor models derived in Chapter 2, the subsequent task involves selecting an appropriate control method to design the current controller for PHIL. It is worth noting that design the controller in dq-axis has several advantages, thus the control method discussed in this thesis is implemented in dq-axis [36]. In Chapter 3, the control plant for PHIL in the dq-axis is derived initially. Subsequently, a design procedure for the traditional decoupling PI control is outlined. The chapter then proceeds to introduce the fundamental concepts of DSRF control and derivation of the proposed CPIR control. The final section focuses on the digitalization and implementation aspects of the controllers used in the proposed CPIR control.

3.1 PHIL Control Plant

3.1.1 Coupling Network

The Coupling network plays a crucial role in PHIL system as it directly affects the magnitude of Total Harmonics Distortion(THD) in the line current. Furthermore, the selection of the coupling network significantly influences the choice of the appropriate control methodology for PHIL implementation.

In [37]-[39], different coupling network topologies and the corresponding control methods for PHIL are discussed. Two popular topologies, RL filter and LCL filter, are compared in [40]. From these studies, a brief conclusion can be made that LCL filter is effective in reducing the THD of the line current, thereby enhancing the accuracy of the motor emulation. However, implementing a control design with LCL filter is more challenging due to complexity. Specifically, utilizing LCL filter introduced an additional state variable, which is the voltage of the capacitor (v_c). In some cases, to reduce the cost

doi:10.6342/NTU202302551

of the system, sensorless control methodology is employed using state observer. By doing so, the complexity and the stability are significantly affected.

Meanwhile, although using an RL filter leads to a higher THD and lower emulation accuracy compared to LCL filter, it is still the most commonly adopted coupling network in the field of PHIL research due to the simplicity of the control design and the stable characteristics of RL filter. Thus, an RL filter is adopted as the coupling network in this thesis.

3.1.2 Derivation of dq-axis Control Plant

To implement the control design in PHIL, the control plant should be derived first.

In this thesis, the PHIL control plant is comprised of two parts: the coupling network and the three-phase Common-Mode Choke (CMC). In order to facilitate energy recovery within the PHIL-based test-bench, the common-DC-bus configuration is implemented, which leads to the flow of common-mode currents in each phase [41]. Thus, the consideration of zero-axis is needed.

To suppress the low-frequency components in the common-mode current, a PI controller in zero-axis is adopted. On the other hand, a CMC is utilized to deal with the high-frequency components that exceed the bandwidth of the controller, and that is why in this thesis CMC is adopted.

Due to this reason, the abc-axis equivalent circuit of the PHIL test-bench is illustrated in Fig. 3.1. Note that the assumption is made that all the parameters are balanced and the mutual inductance in the coupling network can be ignored. By utilizing the equivalent circuit, the abc-axis mathematical equations can be written as (3.1):

doi:10.6342/NTU202302551

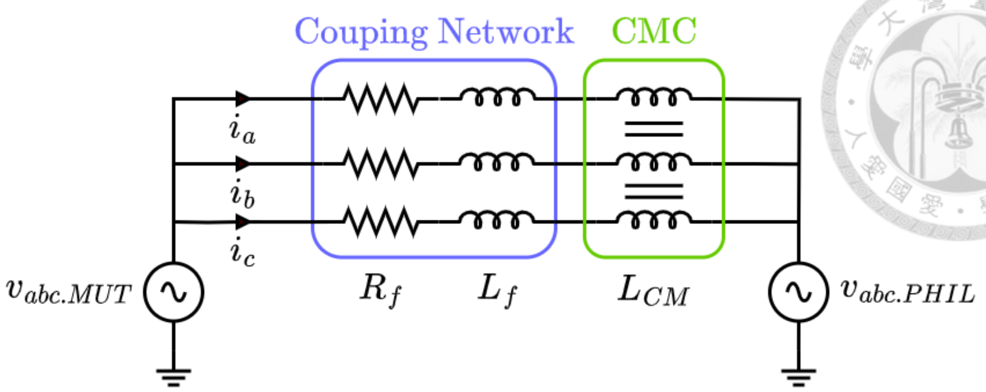

Fig. 3.1 The abc-axis equivalent circuit of the PHIL test-bench.

$$\begin{bmatrix} v_{a.MUT} \\ v_{b.MUT} \\ v_{c.MUT} \end{bmatrix} = \begin{bmatrix} R_f & 0 & 0 \\ 0 & R_f & 0 \\ 0 & 0 & R_f \end{bmatrix} \begin{bmatrix} i_a \\ i_b \\ i_c \end{bmatrix} + \begin{bmatrix} L_f + L_{CM} & L_{CM} & L_{CM} \\ L_M & L_f + L_{CM} & L_{CM} \\ L_M & L_M & L_f + L_{CM} \end{bmatrix} \frac{d}{dt} \begin{bmatrix} i_a \\ i_b \\ i_c \end{bmatrix} + \begin{bmatrix} v_{a.PHIL} \\ v_{b.PHIL} \\ v_{c.PHIL} \end{bmatrix} \quad (3.1)$$

where $v_{a.MUT}$, $v_{b.MUT}$, $v_{c.MUT}$, $v_{a.PHIL}$, $v_{b.PHIL}$, and $v_{c.PHIL}$ are the three-phase voltages produced by MUT and PHIL. R_f, L_f, and L_M are the filter resistance, inductance, and CMC inductance, respectively.

By utilizing the Park transform matrix (***P***) presented in (2.11), the abc-axis equations can be transformed to dq0 coordinates. The results are shown in (3.2):

$$\begin{bmatrix} v_{d.MUT} \\ v_{q.MUT} \\ v_{0.MUT} \end{bmatrix} = \begin{bmatrix} R_f & 0 & 0 \\ 0 & R_f & 0 \\ 0 & 0 & R_f \end{bmatrix} \begin{bmatrix} i_d \\ i_q \\ i_0 \end{bmatrix} + \begin{bmatrix} L_f & 0 & 0 \\ 0 & L_f & 0 \\ 0 & 0 & L_f + 3L_{CM} \end{bmatrix} \frac{d}{dt} \begin{bmatrix} i_d \\ i_q \\ i_0 \end{bmatrix} + p\omega_m L_f \begin{bmatrix} -i_q \\ i_d \\ i_0 \end{bmatrix} + \begin{bmatrix} v_{d.PHIL} \\ v_{q.PHIL} \\ v_{0.PHIL} \end{bmatrix}, \quad (3.2)$$

where $v_{d.MUT}$, $v_{q.MUT}$, $v_{0.MUT}$, $v_{d.PHIL}$, $v_{q.PHIL}$, and $v_{0.PHIL}$ are the dq0-axis voltages produced by MUT and PHIL.

With the Laplace transform, the transfer functions of the PHIL can be derived as (3.3):

doi:10.6342/NTU202302551

$$
\begin{cases}
i_d = -\dfrac{1}{sL_f + R_f} v_{d.PHIL} + \dfrac{p\omega_m L_f}{sL_f + R_f} i_q + \dfrac{1}{sL_f + R_f} v_{d.PHIL} \\
i_q = -\dfrac{1}{sL_f + R_f} v_{q.PHIL} - \dfrac{p\omega_m L_f}{sL_f + R_f} i_d + \dfrac{1}{sL_f + R_f} v_{q.PHIL} \\
i_0 = -\dfrac{1}{s(L_f + 3L_{CM}) + R_f} v_{0.PHIL} + \dfrac{1}{sL_f + R_f} v_{0.PHIL}
\end{cases}. \tag{3.3}
$$

Finally, the PHIL control plant block diagram is illustrated in Fig. 3.2. By utilizing the block diagram and the transfer functions shown in (3.3), the PHIL current control can be designed with various control methodologies.

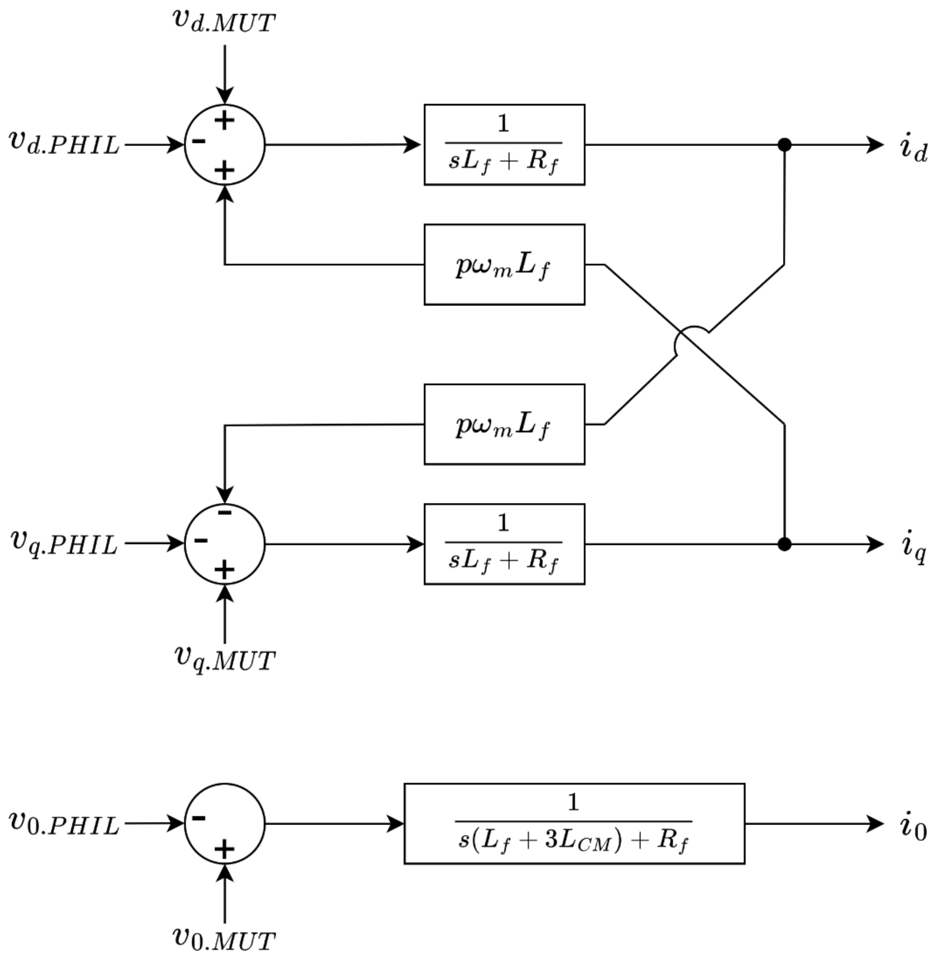

Fig. 3.2 The block diagram of PHIL control plant.

doi:10.6342/NTU202302551

3.2 Traditional PI Control

3.2.1 Introduction to Decoupling PI Control

For the motor driver current controller, the most used method is called decoupling PI control [43], [43]. The main concept of this method, which is often referred as "decoupling", is to use the feedback signals and the parameters of the control plant to linearize the system. By doing this, the control plant will be linear and the classical control theory can be applied.

By utilizing this method in the PHIL current control, the closed-loop current control block diagram in PHIL can be shown as Fig. 3.3:

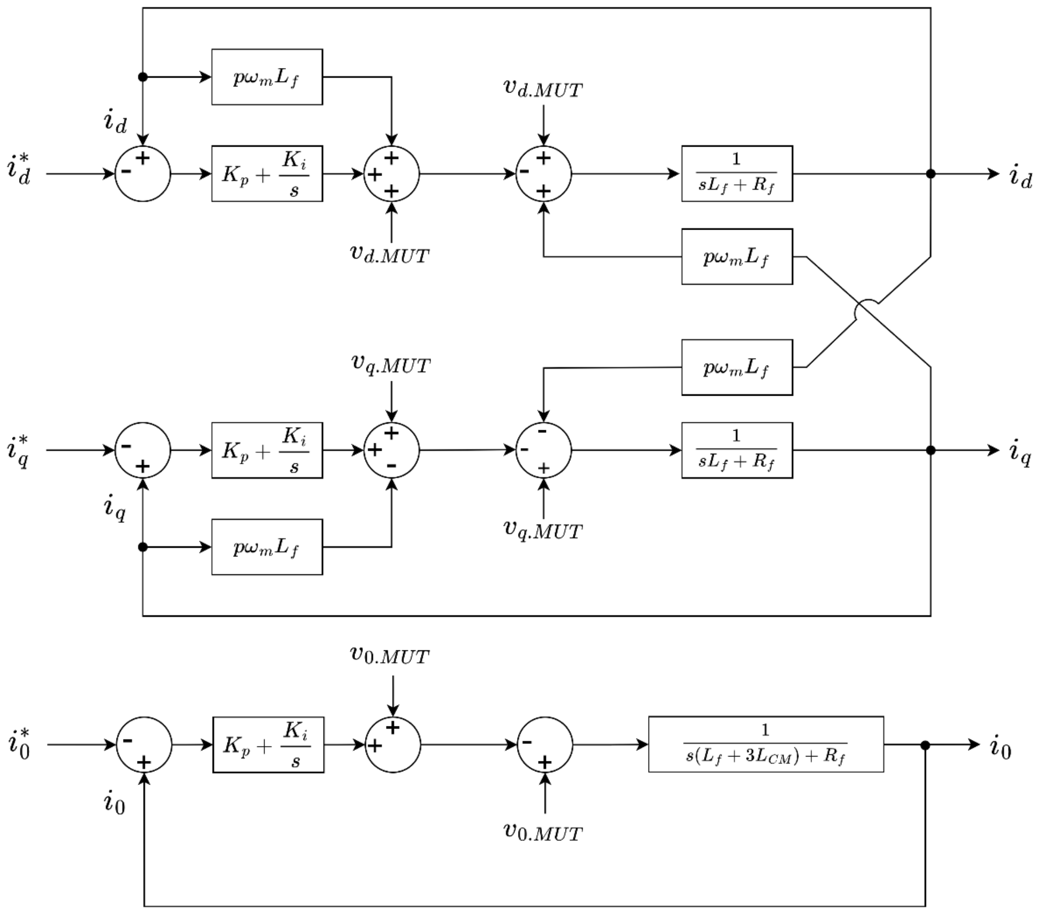

Fig. 3.3 The closed-loop current control block diagram.

where i_d^*, i_q^*, and i_0^* are the current reference of dq0-axis, respectively.K_p and K_i are the proportional gain and integral gain for the PI control.

doi:10.6342/NTU202302551

Assuming that the coupling network and three-phase common mode choke are ideal, and the measured parameters and sensors are all error-free. The closed-loop diagram can be simplified as shown in Fig. 3.4.

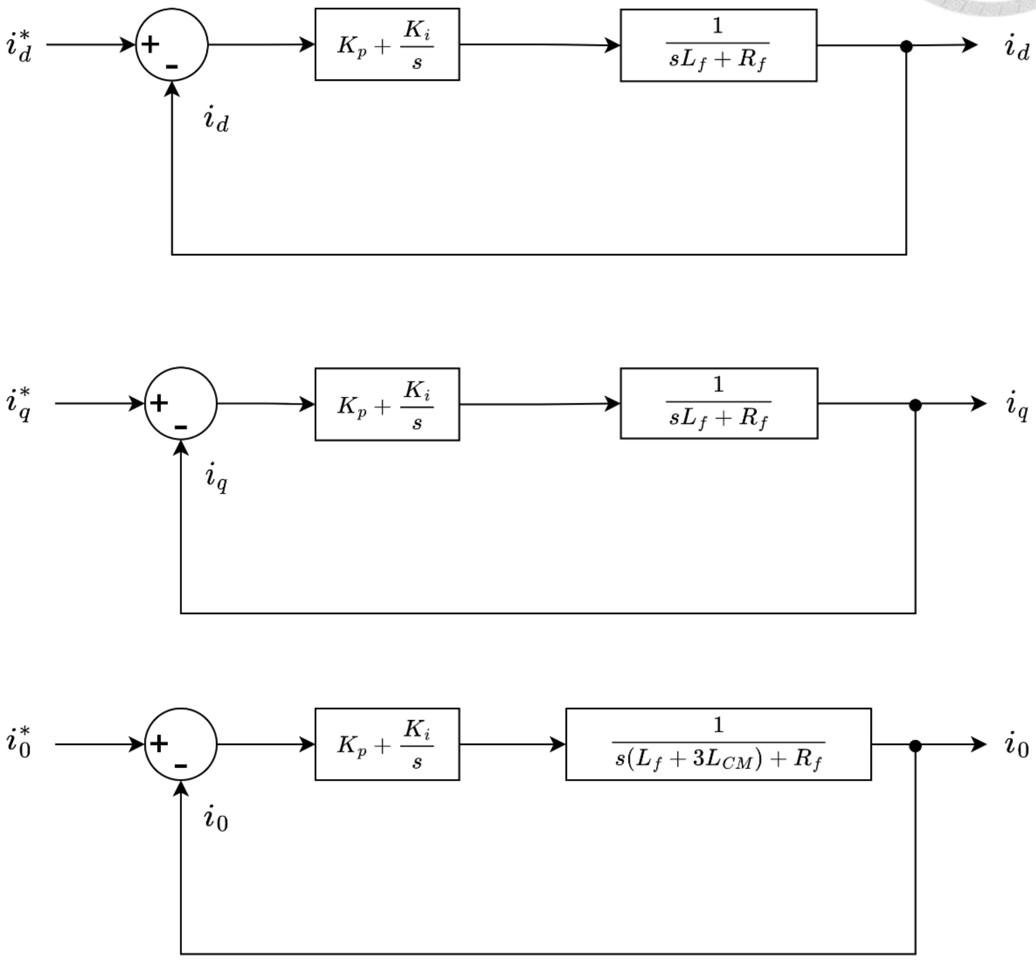

Fig. 3.4 The simplified closed-loop current control block diagram.

With the help of "decoupling ", the design procedures from the basic concepts of classical control theory can be applied for the PI control.

3.2.2 PI Control Design

Unfortunately, in the reality, it is needed to consider the overall time delay of the system when implementing a control design. This time delay can be introduced by different sources, such as sensor delay and processing delay. For simplification, in this

doi:10.6342/NTU202302551

thesis, the total delay for the PHIL is assumed as $1.5t_s$, where the t_s is the processing time per period. The closed-loop block diagram with time delay can be shown as Fig. 3.5.

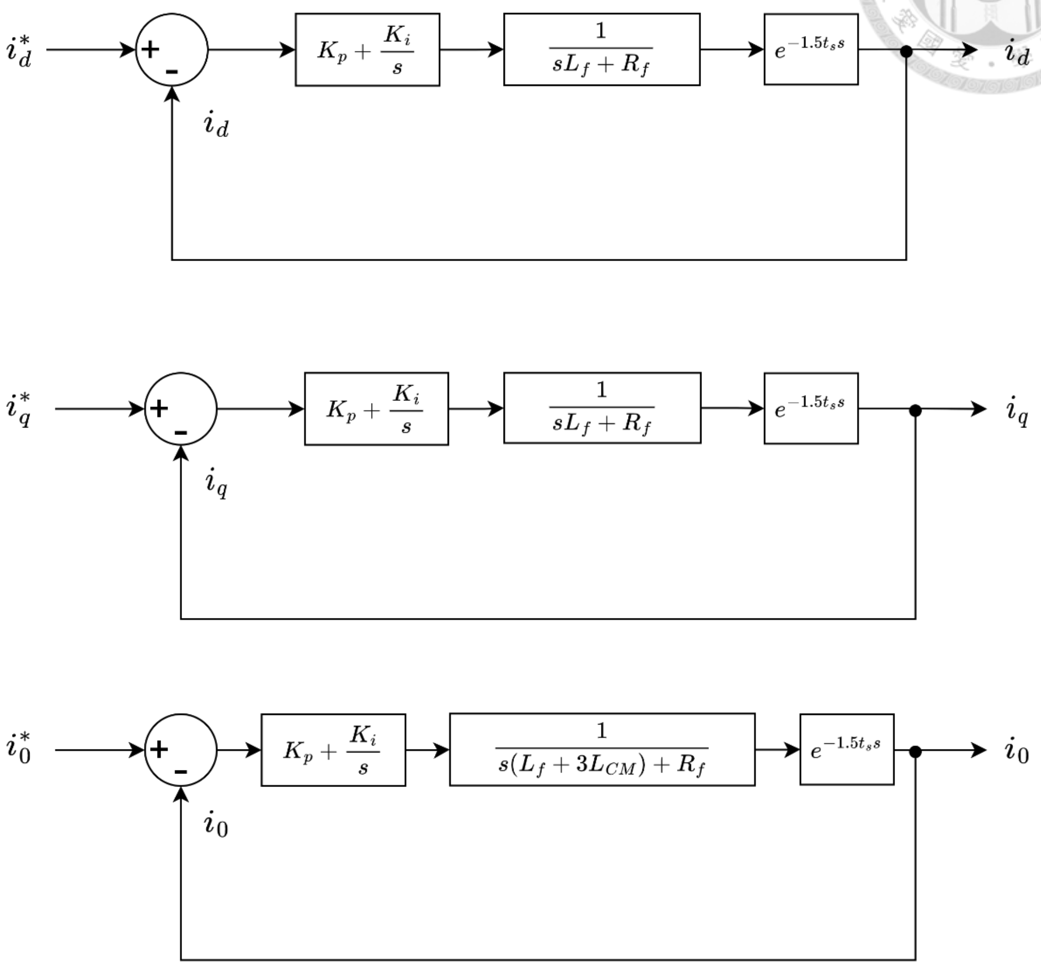

Fig. 3.5 The simplified closed-loop current control block diagram with time delay.

Since t_s is relatively small in PHIL application, which is 10μs in this thesis, the first order Padé approximant can be utilized, which can be expressed as (3.4), to represent the delay term in s-domain. Then, the control gain can be obtained by using root locus. It is worth noticing that the delay term provides a Left Half-Plane(LHP) pole and a Right Half-Plane(RHP) zero to the system. Put simply, the stability of the system is associated with the time delay. Thus, how to suppress the delay is another important research topic.

$$e^{-Ts} = \frac{1 - \frac{T}{2}s}{1 + \frac{T}{2}s} \tag{3.4}$$

doi:10.6342/NTU202302551

With the help of MATLAB, the control design can be effortless since MATLAB already have included the functions of Padé approximant and root locus. The design procedure of dq-axis control shown below is an example of how to design the PI control for a first order system.

First of all, by utilizing the well-known technique called "pole-zero cancellation", it can be found that the ratio of integral gain and proportional gain can be expressed as (3.5):

$$\frac{K_i}{K_p} = \frac{R_f}{L_f}. \tag{3.5}$$

In addition, the values of L_f and R_f are the measurements obtained from the real inductor used in the experiment, which are 2mH and 120mΩ, respectively. By substituting these parameters and utilizing the functions of Padé approximant and root locus, the root locus plot shown in Fig. 3.6 can be obtained.

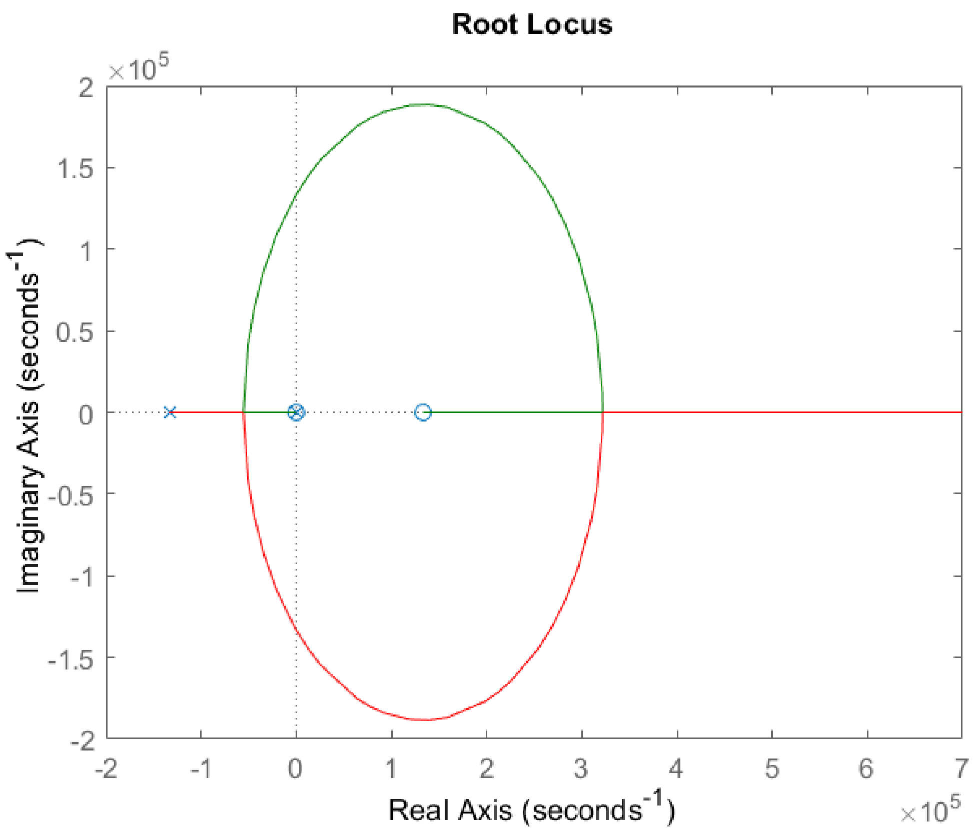

Fig. 3.6 The root locus plot of the dq-axis current control loop.

doi:10.6342/NTU202302551

Afterward, by using the root locus, the proportional gain can be found easily to match the desired performance, which is shown in Fig. 3.7.

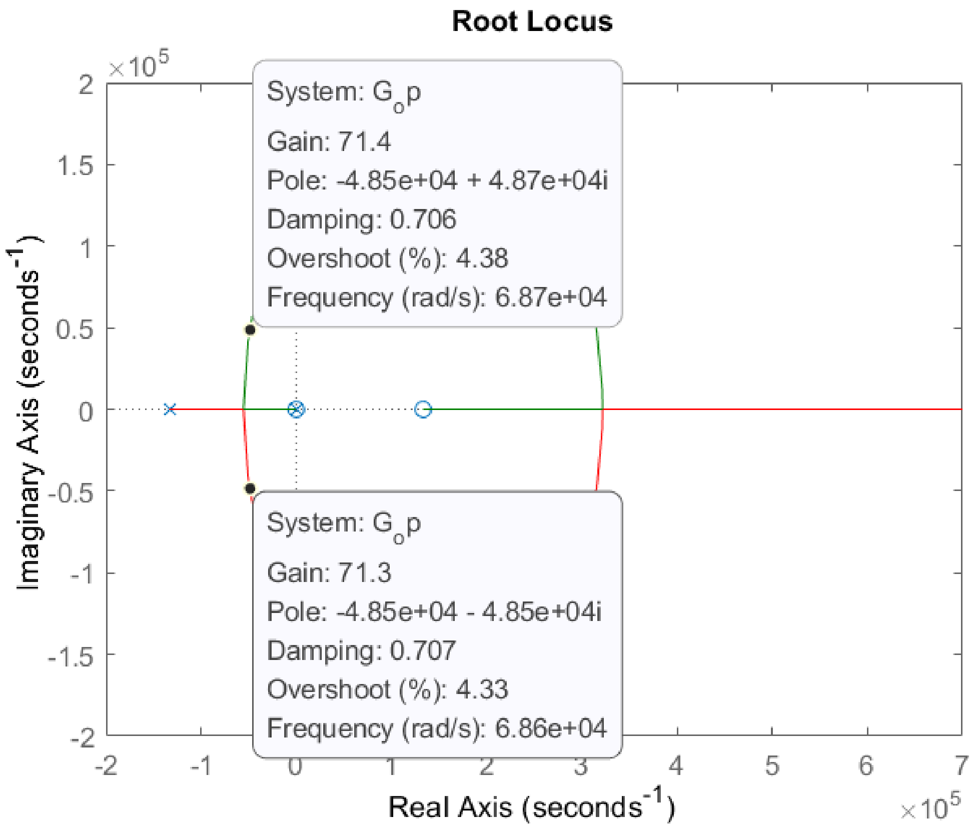

Fig. 3.7 The control design using root locus.

Finally, by using the results in Fig. 3.7, the proportional gain and integral gain are designed as (3.6), and the open-loop bode plot shown in Fig. 3.8 displays that the gain margin and the phase margin for the designed control loop are 11.4dB and 60deg, respectively. In this thesis, these control gains will be used in all the simulations and experiments.

$$\begin{cases} K_p = 70 \\ K_i = 4200 \end{cases} \tag{3.6}$$

doi:10.6342/NTU202302551

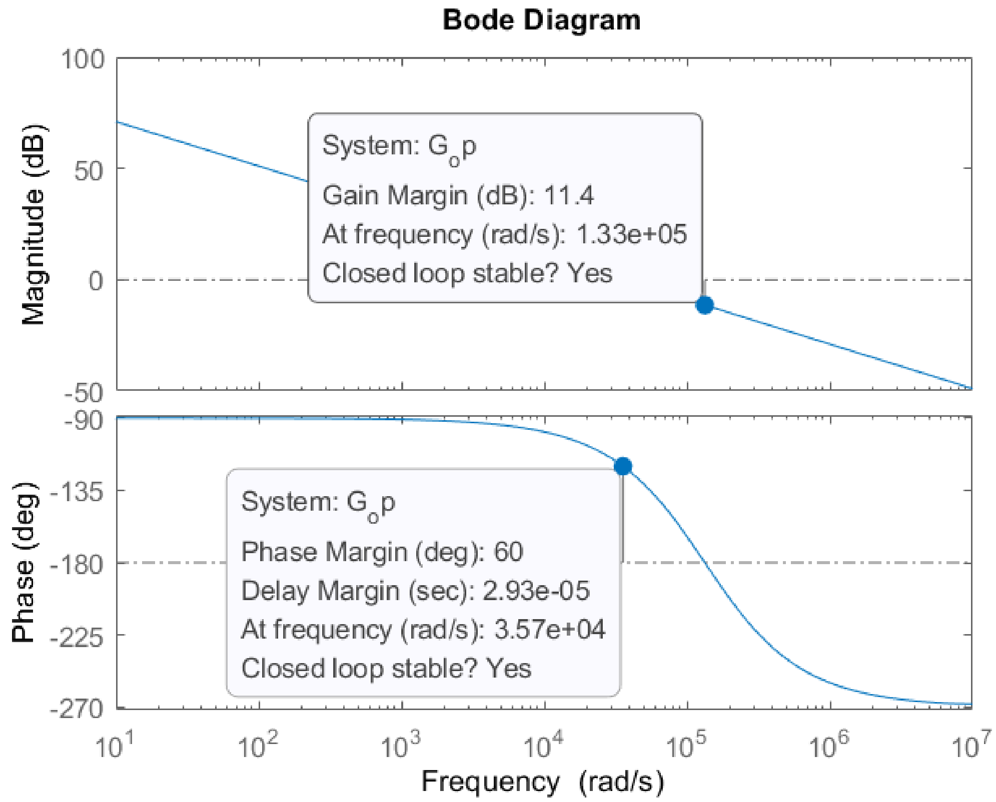

Fig. 3.8 The open-loop bode plot of the dq-axis current control loop.

3.3 Proposed CPIR Control

3.3.1 Introduction to DSRF Control Methodology

In addition to the normal operation of motors, negative sequence current present as a common feature of the three fault scenarios mentioned in this thesis. To deal with the negative sequence current, there are several control methodologies can suppress the negative current. The most used one is called Dual Synchronous Reference Frame (DSRF) control [44]-[48]. The block diagram of DSRF control is illustrated in Fig. 3.9, where i_{d+}^*, i_{q+}^*, i_{d-}^*, and i_{q-}^* are the reference currents in positive and negative sequence, meanwhile i_{d+}, i_{q+}, i_{d-}, and i_{q-} are the feedback currents in positive and negative sequence.

doi:10.6342/NTU202302551

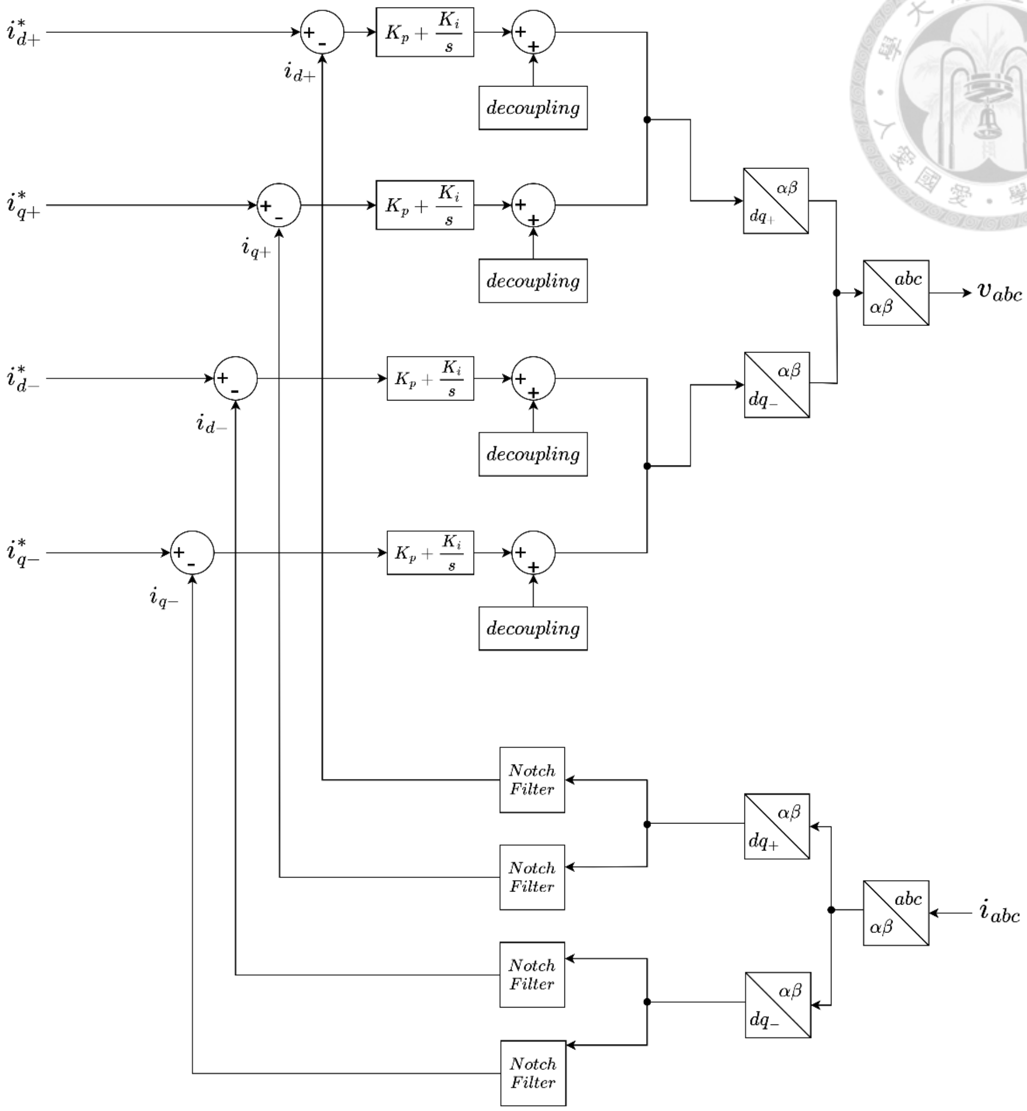

Fig. 3.9 The block diagram of DSRF control.

The main procedure of DSRF control can be divided into three steps:

First, the three-phase currents are transferred into positive reference frame and negative reference frame. This step first transfers the currents into stationary frame with αβ transform ($\boldsymbol{T_{\alpha\beta}}$), and then applies either positive dq transform ($\boldsymbol{T^{+}_{dq}}$) or negative dq transform ($\boldsymbol{T^{-}_{dq}}$) to the previous results. The transform matrices for these three transformations are shown in (3.7), (3.8), and (3.9), respectively:

doi:10.6342/NTU202302551

$$\boldsymbol{T_{\alpha\beta}} = \frac{2}{3}\begin{bmatrix} 1 & -\frac{1}{2} & -\frac{1}{2} \\ 0 & \frac{\sqrt{3}}{2} & -\frac{\sqrt{3}}{2} \\ 0 & -\frac{\sqrt{3}}{2} & \frac{\sqrt{3}}{2} \end{bmatrix} \tag{3.7}$$

$$\boldsymbol{T_{dq}^{+}} = \begin{bmatrix} \cos(\theta) & \sin(\theta) \\ -\sin(\theta) & \cos(\theta) \end{bmatrix} \tag{3.8}$$

$$\boldsymbol{T_{dq}^{-}} = \begin{bmatrix} \cos(\theta) & -\sin(\theta) \\ \sin(\theta) & \cos(\theta) \end{bmatrix}. \tag{3.9}$$

After applying the transformations for the feedback currents, it can be found that the transformed currents in positive reference frame consists of positive sequence current as DC term and negative sequence current as second harmonic term, and vice versa for the ones in negative reference frame. Thus, in this thesis, i_d^{p2n} and i_q^{p2n} are defined as the transformed dq-axis currents from positive sequence to negative sequence, and i_d^{n2p} and i_q^{n2p} as the ones from negative to positive. By utilizing these definitions, the transformed currents can be expressed as:

$$\boldsymbol{T_{dq}^{+}}\boldsymbol{T_{\alpha\beta}}\begin{bmatrix} i_a \\ i_b \\ i_c \end{bmatrix} = \begin{bmatrix} i_{d+} + i_d^{n2p} \\ i_{q+} + i_q^{n2p} \end{bmatrix} \tag{3.10}$$

$$\boldsymbol{T_{dq}^{-}}\boldsymbol{T_{\alpha\beta}}\begin{bmatrix} i_a \\ i_b \\ i_c \end{bmatrix} = \begin{bmatrix} i_{d-} + i_d^{p2n} \\ i_{q-} + i_q^{p2n} \end{bmatrix}. \tag{3.11}$$

In the second step, the notch filter is utilized to filter out the second harmonic term, so that the filtered current only has the DC term which can be regulated without steady-state error by a PI controller theoretically. The transform process of the feedback currents in DSRF control is depicted in Fig. 3.10. By referring to Fig. 3.10, a clearer understanding of the purpose and objectives of these transformations can be obtained.

doi:10.6342/NTU202302551

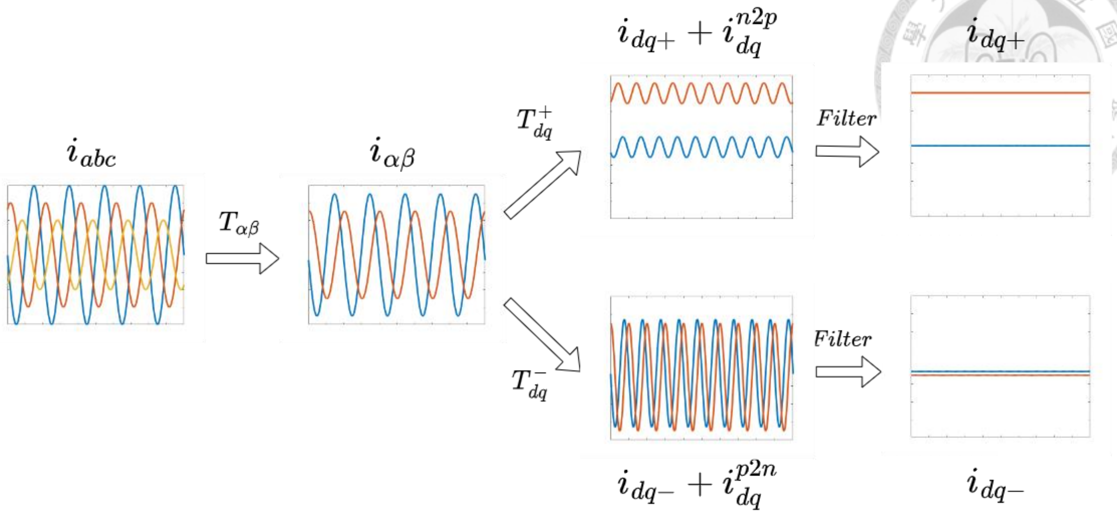

Fig. 3.10 The transform process of the feedback current in DSRF control.

Finally, using the traditional control design mentioned in Section 3.2 , the PI controller in each sequence can be well-designed and regulate the dq-axis feedback currents separately.

DSRF methodology can be implemented in motor driver or grid-tie inverter, but it is not suitable for the PHIL application for many concerns. For example, the usage of notch filter limits the transient response performance for the current control, and DSRF methodology requires lots of computational resources in the MCU because the reference currents from motor model need to be separated into positive and negative sequence, too. That is to say, additional notch filters are needed for the sequence separation in the PHIL application. Therefore, an improved method called Coupling-Proportional-Integral-Resonant (CPIR) control is proposed in this thesis to compensate the drawbacks of DSRF control methodology.

3.3.2 Derivation of CPIR Control

The most important idea about CPIR control is to utilize the structure of DSRF control mentioned in Section 3.3.1 . The PI controller in negative sequence is transformed

doi:10.6342/NTU202302551

to positive sequence, and then the results are combined with the original PI controller in positive sequence to form a new controller. The overall derivation of CPIR is shown as follows:

First of all, the negative-to-positive transform matrix ($\boldsymbol{T^{n2p}}$) and the inverse matrix, which is the positive-to-negative transform matrix ($\boldsymbol{T^{p2n}}$), are introduced in (3.12) and (3.13), respectively. It is worth noting that since the positive sequence rotates in the same direction as the motor, while the negative sequence rotates in the opposite direction. Consequently, the angular velocity difference between these two sequences is 2ω. Moreover, by utilizing (3.12) and (3.13), (3.10) and (3.11) can be further expressed as (3.14).

$$\boldsymbol{T^{n2p}} = \begin{bmatrix} \cos(2\omega t) & -\sin(2\omega t) \\ \sin(2\omega t) & \cos(2\omega t) \end{bmatrix} \tag{3.12}$$

$$\boldsymbol{T^{p2n}} = (\boldsymbol{T^{n2p}})^{-1} = \begin{bmatrix} \cos(2\omega t) & \sin(2\omega t) \\ -\sin(2\omega t) & \cos(2\omega t) \end{bmatrix} \tag{3.13}$$

$$\begin{bmatrix} i_{dq+} + i_{dq}^{n2p} \\ i_{dq-} + i_{dq}^{p2n} \end{bmatrix} = \begin{bmatrix} i_{dq+} + \boldsymbol{T^{n2p}} i_{dq-} \\ i_{dq-} + \boldsymbol{T^{p2n}} i_{dq+} \end{bmatrix} \tag{3.14}$$

In order to transform the PI controller in the negative sequence to the positive sequence, it is necessary to apply the sequence transformations described in (3.12) and (3.13). Note that these sequence transformations are defined in the time domain. Therefore, prior to applying the sequence transformations, the PI controller in the s-domain needs to be transformed into the time domain. The control outputs in negative sequence ,v_{d-} and v_{q-}, are represented in both the s-domain and the time domain as shown in (3.15) and (3.16). In these equations, i_{de-} and i_{qe-} represent the errors between the reference current and the feedback current in negative sequence. It is important to note that the representation of the PI controller is denoted as $C(s)$ in the s-domain, and its representation in the time domain is given by $c(t)$.

doi:10.6342/NTU202302551

$$\begin{bmatrix} v_{d-}(s) \\ v_{q-}(s) \end{bmatrix} = \begin{bmatrix} K_p + \frac{K_i}{s} & 0 \\ 0 & K_p + \frac{K_i}{s} \end{bmatrix} \begin{bmatrix} i_{de-}(s) \\ i_{qe-}(s) \end{bmatrix} = \begin{bmatrix} C(s) & 0 \\ 0 & C(s) \end{bmatrix} \begin{bmatrix} i_{de-}(s) \\ i_{qe-}(s) \end{bmatrix} \tag{3.15}$$

$$\mathcal{L}^{-1}\left\{\begin{bmatrix} v_{d-}(s) \\ v_{q-}(s) \end{bmatrix}\right\} = \begin{bmatrix} v_{d-}(t) \\ v_{q-}(t) \end{bmatrix} = \begin{bmatrix} c(t) & 0 \\ 0 & c(t) \end{bmatrix} * \begin{bmatrix} i_{de-}(t) \\ i_{qe-}(t) \end{bmatrix} \tag{3.16}$$

Note that a multiplication in the time domain becomes a convolution in the s-domain. After the inverse Laplace transform, the negative-to-positive transform matrix ($\boldsymbol{T^{n2p}}$) can be applied to the time-domain control outputs, which is shown as:

$$\boldsymbol{T^{n2p}} \begin{bmatrix} v_{d-}(t) \\ v_{q-}(t) \end{bmatrix} = \boldsymbol{T^{n2p}} \begin{bmatrix} c(t) & 0 \\ 0 & c(t) \end{bmatrix} * \begin{bmatrix} i_{de-}(t) \\ i_{qe-}(t) \end{bmatrix}. \tag{3.17}$$

In this thesis, the transformed dq-axis voltages and current errors from negative sequence to positive sequence are defined as v_d^{n2p}, v_q^{n2p}, i_{de}^{n2p}, and i_{qe}^{n2p}. The definitions are shown in (3.18) and (3.19):

$$\begin{bmatrix} v_d^{n2p}(t) \\ v_q^{n2p}(t) \end{bmatrix} = \boldsymbol{T^{n2p}} \begin{bmatrix} v_{d-}(t) \\ v_{q-}(t) \end{bmatrix} \tag{3.18}$$

$$\begin{bmatrix} i_{de}^{n2p}(t) \\ i_{qe}^{n2p}(t) \end{bmatrix} = \boldsymbol{T^{n2p}} \begin{bmatrix} i_{de-}(t) \\ i_{qe-}(t) \end{bmatrix}. \tag{3.19}$$

With these definitions, the equations shown in (3.17) can be rewritten as (3.20), and by substituting $\boldsymbol{T^{n2p}}$ and $\boldsymbol{T^{p2n}}$ matrix with the result shown in (3.12) and (3.13), the expanded equations can be obtained as (3.21) and (3.22).

$$\begin{bmatrix} v_d^{n2p}(t) \\ v_q^{n2p}(t) \end{bmatrix} = \boldsymbol{T^{n2p}} \begin{bmatrix} c(t) & 0 \\ 0 & c(t) \end{bmatrix} * (\boldsymbol{T^{n2p}})^{-\boldsymbol{1}} \begin{bmatrix} i_{de}^{n2p}(t) \\ i_{qe}^{n2p}(t) \end{bmatrix} \tag{3.20}$$

$$\begin{aligned} v_d^{n2p}(t) = {} & \cos(2\omega t)\, c(t) * \cos(2\omega t)\, i_{de}^{n2p}(t) \\ & - \cos(2\omega t)\, c(t) * \sin(2\omega t)\, i_{qe}^{n2p}(t) \\ & + \sin(2\omega t)\, c(t) * \sin(2\omega t) i_{de}^{n2p}(t) \\ & + \sin(2\omega t) c(t) * \cos(2\omega t)\, i_{qe}^{n2p}(t) \end{aligned} \tag{3.21}$$

doi:10.6342/NTU202302551

$$
\begin{aligned}
v_q^{n2p}(t) = &-\sin(2\omega t)\,c(t) * \cos(2\omega t)\,i_{de}^{n2p}(t) \\
&+\sin(2\omega t)\,c(t) * \sin(2\omega t)\,i_{qe}^{n2p}(t) \\
&+\cos(2\omega t)\,c(t) * \sin(2\omega t) i_{de}^{n2p}(t) \\
&+\cos(2\omega t) c(t) * \cos(2\omega t)\,i_{qe}^{n2p}(t)
\end{aligned} \tag{3.22}
$$

Next, the results from (3.21) and (3.22) can be transformed back to the s-domain, so that they can be combined with the original PI controller in positive sequence.

By utilizing the Laplace transform of sine and cosine functions shown in (3.23) and (3.24), $v_d^{n2p}(t)$ and $v_q^{n2p}(t)$ can be transformed back to s-domain and get further simplified. The results after the simplification are expressed in (3.25) and (3.26).

$$
\mathcal{L}\{\cos(\omega t)\cdot f(t)\} = \frac{s}{s^2+\omega^2} * F(s) = \frac{1}{2}[F(s+j\omega) + F(s-j\omega)] \tag{3.23}
$$

$$
\mathcal{L}\{\sin(\omega t)\cdot f(t)\} = \frac{\omega}{s^2+\omega^2} * F(s) = \frac{j}{2}[F(s+j\omega) - F(s-j\omega)] \tag{3.24}
$$

$$
\begin{aligned}
\mathcal{L}\left\{v_d^{n2p}(t)\right\} = &\frac{s}{s^2+4\omega^2} * \left\{C(s)\left[\frac{1}{2}\left(i_{de}^{n2p}(s+j2\omega) + i_{de}^{n2p}(s-j2\omega)\right)\right]\right\} \\
&-\frac{s}{s^2+4\omega^2} * \left\{C(s)\left[\frac{j}{2}\left(i_{qe}^{n2p}(s+j2\omega) - i_{qe}^{n2p}(s-j2\omega)\right)\right]\right\} \\
&+\frac{2\omega}{s^2+4\omega^2} * \left\{C(s)\left[\frac{j}{2}\left(i_{de}^{n2p}(s+j2\omega) - i_{de}^{n2p}(s-j2\omega)\right)\right]\right\} \\
&+\frac{2\omega}{s^2+4\omega^2} * \left\{C(s)\left[\frac{1}{2}\left(i_{qe}^{n2p}(s+j2\omega) + i_{qe}^{n2p}(s-j2\omega)\right)\right]\right\} \\
= &\frac{1}{4}\{C(s+j2\omega)\left[i_{de}^{n2p}(s+j4\omega) + i_{de}^{n2p}(s)\right] \\
&+C(s-j2\omega)\left[i_{de}^{n2p}(s) + i_{de}^{n2p}(s-j4\omega)\right]\} \\
&-\frac{j}{4}\{C(s+j2\omega)\left[i_{qe}^{n2p}(s+j4\omega) - i_{qe}^{n2p}(s)\right] \\
&+C(s-j2\omega)\left[i_{de}^{n2p}(s) - i_{de}^{n2p}(s-j4\omega)\right]\} \\
&-\frac{1}{4}\{C(s+j2\omega)\left[i_{de}^{n2p}(s+j4\omega) - i_{de}^{n2p}(s)\right] \\
&-C(s-j2\omega)\left[i_{de}^{n2p}(s) - i_{de}^{n2p}(s-j4\omega)\right]\} \\
&-\frac{j}{4}\{C(s+j2\omega)\left[i_{qe}^{n2p}(s+j4\omega) + i_{qe}^{n2p}(s)\right] \\
&-C(s-j2\omega)\left[i_{de}^{n2p}(s) + i_{de}^{n2p}(s-j4\omega)\right]\} \\
= &\frac{1}{2}[C(s+j2\omega) + C(s-j2\omega)] i_{de}^{n2p}(s) \\
&+\frac{j}{2}[C(s+j2\omega) - C(s-j2\omega)] i_{qe}^{n2p}(s)
\end{aligned} \tag{3.25}
$$

doi:10.6342/NTU202302551

$$
\begin{aligned}
\mathcal{L}\{v_q^{n2p}(t)\} = &-\frac{2\omega}{s^2+4\omega^2} * \left\{C(s)\left[\frac{1}{2}\left(i_{de}^{n2p}(s+j2\omega)+i_{de}^{n2p}(s-j2\omega)\right)\right]\right\} \\
&+\frac{2\omega}{s^2+4\omega^2} * \left\{C(s)\left[\frac{j}{2}\left(i_{qe}^{n2p}(s+j2\omega)-i_{qe}^{n2p}(s-j2\omega)\right)\right]\right\} \\
&+\frac{s}{s^2+4\omega^2} * \left\{C(s)\left[\frac{j}{2}\left(i_{de}^{n2p}(s+j2\omega)-i_{de}^{n2p}(s-j2\omega)\right)\right]\right\} \\
&+\frac{s}{s^2+4\omega^2} * \left\{C(s)\left[\frac{1}{2}\left(i_{qe}^{n2p}(s+j2\omega)+i_{qe}^{n2p}(s-j2\omega)\right)\right]\right\} \\
= &-\frac{j}{4}\{C(s+j2\omega)\left[i_{de}^{n2p}(s+j4\omega)+i_{de}^{n2p}(s)\right] \\
&-C(s-j2\omega)\left[i_{de}^{n2p}(s)+i_{de}^{n2p}(s-j4\omega)\right]\} \\
&-\frac{1}{4}\{C(s+j2\omega)\left[i_{qe}^{n2p}(s+j4\omega)-i_{qe}^{n2p}(s)\right] \\
&-C(s-j2\omega)\left[i_{qe}^{n2p}(s)-i_{qe}^{n2p}(s-j4\omega)\right]\} \\
&+\frac{j}{4}\{C(s+j2\omega)\left[i_{de}^{n2p}(s+j4\omega)-i_{de}^{n2p}(s)\right] \\
&+C(s-j2\omega)\left[i_{de}^{n2p}(s)-i_{de}^{n2p}(s-j4\omega)\right]\} \\
&+\frac{1}{4}\{C(s+j2\omega)\left[i_{qe}^{n2p}(s+j4\omega)+i_{qe}^{n2p}(s)\right] \\
&+C(s-j2\omega)\left[i_{qe}^{n2p}(s)+i_{qe}^{n2p}(s-j4\omega)\right]\} \\
= &-\frac{j}{2}[C(s+j2\omega)-C(s-j2\omega)]i_{de}^{n2p}(s) \\
&+\frac{1}{2}[C(s+j2\omega)+C(s-j2\omega)]i_{qe}^{n2p}(s) \qquad (3.26)
\end{aligned}
$$

By substituting the definition of C(s) shown in (3.15) back to (3.25) and (3.26), the final form of the control outputs transformed from negative sequence to positive sequence can be obtained. The results are shown in (3.27) and (3.28).

$$
\begin{aligned}
v_d^{n2p}(s) &= \frac{1}{2}[C(s+j2\omega)+C(s-j2\omega)]i_{de}^{n2p}(s) \\
&\quad+\frac{j}{2}[C(s+j2\omega)-C(s-j2\omega)]i_{qe}^{n2p}(s) \\
&= \frac{1}{2}\left[K_p+\frac{K_i}{s+j2\omega}+K_p+\frac{K_i}{s-j2\omega}\right]i_{de}^{n2p}(s) \\
&\quad+\frac{j}{2}\left[K_p+\frac{K_i}{s+j2\omega}-K_p-\frac{K_i}{s-j2\omega}\right]i_{qe}^{n2p}(s) \\
&= \left[K_p+\frac{K_i s}{s^2+4\omega^2}\right]i_{de}^{n2p}(s)+\left[\frac{2\omega K_i}{s^2+4\omega^2}\right]i_{qe}^{n2p}(s) \qquad (3.27)
\end{aligned}
$$

doi:10.6342/NTU202302551

$$
\begin{aligned}
v_q^{n2p}(s) &= -\frac{j}{2}[C(s+j2\omega)-C(s-j2\omega)]i_{de}^{n2p}(s) \\
&\quad +\frac{1}{2}[C(s+j2\omega)+C(s-j2\omega)]i_{qe}^{n2p}(s) \\
&= -\frac{j}{2}\left[K_p+\frac{K_i}{s+j2\omega}-K_p-\frac{K_i}{s-j2\omega}\right]i_{de}^{n2p}(s) \\
&\quad +\frac{1}{2}\left[K_p+\frac{K_i}{s+j2\omega}+K_p+\frac{K_i}{s-j2\omega}\right]i_{qe}^{n2p}(s) \\
&= \left[-\frac{2\omega K_i}{s^2+4\omega^2}\right]i_{de}^{n2p}(s)+\left[K_p+\frac{K_i s}{s^2+4\omega^2}\right]i_{qe}^{n2p}(s)
\end{aligned} \tag{3.28}
$$

The control law of the original PI controller in positive sequence can be expressed in (3.29):

$$
\begin{bmatrix} v_{d+}(s) \\ v_{q+}(s) \end{bmatrix} = \begin{bmatrix} K_p+\frac{K_i}{s} & 0 \\ 0 & K_p+\frac{K_i}{s} \end{bmatrix}\begin{bmatrix} i_{de+}(s) \\ i_{qe+}(s) \end{bmatrix}. \tag{3.29}
$$

Next, by combining (3.29) with (3.27) and (3.28), the control outputs in positive sequence can be expressed as:

$$
\begin{aligned}
\begin{bmatrix} v_{d+}(s)+v_d^{n2p}(s) \\ v_{q+}(s)+v_q^{n2p}(s) \end{bmatrix} &= \begin{bmatrix} K_p & 0 \\ 0 & K_p \end{bmatrix}\begin{bmatrix} i_{de+}(s)+i_{de}^{n2p}(s) \\ i_{qe+}(s)+i_{qe}^{n2p}(s) \end{bmatrix} \\
&\quad + \begin{bmatrix} \frac{K_i}{s} & 0 \\ 0 & \frac{K_i}{s} \end{bmatrix}\begin{bmatrix} i_{de+}(s) \\ i_{qe+}(s) \end{bmatrix} \\
&\quad + \begin{bmatrix} \frac{K_i s}{s^2+4\omega^2} & \frac{2\omega K_i}{s^2+4\omega^2} \\ -\frac{2\omega K_i}{s^2+4\omega^2} & \frac{K_i s}{s^2+4\omega^2} \end{bmatrix}\begin{bmatrix} i_{de}^{n2p}(s) \\ i_{qe}^{n2p}(s) \end{bmatrix}.
\end{aligned} \tag{3.30}
$$

Fig. 3.11 and Fig. 3.12 shows the bode plot of an integral term and a resonant term, where the word "resonant" is used to describe the phenomenon of increased magnitude that occurs when the frequency of an applied periodic force is equal or close to the natural frequency, which is often referred to the resonant frequency.

doi:10.6342/NTU202302551

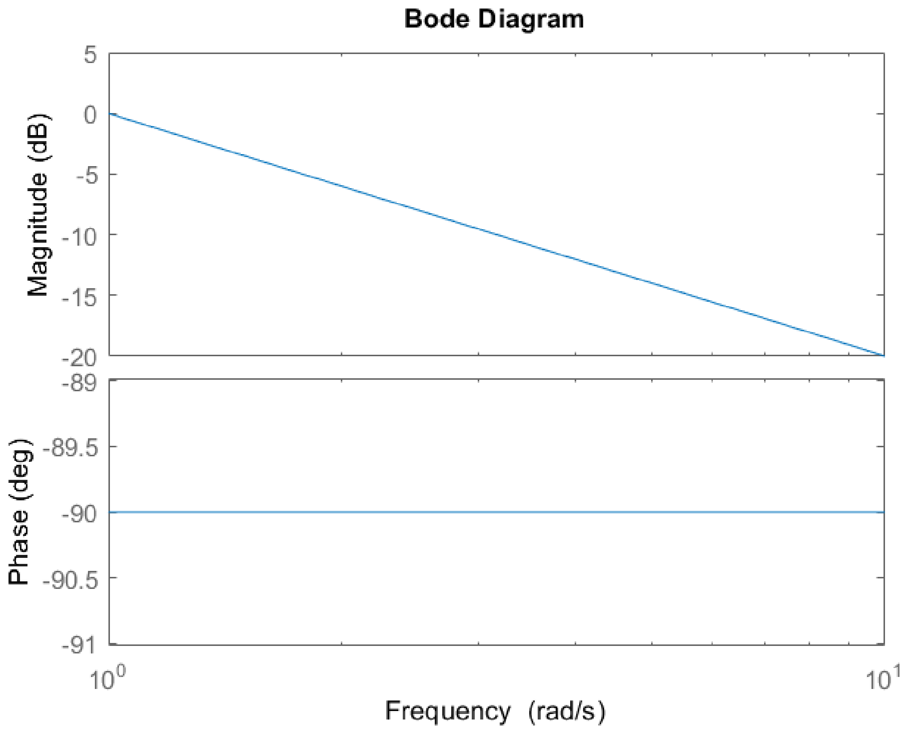

Fig. 3.11 The bode plot of an integral term.

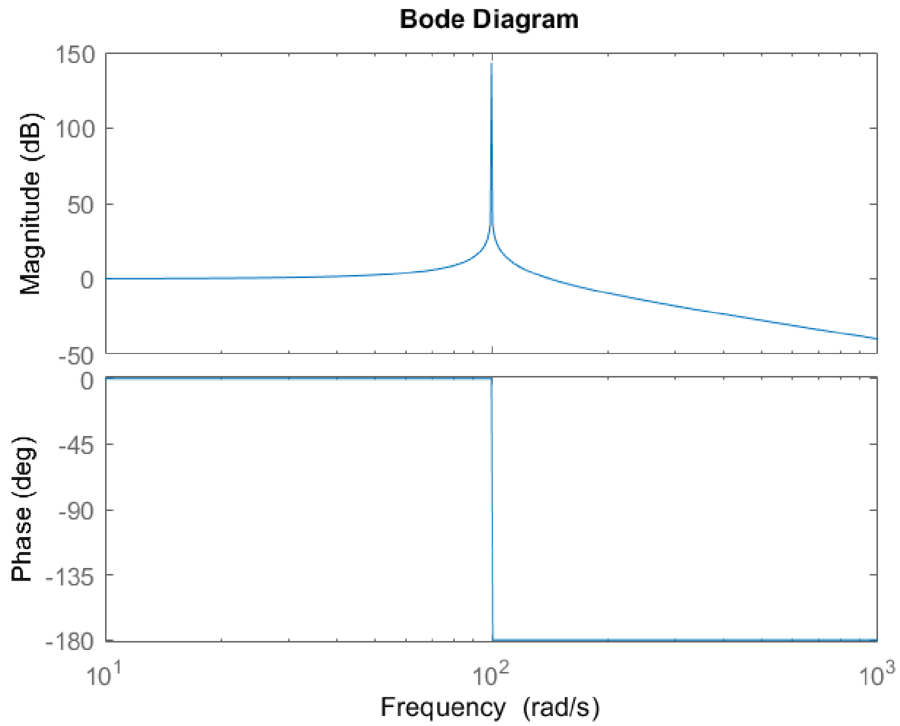

Fig. 3.12 The bode plot of a resonant term.

doi:10.6342/NTU202302551

By analyzing Fig. 3.11 and Fig. 3.12, it is evident that the contribution of second harmonic currents, which are i_{de}^{n2p} and i_{qe}^{n2p}, to the integral term is relatively small compared to the DC currents, which are i_{de+} and i_{qe+}, and vice versa for the resonant term. Therefore, the second harmonic currents and DC currents can be separately added to the integral term and resonant term without significantly impacting the results, which is shown as:

$$\begin{aligned}\begin{bmatrix} v_{d+}(s) + v_d^{n2p}(s) \\ v_{q+}(s) + v_q^{n2p}(s) \end{bmatrix} &= \begin{bmatrix} K_p & 0 \\ 0 & K_p \end{bmatrix} \begin{bmatrix} i_{de+}(s) + i_{de}^{n2p}(s) \\ i_{qe+}(s) + i_{qe}^{n2p}(s) \end{bmatrix} \\ &+ \begin{bmatrix} \frac{K_i}{s} & 0 \\ 0 & \frac{K_i}{s} \end{bmatrix} \begin{bmatrix} i_{de+}(s) + i_{de}^{n2p}(s) \\ i_{qe+}(s) + i_{de}^{n2p}(s) \end{bmatrix} \\ &+ \begin{bmatrix} \frac{K_i s}{s^2+4\omega^2} & \frac{2\omega K_i}{s^2+4\omega^2} \\ -\frac{2\omega K_i}{s^2+4\omega^2} & \frac{K_i s}{s^2+4\omega^2} \end{bmatrix} \begin{bmatrix} i_{de+}(s) + i_{de}^{n2p}(s) \\ i_{de+}(s) + i_{qe}^{n2p}(s) \end{bmatrix}. \end{aligned} \tag{3.31}$$

Finally, the control law of the proposed CPIR control can be expressed as:

$$\begin{bmatrix} v_d(s) \\ v_q(s) \end{bmatrix} = \begin{bmatrix} K_p + \frac{K_i}{s} + \frac{K_i s}{s^2+4\omega^2} & \frac{2\omega K_i}{s^2+4\omega^2} \\ -\frac{2\omega K_i}{s^2+4\omega^2} & K_p + \frac{K_i}{s} + \frac{K_i s}{s^2+4\omega^2} \end{bmatrix} \begin{bmatrix} i_{de}(s) \\ i_{qe}(s) \end{bmatrix} \tag{3.32}$$

where

$$\begin{bmatrix} v_d \\ v_q \end{bmatrix} = \boldsymbol{T}_{\boldsymbol{dq}}^{+} \boldsymbol{T}_{\boldsymbol{\alpha\beta}} \begin{bmatrix} v_a \\ v_b \\ v_c \end{bmatrix} = \begin{bmatrix} v_{d+} + v_d^{n2p} \\ v_{q+} + v_q^{n2p} \end{bmatrix} \tag{3.33}$$

$$\begin{bmatrix} i_{de} \\ i_{qe} \end{bmatrix} = \begin{bmatrix} i_d^* \\ i_q^* \end{bmatrix} - \boldsymbol{T}_{\boldsymbol{dq}}^{+} \boldsymbol{T}_{\boldsymbol{\alpha\beta}} \begin{bmatrix} i_a \\ i_b \\ i_c \end{bmatrix} = \begin{bmatrix} i_{de+} + i_{de}^{n2p} \\ i_{qe+} + i_{qe}^{n2p} \end{bmatrix}. \tag{3.34}$$

The block diagram of CPIR control is shown in Fig. 3.13. From Fig. 3.13, it is important to note that the CPIR control consists of two types of resonant controllers. The first one is the self-resonant controller, where the control input of each axis only affects the control output in its own axis. The second one is the coupling resonant controller,

doi:10.6342/NTU202302551

where the control input of each axis influences the control output in the opposite axis, acting as a coupling term. This is also the reason why the proposed control method in this thesis is called Coupling-Proportional-Integral-Resonant (CPIR) control.

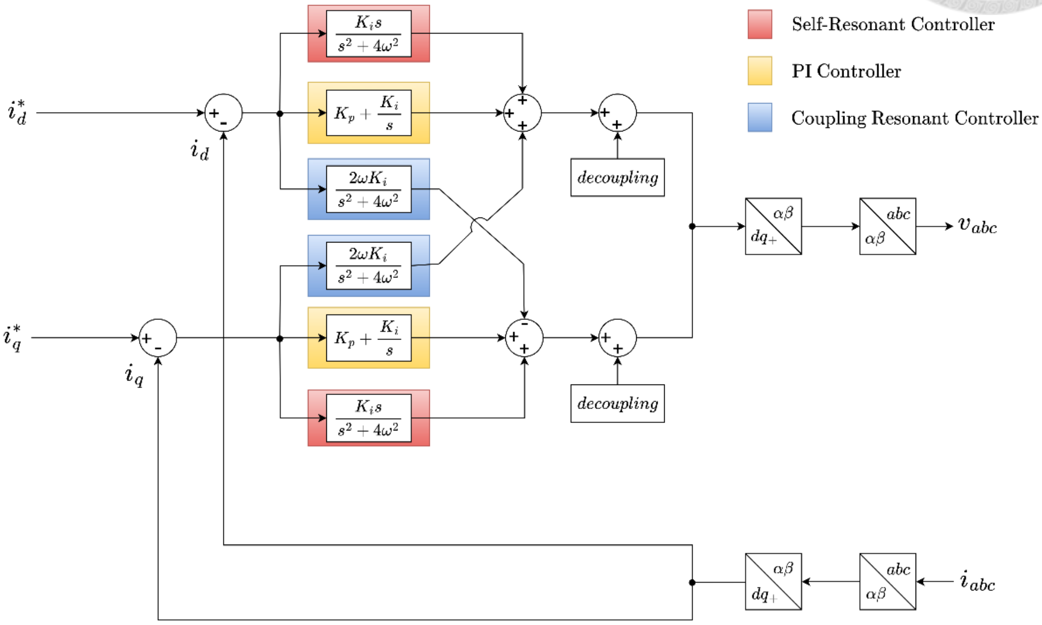

Fig. 3.13 The block diagram of CPIR control.

Comparing Fig. 3.13 to the block diagram of DSRF control shown in Fig. 3.9, it is worth noting that there is no need to separate the control system into positive and negative sequence when the CPIR control is adopted, which means there is no need to apply any notch filter for the implementation of PHIL. Therefore, the computational resources are saved, and the performance of the current control is not affected by the notch filters anymore.

3.4 Digital Control Implementation

Since the PHIL current control is implemented in the MCU, it is necessary to digitalize the continuous-time control law. The most common approach, which is adopted in this thesis, is implementing the control design in s-domain first, and then utilizing the

doi:10.6342/NTU202302551

s-to-z transform to obtain the discrete-time control law. Although it is suggested that the digital control design should be implemented in the z-domain directly to make account of the sampling effect [49].

The fundamental concept of s-to-z transform can be regarded as the relation between s plane and z plane shown in (3.35), where T is the sampling time for the digitalization.

$$\mathrm{z} = e^{sT} \tag{3.35}$$

Note that it is considered not suitable for the digital implementation since the exponential operation is resource-consuming. Thus, there are lots of different methods to work as the approximated approaches [50], [51]. The most popular method is Tustin's method, which is often referred as Bilinear transform. The Bilinear transform can be expressed as:

$$s = \frac{2(1 - z^{-1})}{T(1 + z^{-1})}. \tag{3.36}$$

Once the Bilinear transform is applied to transform the control law from the s-domain to the z-domain, the inverse Z-transform can be utilized to convert the control law from the z-domain to its discrete-time representation, which can be directly implemented in digital systems, such as microcontroller (MCU). The only inverse Z-transform used in this thesis can be expressed as:

$$x[n - m] = z^{-m}x[n] \tag{3.37}$$

where $x[n]$ is a signal in current step, $x[n-1]$ is a signal in previous or future m step, and m can be any integer.

From Fig. 3.13, it is evident that there are one PI controller and two different resonant controllers, namely the self-resonant controller and the coupling resonant controller, need to be converted. The converting results are shown as follows:

doi:10.6342/NTU202302551

A. PI controller:

To begin with, the block diagram of a PI controller in the time domain is shown in Fig. 3.14.

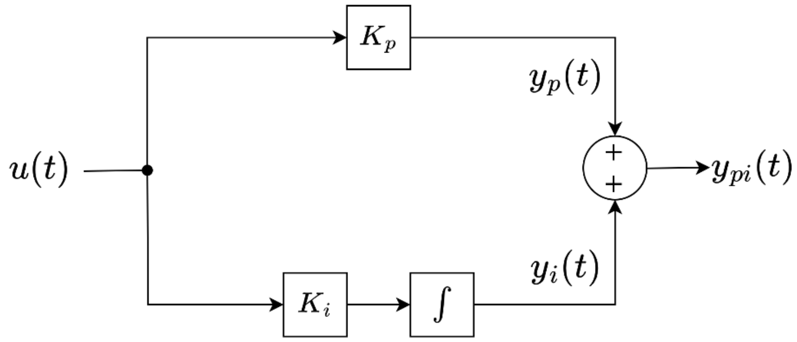

Fig. 3.14 The block diagram of a PI controller in the time domain.

From Fig. 3.14, the equations of the P-control output (y_p) and I-control output (y_i) in the time domain can be expressed as:

$$y_p(\mathrm{t}) = K_p u(t) \tag{3.38}$$

$$y_i(\mathrm{t}) = \int K_i \cdot u(t) dt \tag{3.39}$$

where u is the control input which can be referred as i_{de} or i_{qe} shown in (3.34).

Then, applying the Laplace transform to obtain the equations in the s-domain. The results can be shown as:

$$Y_P(s) = K_p U(s) \tag{3.40}$$

$$Y_I(s) = \frac{K_i}{s} U(s) \tag{3.41}$$

where $U(s)$, $Y_P(\mathrm{s})$, and $Y_I(\mathrm{s})$ are the control input, the P-control output, and the I-control output in the s-domain, respectively.

Next, applying the Bilinear transform, which is shown in (3.36), to obtain the equations in the z-domain. The results can be obtained as:

$$Y_P(z) = K_p U(z) \tag{3.42}$$

doi:10.6342/NTU202302551

$$Y_I(z) = K_i\left[\frac{T}{2}\frac{(1+z^{-1})}{(1-z^{-1})}\right]U(z)$$
$$= \frac{T}{2}K_i(1+z^{-1})U(z) + z^{-1}Y_I(z) \quad (3.43)$$

where $U(z)$, $Y_P(z)$, and $Y_I(z)$ are the control input, the P-control output, and the I-control output in the z-domain, respectively.

Subsequently, applying the inverse Z-transform, which is shown in (3.37), to obtain the discrete-time control outputs. The results can be expressed as:

$$Y_P[n] = K_p\mathrm{U}[n] \quad (3.44)$$

$$\mathrm{Y}_I[n] = \frac{T}{2}K_i(\mathrm{U}[n] + \mathrm{U}[n-1]) + \mathrm{Y}_I[n-1] \quad (3.45)$$

where $\mathrm{U}[n]$, $\mathrm{Y}_P[n]$, $\mathrm{Y}_I[n]$ are the discrete-time control input, P-control output, and I-control output in current step, respectively. Meanwhile, $\mathrm{U}[n-1]$ and $\mathrm{Y}_I[n-1]$ are the discrete-time control input and I-control output in previous step.

Eventually, the discrete-time control law of the PI controller can be obtained as:

$$\mathrm{Y}_{PI}[n] = Y_P[n] + \mathrm{Y}_I[n]$$
$$= K_p\mathrm{U}[n] + \frac{T}{2}K_i(\mathrm{U}[n] + \mathrm{U}[n-1]) + \mathrm{Y}_I[n-1] \quad (3.45)$$

B. Self-resonant controller

Next, the implementation of the self-resonant controller in this thesis is illustrated in Fig. 3.15.

doi:10.6342/NTU202302551

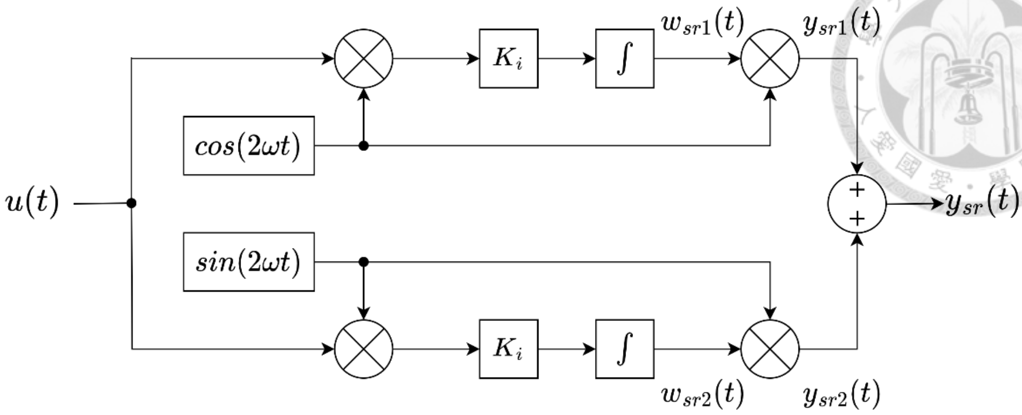

Fig. 3.15 The block diagram of the self-resonant controller.

The following derivation shows that Fig. 3.15 is equivalent to the definition shown in Fig. 3.13:

First of all, by using the block diagram shown in Fig. 3.15, the equations of w_{sr1} and w_{sr2} in time domain can be written as:

$$\begin{cases} w_{sr1}(t) = \int \cos(2\omega t) \cdot K_i \cdot u(t)\, dt \\ w_{sr2}(t) = \int \sin(2\omega t) \cdot K_i \cdot u(t)\, dt \end{cases} \tag{3.46}$$

Then, applying the Laplace transform to obtain the equations of W_{SR1} and W_{SR2} in s-domain. The results can be shown as:

$$\begin{cases} \mathcal{L}\{w_{sr1}(t)\} = W_{SR1}(s) = \dfrac{K_i}{2s}[U(s+j2\omega) + U(s-j2\omega)] \\ \mathcal{L}\{w_{sr2}(t)\} = W_{SR2}(s) = \dfrac{jK_i}{2s}[U(s+j2\omega) - U(s-j2\omega)] \end{cases} \tag{3.47}$$

After that, the output equation can be written down in time domain according to Fig. 3.15, and the results can be expressed as:

$$y_{sr}(t) = y_{sr1}(t) + y_{sr2}(t) = \cos(2\omega t)\, w_{sr1}(t) + \sin(2\omega t)\, w_{sr2}(t) \tag{3.48}$$

where y_{sr} is the control output of the self-resonant controller.

Then, applying Laplace transform to obtain the control law of the self-resonant controller in s-domain. The results can be obtained as:

doi:10.6342/NTU202302551

$$
\begin{aligned}
\mathcal{L}\{y_{sr}(t)\} = Y_{SR}(s) &= \frac{1}{2}[W_{SR1}(s+j2\omega)+W_{SR1}(s-j2\omega)] \\
&\quad + \frac{j}{2}[W_{SR2}(s+j2\omega)-W_{SR2}(s-j2\omega)] \\
&= \frac{K_i}{4(s+j2\omega)}[U(s)+U(s+j4\omega)] \\
&\quad + \frac{K_i}{4(s-j2\omega)}[U(s)+U(s-j4\omega)] \\
&\quad + \frac{K_i}{4(s+j2\omega)}[U(s)-U(s+j4\omega)] \\
&\quad + \frac{K_i}{4(s-j2\omega)}[U(s)-U(s-j4\omega)] \\
&= \left[\frac{K_i}{2(s+j2\omega)}+\frac{K_i}{2(s-j2\omega)}\right]U(s) \\
&= \frac{K_i s}{s^2+4\omega^2}U(s)
\end{aligned}
\tag{3.49}
$$

where the $Y_{SR}(\mathrm{s})$ is the control output of the self-resonant controller in s-domain, and it can be found that the results from (3.49) is equivalent to the expression of the self-resonant controller shown in Fig. 3.13.

More importantly, by utilizing the block diagram shown in Fig. 3.15 and applying the same transformation procedures for the PI controller, the discrete-time control law of the self-resonant controller can be expressed as:

$$\mathrm{Y}_{SR}[n] = \mathrm{Y}_{SR1}[n] + \mathrm{Y}_{SR2}[n] = \cos(2\theta[n])W_{SR1}[n] + \sin(2\theta[n])W_{SR2}[n] \tag{3.50}$$

where

$$\mathrm{W}_{SR1}[n] = \frac{T}{2}K_i[\cos(2\theta[n])\mathrm{U}[n] + \cos(2\theta[n-1])\mathrm{U}[n-1]] + \mathrm{Y}_{SR1}[n-1] \tag{3.51}$$

$$\mathrm{W}_{SR2}[n] = \frac{T}{2}K_i[\sin(2\theta[n])\mathrm{U}[n] + \sin(2\theta[n-1])\mathrm{U}[n-1]] + \mathrm{Y}_{SR2}[n-1]. \tag{3.52}$$

C. Coupling resonant controller

Moreover, the implementation of the coupling resonant controller in this thesis is displayed in Fig. 3.16.

doi:10.6342/NTU202302551

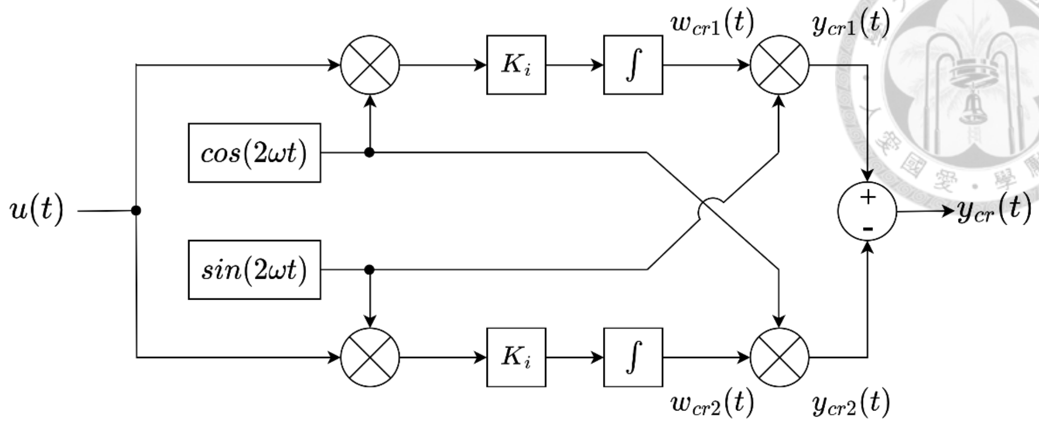

Fig. 3.16 The block diagram of the coupling resonant controller.

The following derivation shows that Fig. 3.16 is equivalent to the definition shown in Fig. 3.13:

First of all, by using the block diagram shown in Fig. 3.16, the equations of w_{cr1} and w_{cr2} in time domain can be written as:

$$\begin{cases} w_{cr1}(t) = \int \cos(2\omega t) \cdot K_i \cdot u(t)\, dt \\ w_{cr2}(t) = \int \sin(2\omega t) \cdot K_i \cdot u(t)\, dt \end{cases} \tag{3.53}$$

Then, applying the Laplace transform to obtain the equations of W_{CR1} and W_{CR2} in s-domain. The results can be shown as:

$$\begin{cases} \mathcal{L}\{w_{cr1}(t)\} = W_{CR1}(s) = \dfrac{K_i}{2s}[U(s+j2\omega) + U(s-j2\omega)] \\ \mathcal{L}\{w_{cr2}(t)\} = W_{CR2}(s) = \dfrac{jK_i}{2s}[U(s+j2\omega) - U(s-j2\omega)] \end{cases} \tag{3.54}$$

After that, the output equation can be written down in time domain according to Fig. 3.16, and the results can be expressed as:

$$y_{cr}(t) = y_{cr1}(t) - y_{cr2}(t) = \sin(2\omega t)\, w_{cr1}(t) - \cos(2\omega t)\, w_{cr2}(t) \tag{3.55}$$

where y_{sr} is the control output of the coupling-resonant controller.

Then, applying Laplace transform to obtain the control law of the coupling resonant controller in s-domain. The results can be obtained as:

doi:10.6342/NTU202302551

$$
\begin{aligned}
\mathcal{L}\{y_{cr}(t)\} = Y_{CR}(s) &= \frac{j}{2}[W_{CR1}(s+j2\omega) - W_{CR1}(s-j2\omega)] \\
&\quad -\frac{1}{2}[W_{CR2}(s+j2\omega) + W_{CR2}(s-j2\omega)] \\
&= \frac{jK_i}{4(s+j2\omega)}[U(s) + U(s+j4\omega)] \\
&\quad -\frac{jK_i}{4(s-j2\omega)}[U(s) + U(s-j4\omega)] \\
&\quad +\frac{jK_i}{4(s+j2\omega)}[U(s) - U(s+j4\omega)] \\
&\quad -\frac{K_i}{4(s-j2\omega)}[U(s) - U(s-j4\omega)] \\
&= \left[\frac{jK_i}{2(s+j2\omega)} - \frac{jK_i}{2(s-j2\omega)}\right]U(s) \\
&= \frac{2\omega K_i}{s^2+4\omega^2}U(s)
\end{aligned}
\tag{3.56}
$$

where the $Y_{CR}(\mathrm{s})$ is the control output of the coupling resonant controller in s-domain, and it can be found that the results from (3.56) is equivalent to the expression of the coupling resonant controller shown in Fig. 3.13.

More importantly, by utilizing the block diagram shown in Fig. 3.16 and applying the same transformation procedures for the PI controller, the discrete-time control law of the coupling resonant controller can be expressed as:

$$
\mathrm{Y}_{CR}[n] = \mathrm{Y}_{CR1}[n] + \mathrm{Y}_{CR2}[n] = \sin(2\theta[n])W_{CR1}[n] - \cos(2\theta[n])W_{CR2}[n] \tag{3.57}
$$

where

$$
\mathrm{W}_{CR1}[n] = \frac{T}{2}K_i[\cos(2\theta[n])\mathrm{U}[n] + \cos(2\theta[n-1])\mathrm{U}[n-1]] + \mathrm{Y}_{CR1}[n-1] \tag{3.58}
$$

$$
\mathrm{W}_{CR2}[n] = \frac{T}{2}K_i[\sin(2\theta[n])\mathrm{U}[n] + \sin(2\theta[n-1])\mathrm{U}[n-1]] + \mathrm{Y}_{CR2}[n-1] \tag{3.59}
$$

Last but not least, it is important to highlight that the digital control implementation presented in this section enables the realization of both the traditional PI control and the proposed CPIR control. The subsequent step involves employing simulation tools to verify the improved performance of PHIL current control under different fault scenarios by adopting the CPIR control compared to the traditional PI control.

doi:10.6342/NTU202302551

Chapter 4 Computer Simulations

4.1 Simulation Environment

MATLAB & Simulink is utilized to run the PHIL-based motor test-bench simulations and to verify the performance of the proposed CPIR control compares to the traditional PI control in different fault scenarios. The specification of the PHIL-based motor test-bench and the emulated SPMSM can be found in Table 4.1 and

Table 4.2.

Table 4.1 Specification of the PHIL-based motor test-bench.

Parameters	Value
DC-link Voltage	400V
MUT Switching Frequency	9.5kHz
PHIL Switching Frequency	100kHz
Coupling Network Inductance	2mH
Coupling Network Resistance	120mΩ
Three-phase CMC Inductance	14mH
Three-phase CMC Resistance	80mΩ

Table 4.2 Specification of the emulated SPMSM.

Parameters	Value
Stator Resistance	0.2648Ω
Self-Inductance	1.27mH
Mutual Inductance	0.64mH
Flux Linkage	0.12414V·s/rad
Inertia	$0.0050\text{kg}\cdot\text{m}^2$
Friction Coefficient	$0.0044\text{kg}\cdot\text{m}^2\cdot\text{s}^{-1}$
Number of Poles	8

To verify the emulating performance, the simulation is divided into two parts:

First, a MUT is connected with a PHIL to create a PHIL-based motor test-bench, as

doi:10.6342/NTU202302551

shown in Fig. 4.1. For the MUT, FOC (see more in Appendix A.) is utilized to control the target motor in MUT, and then the control signals are sent to the MUT power stage, which is a three-phase inverter, to supply power to the motor. Simultaneously, the PHIL performs model calculations using a 312.5kHz modified Euler's method to compute the motor currents under different scenarios. After the calculations, the model currents serve as the reference signals for the PHIL current control, which employs various control methods. Eventually, the PHIL regulates the three-phase currents flowed through the PHIL power stage, consisting of a three-phase inverter, a coupling network, and a three-phase CMC, to accurately emulate the electrical behavior of the target motor.

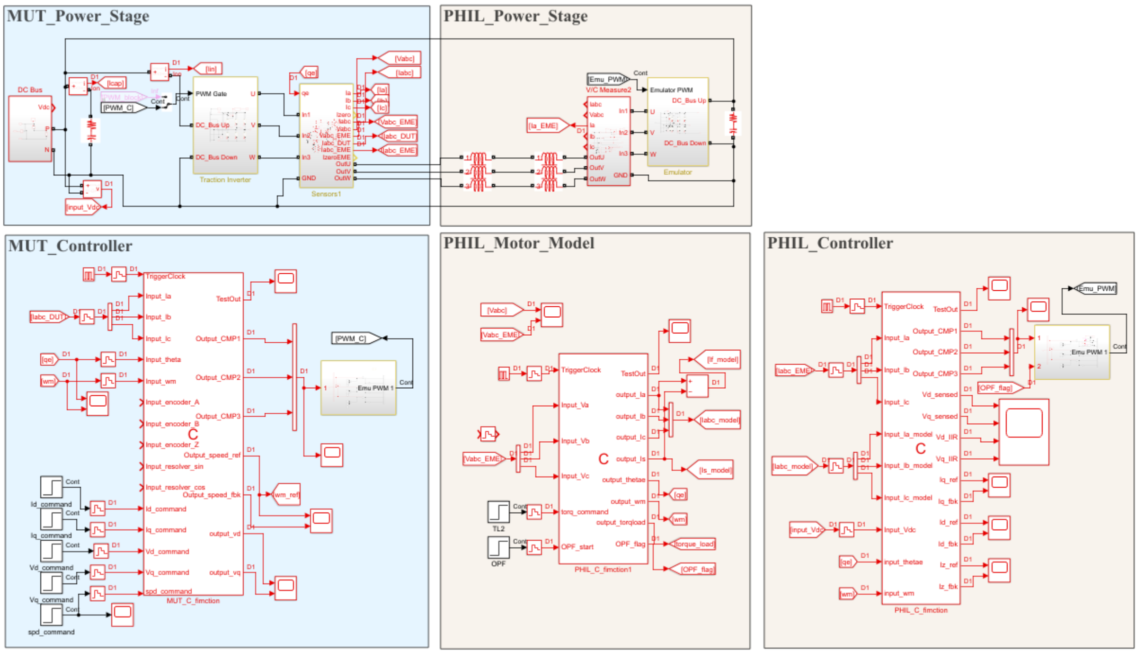

Fig. 4.1 Simulation diagram of PHIL-based motor test-bench.

Next, another MUT with identical specification is connected with a pure numerical model representing an ideal motor model, as depicted in Fig. 4.2. The MUT performs the same tasks as mentioned earlier. However, instead of being connected to a PHIL, it is connected to a motor model that uses a 4MHz forward Euler's method to calculate the model currents. This high calculating frequency ensures highly accurate model currents, as it is significantly higher than the switching frequency of the MUT. Therefore, the

doi:10.6342/NTU202302551

calculated currents from this model can be regarded as the ideal currents, serving as a reference standard for comparing and verifying the performance of the PHIL-based motor test-bench in both simulation and experiment.

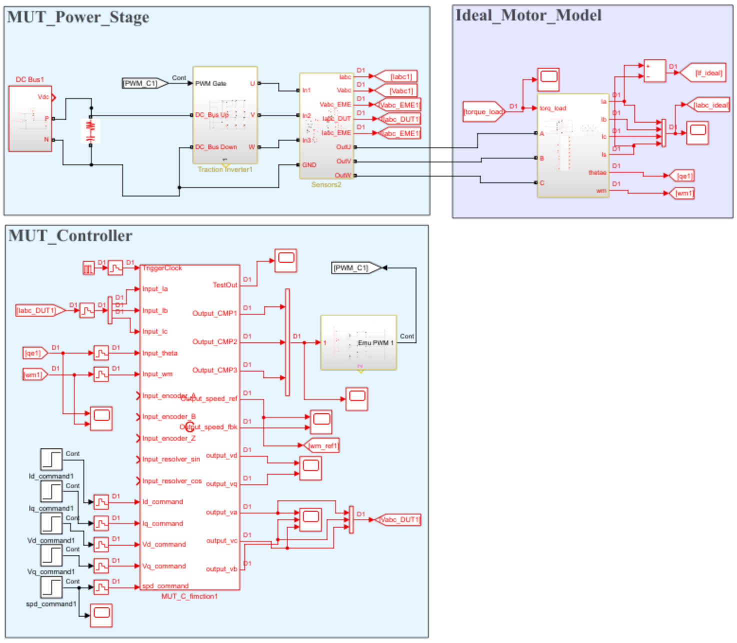

Fig. 4.2 Simulation diagram of motor test-bench with ideal motor model.

Besides, the load profile for the tests in both simulation and experiment is shown in Fig. 4.3. The speed reference is chosen to be 1500 rpm since the rated speed for the emulated motor is 2000 rpm. Note that 1500 rpm is 100 Hz in electrical frequency with 8-pole PMSM. Thus, the frequency of second order harmonic is referred to 200 Hz in this thesis.

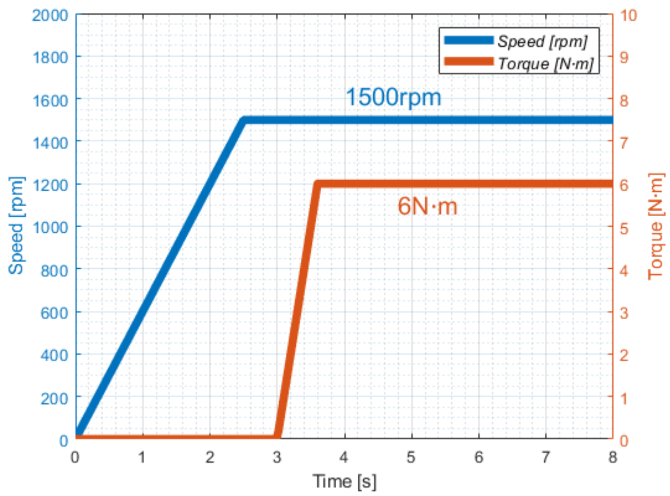

doi:10.6342/NTU202302551

Fig. 4.3 The load profile of the motor test-bench.

4.2 Simulation under R-Unbalance Scenario

In this section, the motor model under R-Unbalance, which is derived in Section 2.2.2 , is utilized and the performance of the traditional decoupling PI control and the proposed CPIR control are presented in Section 4.2.1 and Section 4.2.2 ,respectively. Note that the unbalanced three-phase resistance are set as shown in (4.1) and the other parameters are identical to the specification shown in

Table 4.2.

$$\begin{cases} R_a = 10.2648\Omega \\ R_b = 0.2648\Omega \\ R_c = 0.2648\Omega \end{cases} \tag{4.1}$$

4.2.1 R-Unbalance Simulation with PI Control

Fig. 4.4 shows the three-phase currents in the time domain and the αβ-axis currents in stationary frame under R-Unbalance simulation with PI control for the comparison, where $i_{a.ideal}$, $i_{b.ideal}$, $i_{c.ideal}$, $i_{a.model}$, $i_{b.model}$, $i_{c.model}$, $i_{a.PHIL}$, $i_{b.PHIL}$, and $i_{c.PHIL}$ are the three-phase currents calculated by the pure numerical model, referred to as ideal currents, the three-phase currents calculated by the motor model in the PHIL, referred to as model currents, and the three-phase currents flowing through the PHIL power stage, referred to as PHIL currents, respectively.

From Fig. 4.4(a) and Fig. 4.4(b), it can be found that the difference between the ideal currents and the model currents are unclear, mainly on the switching-related harmonics. However, it can be found that the difference between the model currents and the PHIL currents have some amplitude difference from Fig. 4.4(c). Therefore, the ellipses formed by the model currents and the PHIL currents, as shown in Fig. 4.4(d), are not identical.

Fig. 4.5 and Fig. 4.6 show the dq-axis reference currents and feedback currents in

doi:10.6342/NTU202302551

the time domain and the frequency domain under R-Unbalance simulation with PI control for the comparison, where i_d^*, i_q^*, i_d, and i_q are the dq-axis reference currents and feedback currents, respectively.

From Fig. 4.5(a), Fig. 4.5(b), Fig. 4.6(a), and Fig. 4.6(b), it is evident that there is a noticeable error between the dq-axis reference currents and feedback currents in the time domain. Additionally, Fig. 4.5(c), Fig. 4.5(d), Fig. 4.6(c), and Fig. 4.6(d) show the main difference in dq-axis is attributed to the steady-state error in the second harmonic, which is the target of suppression through the implementation of the proposed CPIR control.

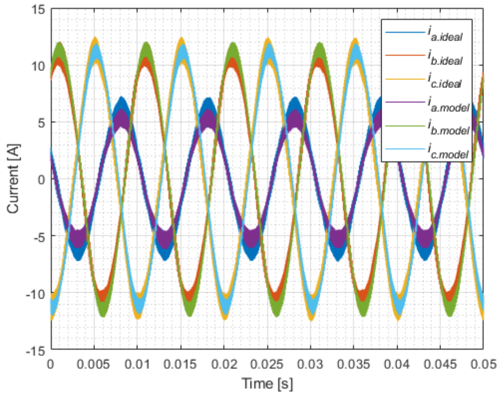

(a)

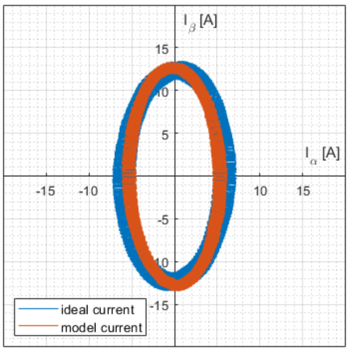

(b)

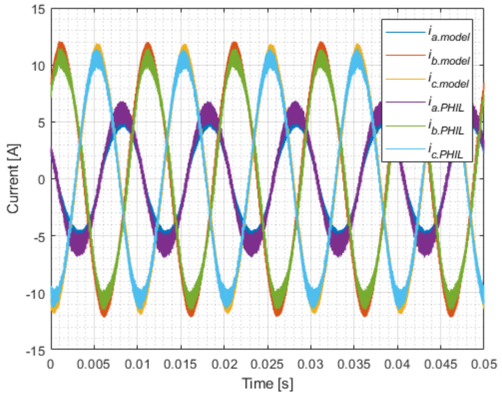

(c)

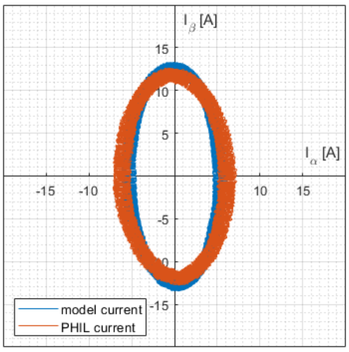

(d)

Fig. 4.4 The comparison diagram for three-phase currents in the time domain and αβ-axis currents in stationary frame under R-Unbalance simulation with PI control (a) The three-phase current comparison between ideal currents and model currents (b) The αβ-axis current comparison between ideal currents and model currents (c) The three-

doi:10.6342/NTU202302551

phase current comparison between model currents and PHIL currents (d) The αβ-axis current comparison between model currents and PHIL currents.

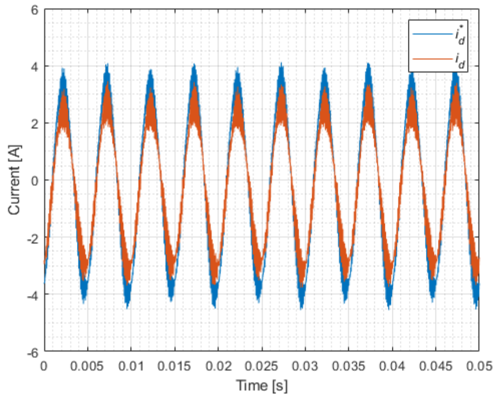

(a)

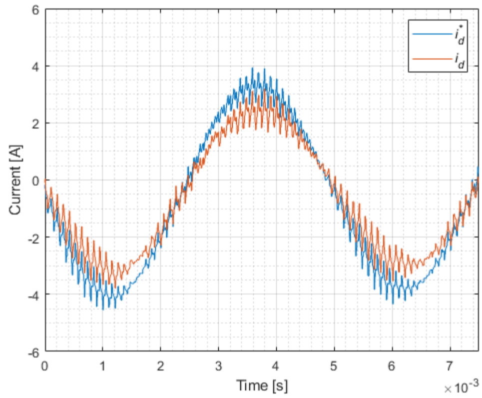

(b)

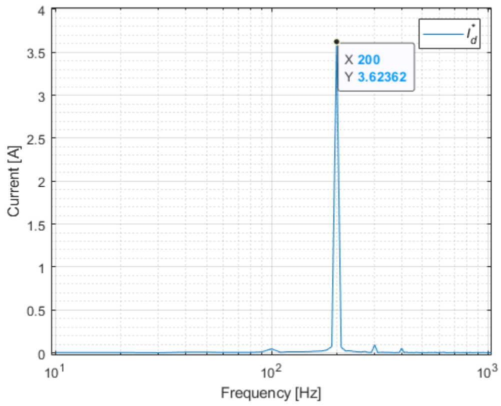

(c)

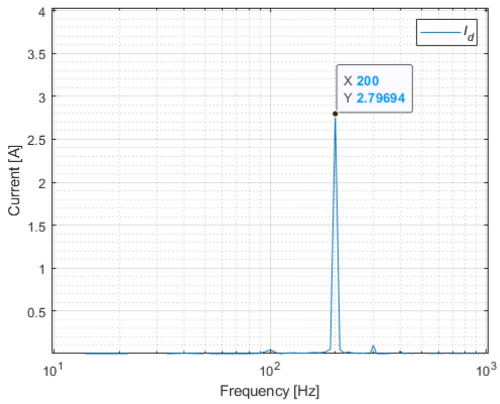

(d)

Fig. 4.5 The comparison diagram for the d-axis reference current and feedback current in the time domain and the frequency domain under R-Unbalance simulation with PI control (a) The d-axis current comparison between the reference current and the feedback current in the time domain (b) The zoom-in version of d-axis current comparison in the time domain (c) The d-axis reference current in the frequency domain (d) The d-axis feedback current in the frequency domain.

doi:10.6342/NTU202302551

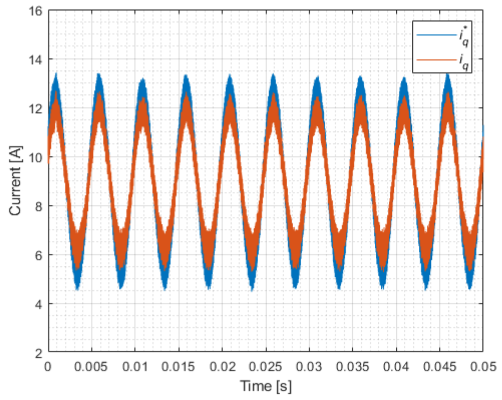

(a)

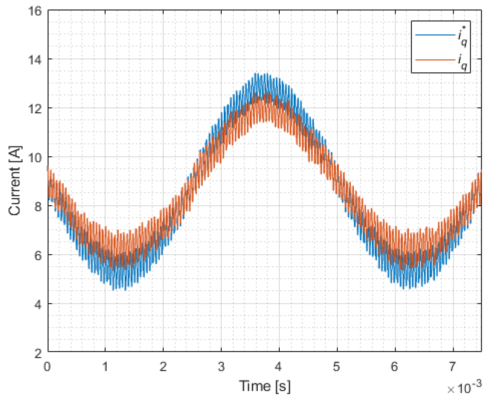

(b)

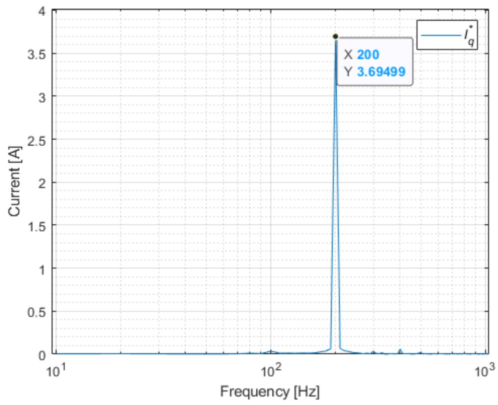

(c)

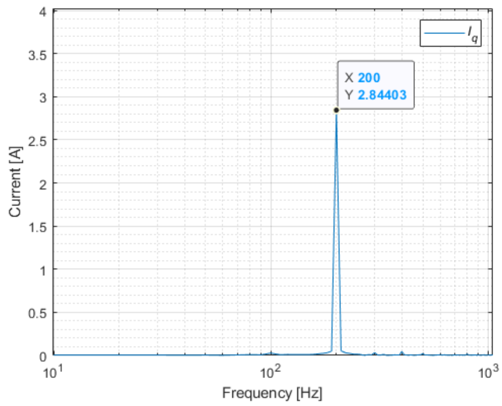

(d)

Fig. 4.6 The comparison diagram for the q-axis reference current and feedback current in the time domain and the frequency domain under R-Unbalance simulation with PI control (a) The q-axis current comparison between the reference current and the feedback current in the time domain (b) The zoom-in version of q-axis current comparison in the time domain (c) The q axis reference current in the frequency domain (d) The q-axis feedback current in the frequency domain.

doi:10.6342/NTU202302551

4.2.2 R-Unbalance Simulation with CPIR Control

Fig. 4.7 shows the three-phase currents in the time domain and the $\alpha\beta$-axis currents in stationary frame under R-Unbalance simulation with CPIR control for the comparison.

From Fig. 4.7(a) and Fig. 4.7(b), it can be found that the difference between the ideal currents and the model currents are similar to the ones with PI control. However, it can be found that the model currents and the PHIL currents are almost the same from Fig. 4.7(c). Consequently, the ellipses formed by the model currents and the PHIL currents, as shown in Fig. 4.7(d), are nearly identical.

Fig. 4.8 and Fig. 4.9 show the dq-axis reference currents and feedback currents in the time domain and the frequency domain under R-Unbalance simulation with CPIR control for the comparison.

Based on the observations from Fig. 4.8(a), Fig. 4.8(b), Fig. 4.9(a), and Fig. 4.9(b), it is obvious to note that the noticeable error between the reference currents and the feedback currents resulted from the usage of PI control is eliminated. Furthermore, the results depicted in Fig. 4.8(c), Fig. 4.8(d), Fig. 4.9(c), and Fig. 4.9(d) demonstrate that the proposed CPIR control achieves a second harmonic steady-state error of less than 1%, effectively suppressing its presence.

doi:10.6342/NTU202302551

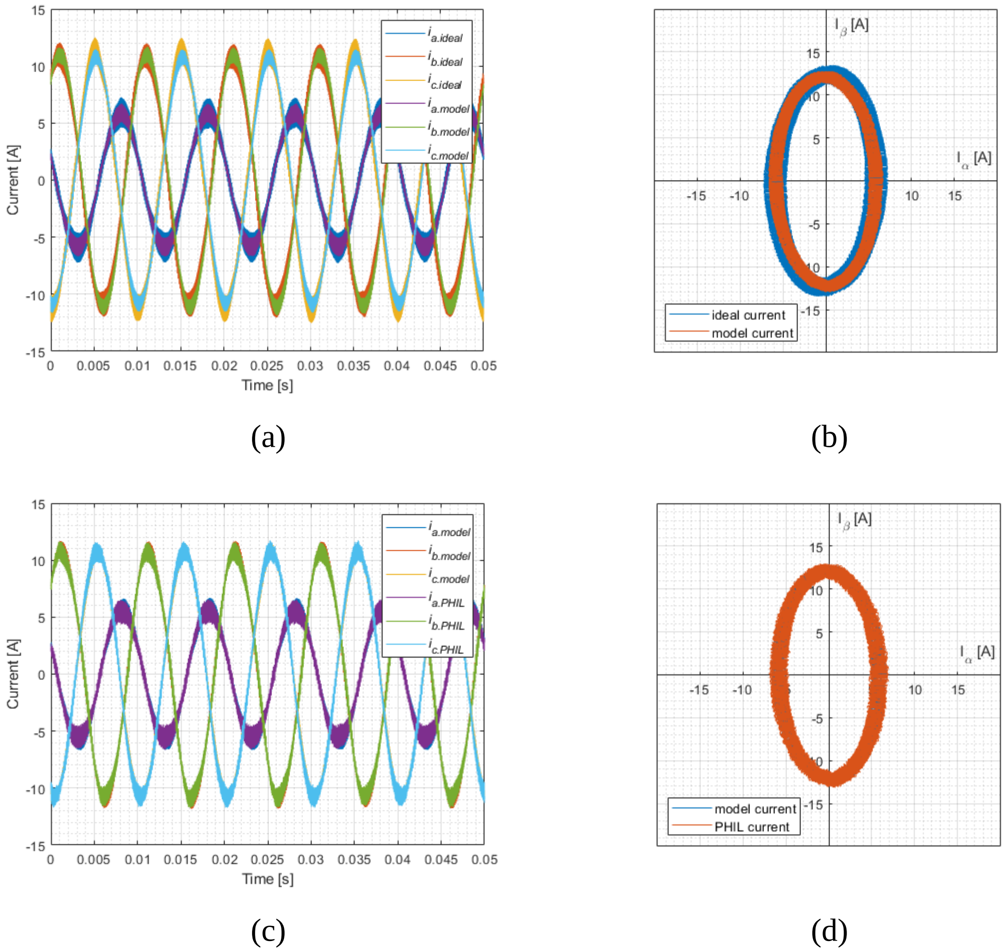

Fig. 4.7 The comparison diagram for three-phase currents in the time domain and αβ-axis currents in stationary frame under R-Unbalance simulation with CPIR control (a) The three-phase current comparison between ideal currents and model currents (b) The αβ-axis current comparison between ideal currents and model currents (c) The three-phase current comparison between model currents and PHIL currents (d) The αβ-axis current comparison between model currents and PHIL currents.

doi:10.6342/NTU202302551

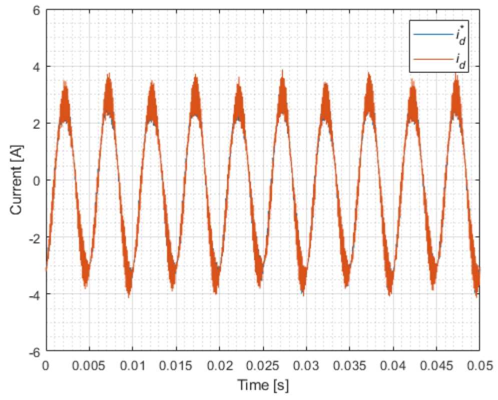

(a)

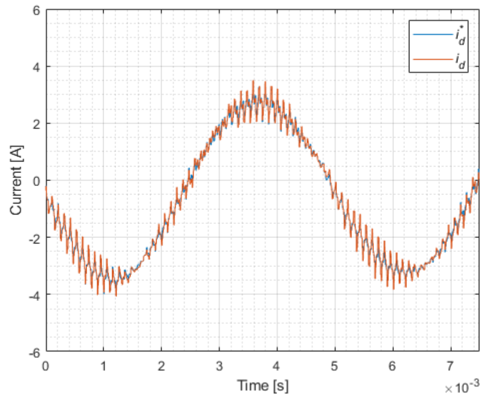

(b)

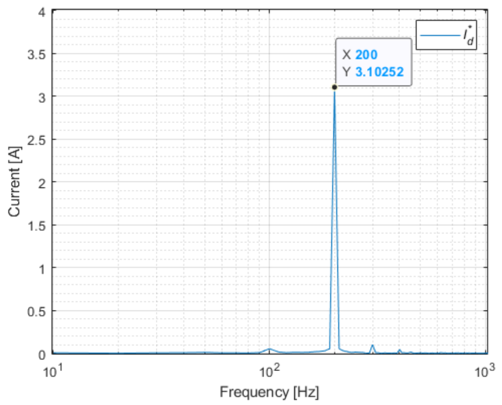

(c)

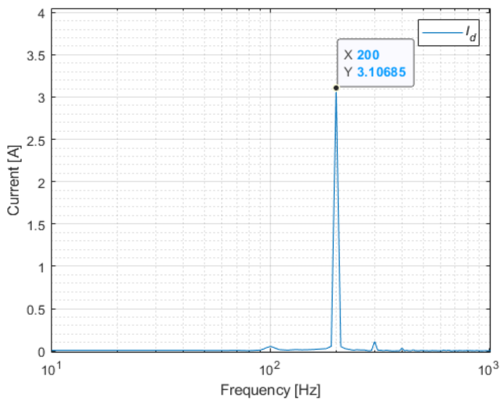

(d)

Fig. 4.8 The comparison diagram for the d-axis reference current and feedback current in the time domain and the frequency domain under R-Unbalance simulation with CPIR control (a) The d-axis current comparison between the reference current and the feedback current in the time domain (b) The zoom-in version of d-axis current comparison in the time domain (c) The d-axis reference current in the frequency domain (d) The d-axis feedback current in the frequency domain.

doi:10.6342/NTU202302551

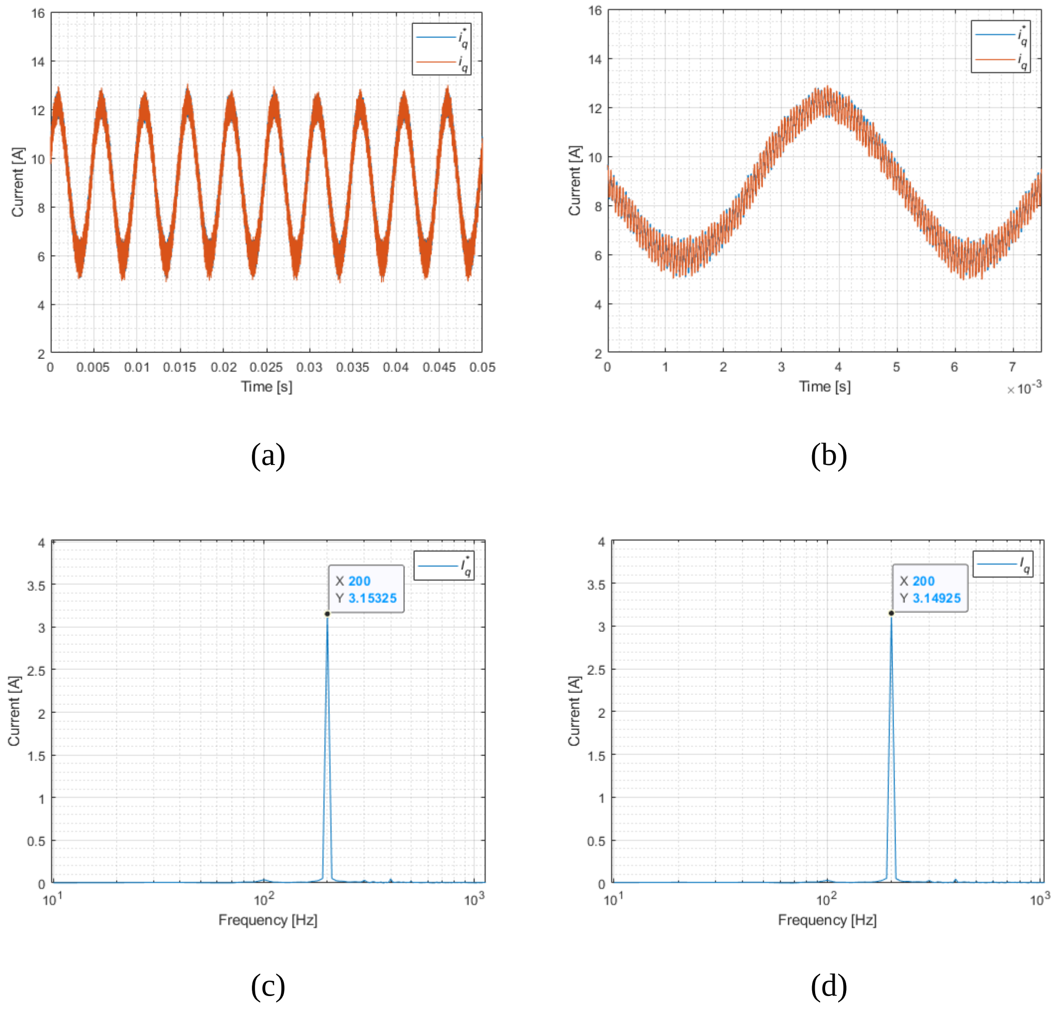

Fig. 4.9 The comparison diagram for the q-axis reference current and feedback current in the time domain and the frequency domain under R-Unbalance simulation with CPIR control (a) The q-axis current comparison between the reference current and the feedback current in the time domain (b) The zoom-in version of q-axis current comparison in the time domain (c) The q-axis reference current in the frequency domain (d) The q-axis feedback current in the frequency domain.

doi:10.6342/NTU202302551

4.3 Simulation under OPF Scenario

In this section, the motor model under OPF, which is derived in Section 2.3.2 , is utilized and the performance of the traditional decoupling PI control and the proposed CPIR control are presented in Section 4.3.1 and Section 4.3.2 ,respectively. Note that all the motor parameters remain identical to the specification provided in

Table 4.2. However, it is worth mentioning that phase A is intentionally disconnected, resulting in the desired open circuit condition targeted by this scenario.

4.3.1 OPF Simulation with PI Control

Fig. 4.10 shows the three-phase currents in the time domain and $\alpha\beta$-axis currents in stationary frame under OPF simulation with PI control for the comparison.

From Fig. 4.10(a) and Fig. 4.10(b), it can be observed that the ideal currents and the model currents are almost identical. Furthermore, it is noteworthy that the $\alpha\beta$-axis currents in stationary frame appear as a straight line due to the absence of A-phase current caused by the open circuit condition. However, Fig. 4.10(c) shows that there is a significant disparity between the model currents and the PHIL currents. Thus, the graph formed by the PHIL currents in Fig. 4.10(d) does not exhibit a straight line shape.

Fig. 4.11 and Fig. 4.12 show the dq-axis reference currents and feedback currents in the time domain and the frequency domain under OPF simulation with PI control for the comparison.

From Fig. 4.11(a), Fig. 4.11(b), Fig. 4.12(a), and Fig. 4.12(b), it is obvious that there is a considerable error between the dq-axis reference currents and feedback currents in the time domain. In addition, Fig. 4.11(c), Fig. 4.11(d), Fig. 4.12(c), and Fig. 4.12(d) show the difference in dq-axis is due to the steady-state error in the second harmonic.

doi:10.6342/NTU202302551

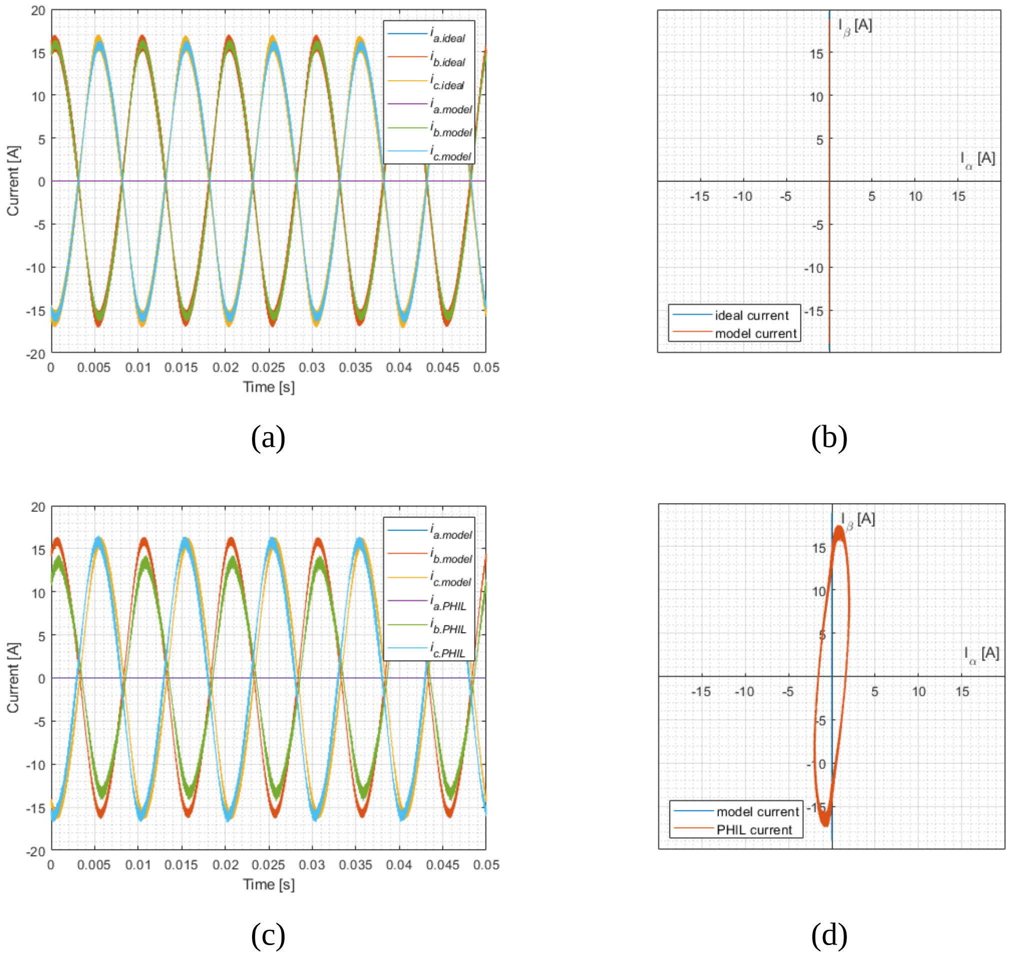

Fig. 4.10 The comparison diagram for three-phase currents in the time domain and αβ-axis currents in stationary frame under OPF simulation with PI control (a) The three-phase current comparison between ideal currents and model currents (b) The αβ-axis current comparison between ideal currents and model currents (c) The three-phase current comparison between model currents and PHIL currents (d) The αβ-axis current comparison between model currents and PHIL currents.

doi:10.6342/NTU202302551

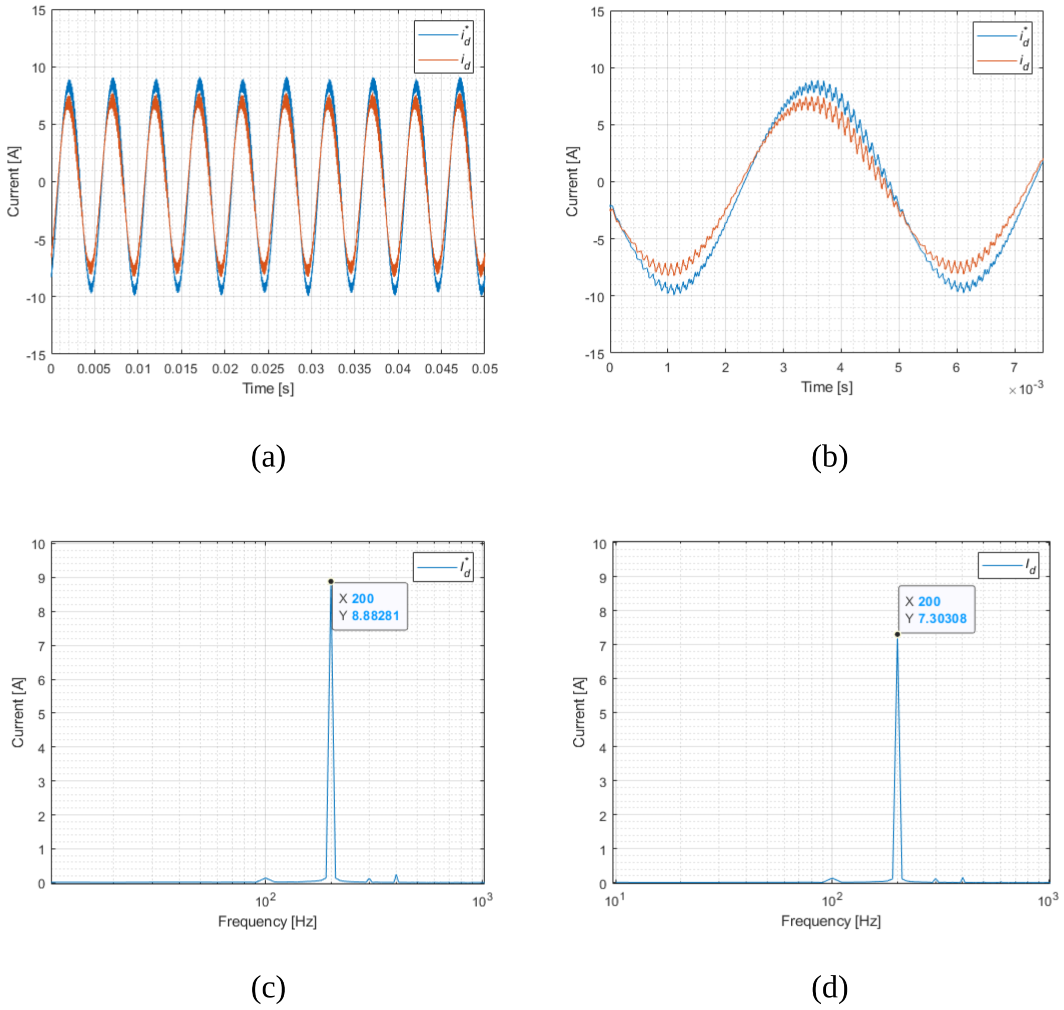

Fig. 4.11 The comparison diagram for the d-axis reference current and feedback current in the time domain and the frequency domain under OPF simulation with PI control (a) The d-axis current comparison between the reference current and the feedback current in the time domain (b) The zoom-in version of d-axis current comparison in the time domain (c) The d-axis reference current in the frequency domain (d) The d-axis feedback current in the frequency domain.

doi:10.6342/NTU202302551

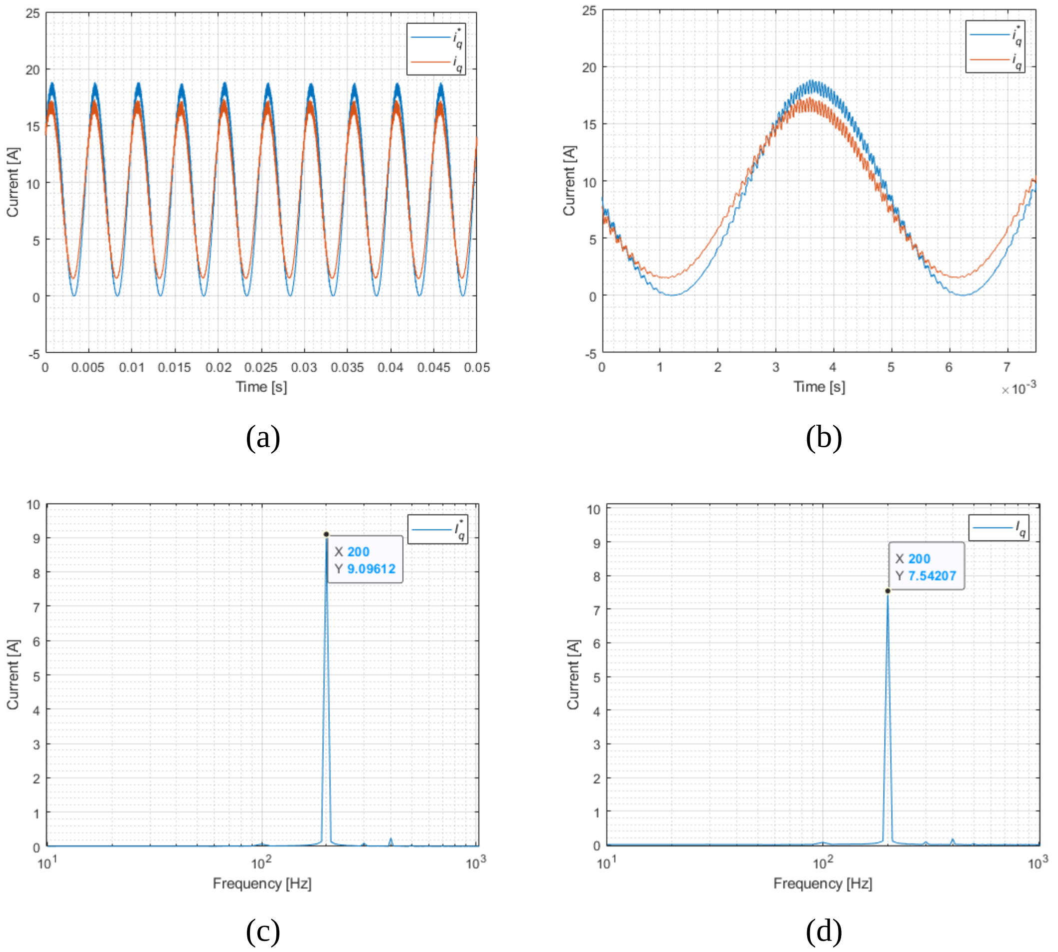

Fig. 4.12 The comparison diagram for the q-axis reference current and feedback current in the time domain and the frequency domain under OPF simulation with PI control (a) The q-axis current comparison between the reference current and the feedback current in the time domain (b) The zoom-in version of q-axis current comparison in the time domain (c) The q-axis reference current in the frequency domain (d) The q-axis feedback current in the frequency domain.

doi:10.6342/NTU202302551

4.3.2 OPF Simulation with CPIR Control

Fig. 4.13 shows the three-phase currents in the time domain and the $\alpha\beta$-axis currents in stationary frame under OPF simulation with CPIR control for the comparison.

From Fig. 4.13(a) and Fig. 4.13(b), it can be observed that the difference between the ideal currents and the model currents remains consistent with that of the PI control. However, Fig. 4.13(c) illustrates that there is a negligible difference between the model currents and the PHIL currents when using the CPIR control. As a result, the graph illustrating the PHIL currents in Fig. 4.13(d) closely resembles a straight line, indicating improved performance and accuracy.

Fig. 4.14 and Fig. 4.15 show the dq-axis reference currents and feedback currents in the time domain and the frequency domain under OPF simulation with CPIR control for the comparison.

Based on the observations from Fig. 4.14(a), Fig. 4.14(b), Fig. 4.15(a), and Fig. 4.15(b), it is evident that the CPIR control successfully reduces the significant error between the reference currents and the feedback currents, which is present when using the PI controller. Moreover, as shown in Fig. 4.14(c), Fig. 4.14(d), Fig. 4.15(c), and Fig. 4.15(d), the CPIR control achieves an impressive suppression of the second harmonic with a steady-state error of approximately 2%.

doi:10.6342/NTU202302551

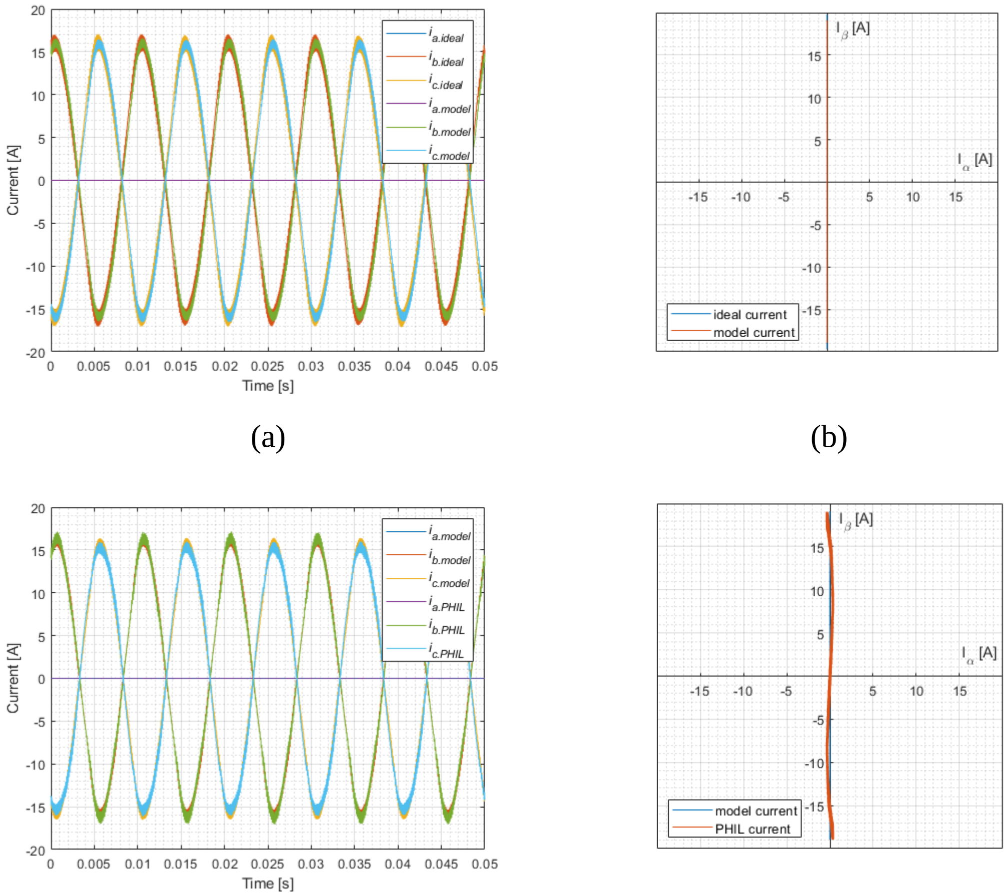

(a) (b)

(c) (d)

Fig. 4.13 The comparison diagram for three-phase currents in the time domain and αβ-axis currents in stationary frame under OPF simulation with CPIR control (a) The three-phase current comparison between ideal currents and model currents (b) The αβ-axis current comparison between ideal currents and model currents (c) The three-phase current comparison between model currents and PHIL currents (d) The αβ-axis current comparison between model currents and PHIL currents.

doi:10.6342/NTU202302551

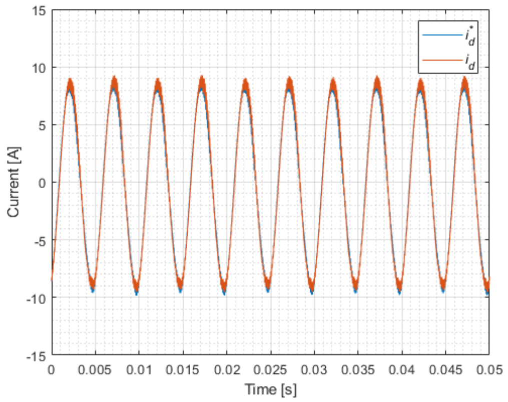

(a)

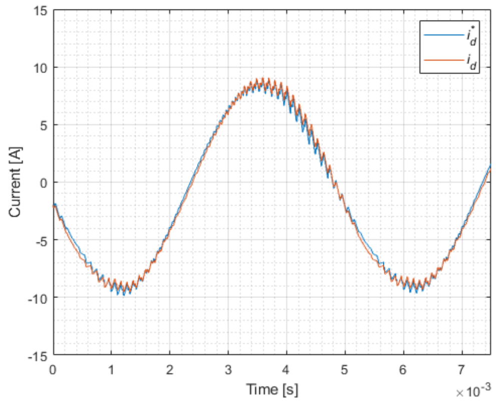

(b)

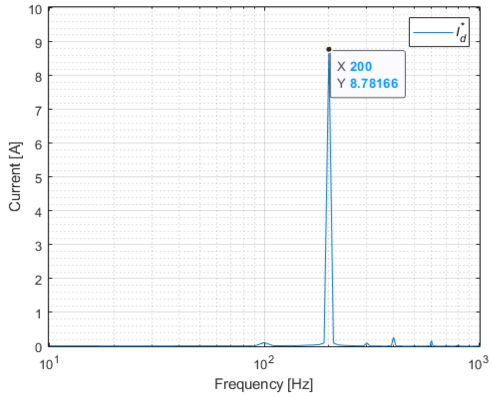

(c)

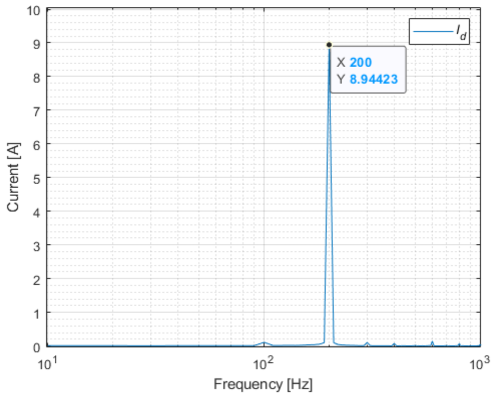

(d)

Fig. 4.14 The comparison diagram for the d-axis reference current and feedback current in the time domain and the frequency domain under OPF simulation with CPIR control (a) The d-axis current comparison between the reference current and the feedback current in the time domain (b) The zoom-in version of d-axis current comparison in the time domain (c) The d-axis reference current in the frequency domain (d) The d-axis feedback current in the frequency domain.

doi:10.6342/NTU202302551

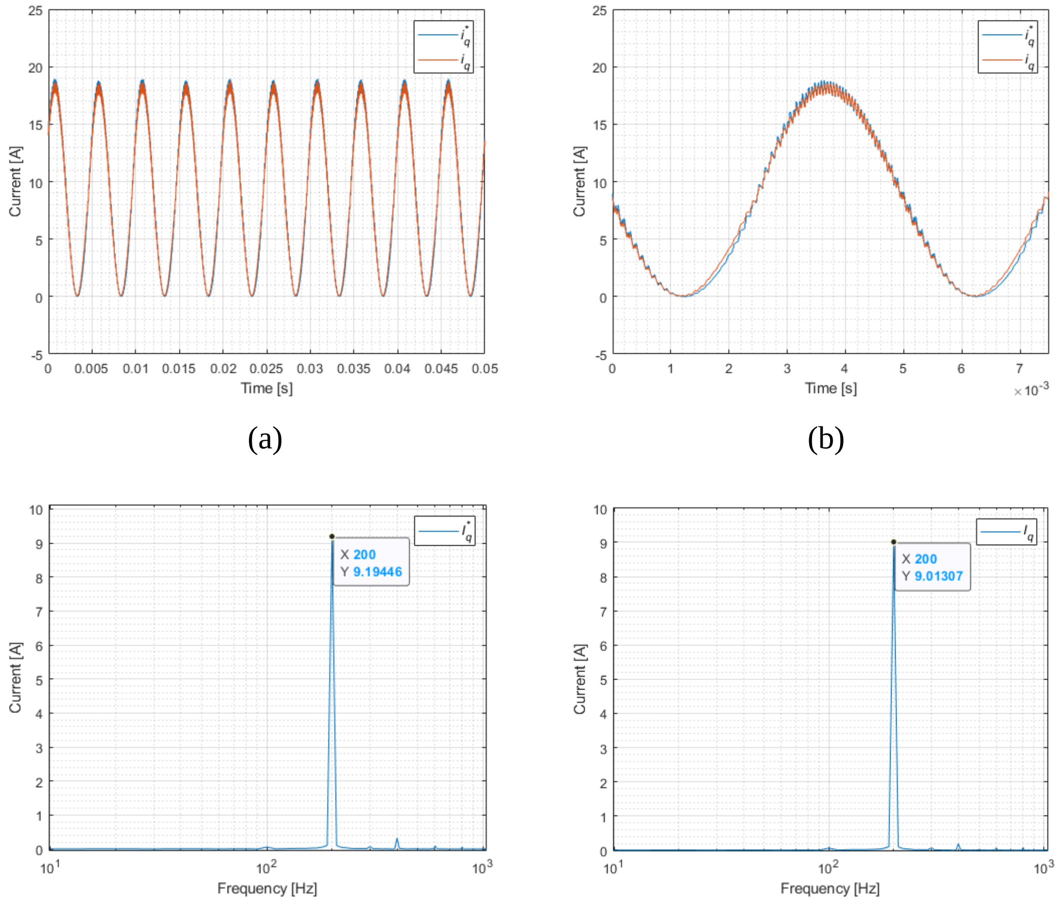

(a) (b)

(c) (d)

Fig. 4.15 The comparison diagram for the q-axis reference current and feedback current in the time domain and the frequency domain under OPF simulation with CPIR control (a) The q-axis current comparison between the reference current and the feedback current in the time domain (b) The zoom-in version of q-axis current comparison in the time domain (c) The q-axis reference current in the frequency domain (d) The q-axis feedback current in the frequency domain.

doi:10.6342/NTU202302551

4.4 Simulation under ISCF Scenario

In this section, the motor model under ISCF, which is derived in Section 2.4.2 , is utilized and the performance of the traditional decoupling PI control and the proposed CPIR control are presented in Section 4.4.1 and Section 4.4.2 ,respectively. Note that the fault resistance and the fault index are set as shown in (4.2) and the other parameters are identical to the specification shown in

Table 4.2.

$$\begin{cases} R_f = 0.1\Omega \\ \Delta = 0.2 \end{cases} \tag{4.2}$$

4.4.1 ISCF Simulation with PI Control

Fig. 4.16 shows the three-phase currents in the time domain and αβ-axis currents in stationary frame under ISCF simulation with PI control for the comparison.

From Fig. 4.16(a) and Fig. 4.16(b), it can be found that the ideal currents and the model currents exhibit a noticeable difference, especially for the switching-related harmonics. This is because the ideal currents are calculated at a frequency that is 10 times higher than the model currents obtained from the PHIL motor model. As a result, the ideal currents offer improved accuracy for capturing nonlinear effects, particularly the switching effect in this application.

Fig. 4.16(c) shows that there is a significant disparity between the model currents and the PHIL currents. This can be attributed to the fact that the frequencies of the switching-related harmonics present in model currents exceed the bandwidth of the designed control. In other words, the control is only capable of regulating currents for relatively low frequencies, as evident from Fig. 4.16(d).

Fig. 4.17 and Fig. 4.18 show the dq-axis reference currents and feedback currents in

doi:10.6342/NTU202302551

the time domain and the frequency domain under ISCF simulation with PI control for the comparison.

From Fig. 4.17(a), Fig. 4.17(b), Fig. 4.18(a), and Fig. 4.18(b), it is apparent that there is a tremendous error between the dq-axis reference currents and feedback currents in the time domain. Furthermore, Fig. 4.17(c), Fig. 4.17(d), Fig. 4.18(c), and Fig. 4.18(d) indicate the difference in dq-axis is caused not only by the second harmonic but also by the near 9.5kHz and near 19kHz components. These additional components are attributed to the switching frequency of the MUT and twice the switching frequency, respectively.

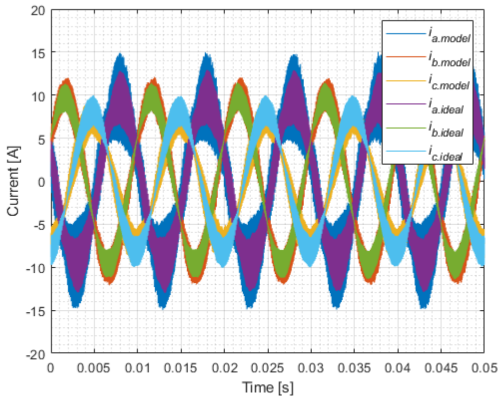

(a)

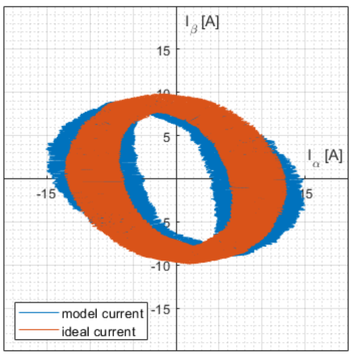

(b)

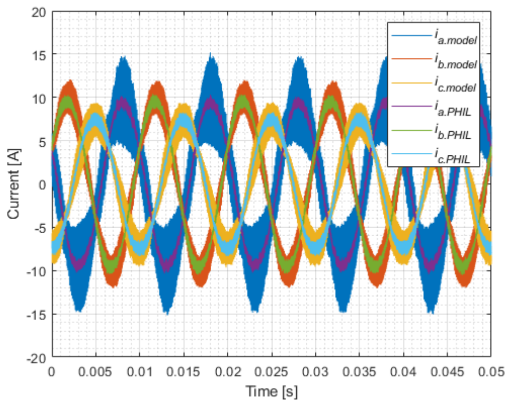

(c)

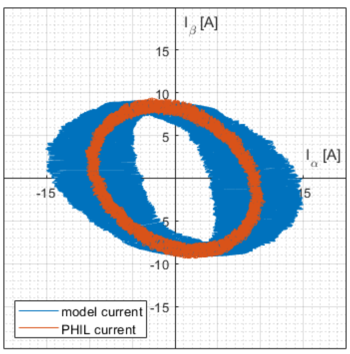

(d)

Fig. 4.16 The comparison diagram for three-phase currents in the time domain and αβ-axis currents in stationary frame under ISCF simulation with PI control (a) The three-phase current comparison between ideal currents and model currents (b) The αβ-axis current comparison between ideal currents and model currents (c) The three-phase current

doi:10.6342/NTU202302551

comparison between model currents and PHIL currents (d) The αβ-axis current comparison between model currents and PHIL currents.

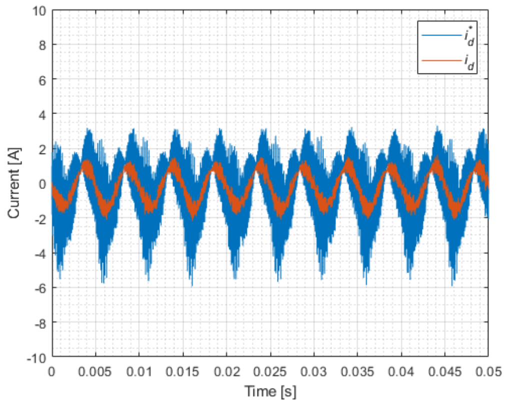

(a)

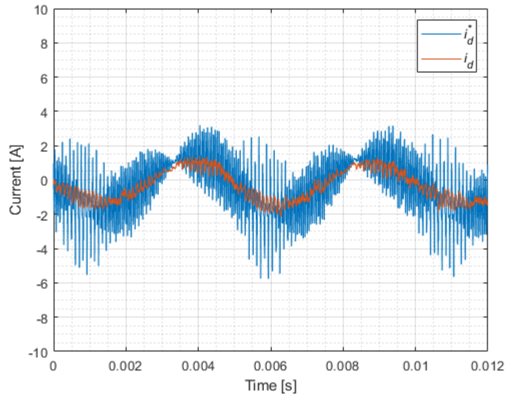

(b)

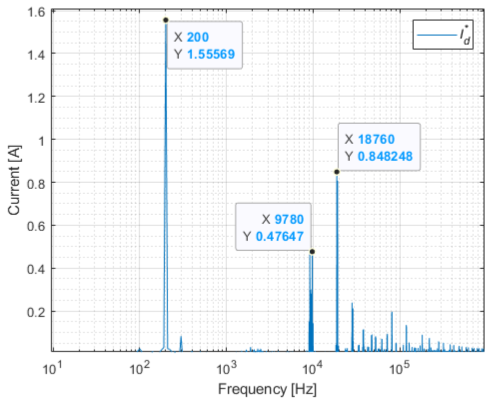

(c)

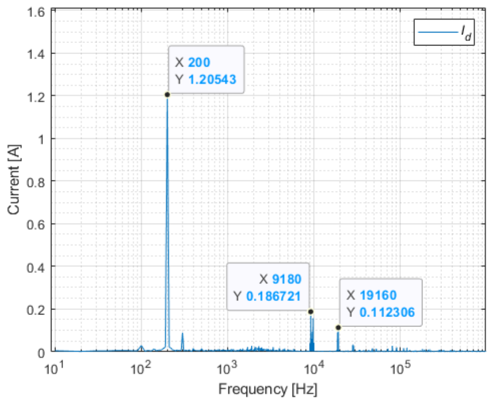

(d)

Fig. 4.17 The comparison diagram for the d-axis reference current and feedback current in the time domain and the frequency domain under ISCF simulation with PI control (a) The d-axis current comparison between the reference current and the feedback current in the time domain (b) The zoom-in version of d-axis current comparison in the time domain (c) The d-axis reference current in the frequency domain (d) The d-axis feedback current in the frequency domain.

doi:10.6342/NTU202302551

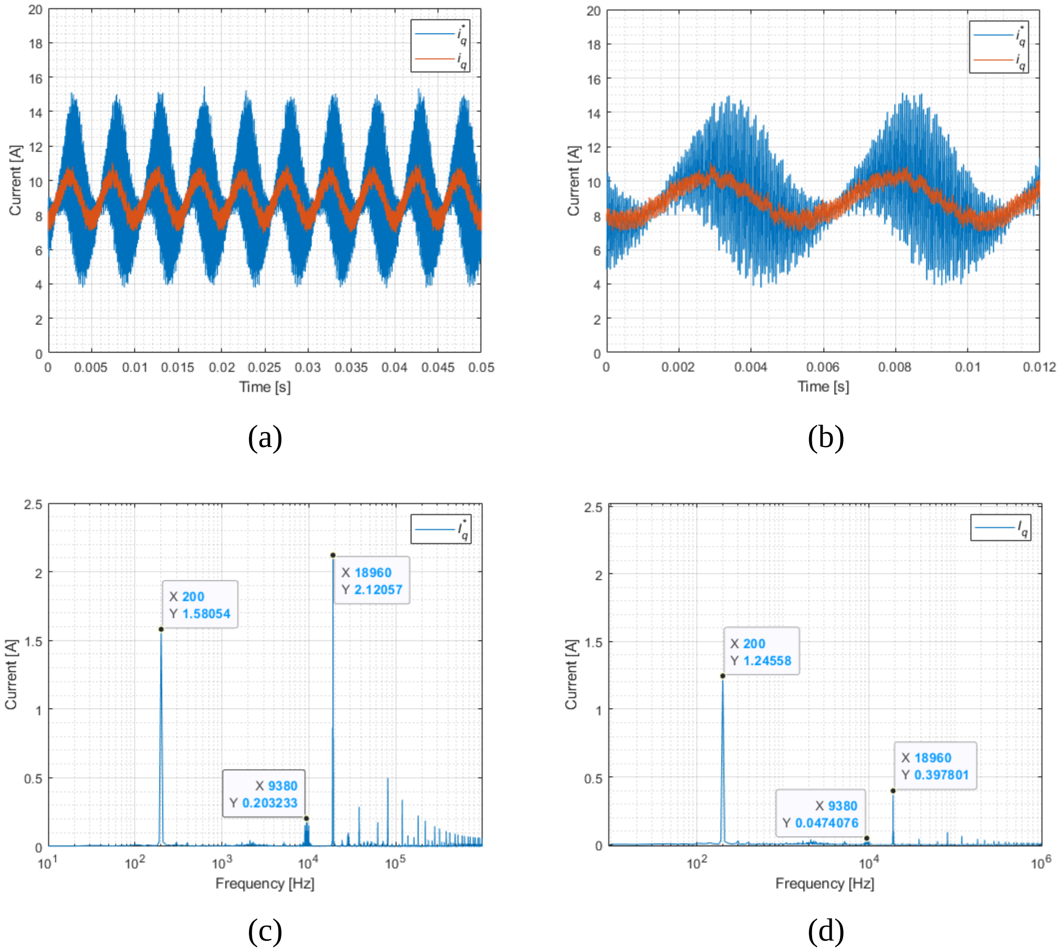

Fig. 4.18 The comparison diagram for the q-axis reference current and feedback current in the time domain and the frequency domain under ISCF simulation with PI control (a) The q-axis current comparison between the reference current and the feedback current in the time domain (b) The zoom-in version of q-axis current comparison in the time domain (c) The q-axis reference current in the frequency domain (d) The q-axis feedback current in the frequency domain.

doi:10.6342/NTU202302551

4.4.2 ISCF Simulation with CPIR Control

Fig. 4.19 shows the three-phase currents in the time domain and $\alpha\beta$-axis currents in stationary frame under ISCF simulation with CPIR control for the comparison.

From Fig. 4.19(a) and Fig. 4.19(b), it can be observed that the difference between the ideal currents and the model currents remains consistent with that of the PI control. Moreover, Fig. 4.19(c) and Fig. 4.19(d) also illustrate that there is no noticeable difference between the model currents and the PHIL currents whether using the CPIR control or PI control.

Fig. 4.20 and Fig. 4.21 show the dq-axis reference currents and feedback currents in the time domain and the frequency domain under ISCF simulation with CPIR control for the comparison.

Based on the observations from Fig. 4.20(a), Fig. 4.20(b), Fig. 4.21(a), and Fig. 4.21(b), it is difficult to discern any noticeable difference between the outcomes obtained with the CPIR control and the results obtained with the PI control. However, as depicted in Fig. 4.20(c), Fig. 4.20(d), Fig. 4.21(c), and Fig. 4.21(d), the CPIR control effectively suppresses the steady-state error in the second harmonic as expected. Nonetheless, it is worth noting that the errors arising from the near 9.5kHz, which is the switching frequency of the MUT, and near 19kHz, whitch is twice the switching frequency of the MUT, components remain unsolved.

doi:10.6342/NTU202302551

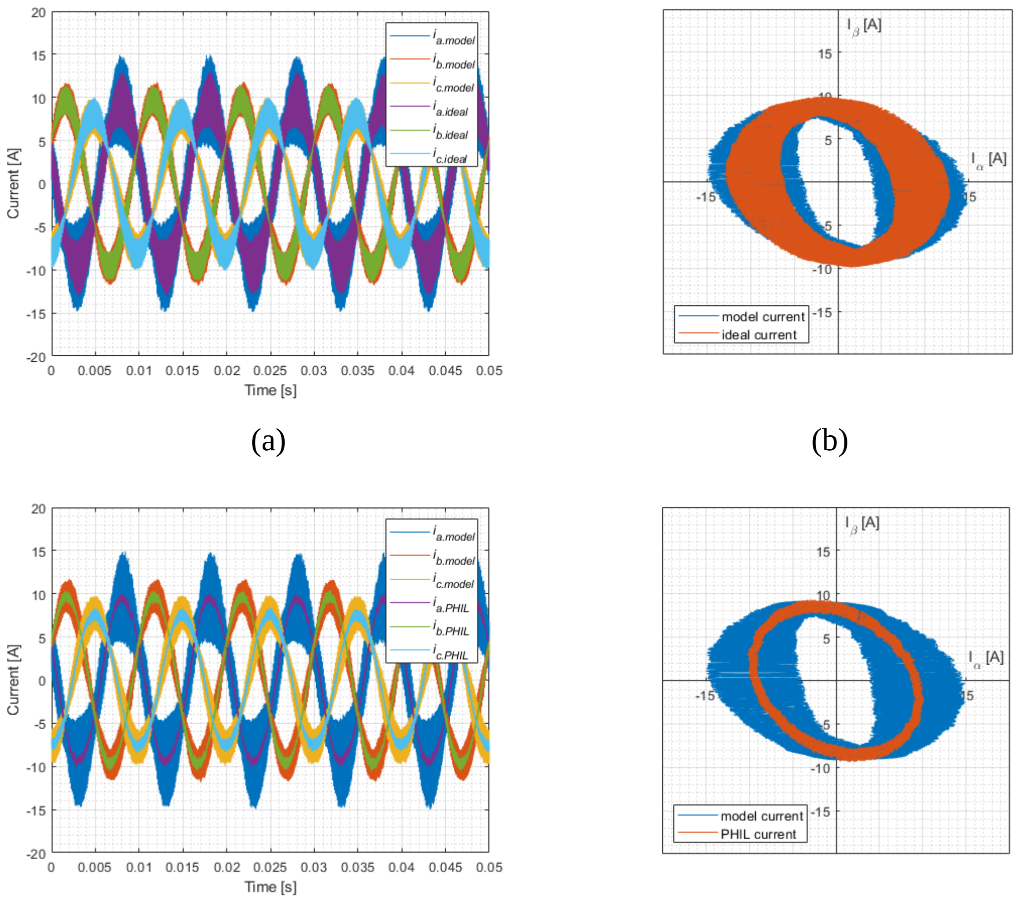

(a) (b)

(c) (d)

Fig. 4.19 The comparison diagram for three-phase currents in the time domain and αβ-axis currents in stationary frame under ISCF simulation with CPIR control (a) The three-phase current comparison between ideal currents and model currents (b) The αβ-axis current comparison between ideal currents and model currents (c) The three-phase current comparison between model currents and PHIL currents (d) The αβ-axis current comparison between model currents and PHIL currents.

doi:10.6342/NTU202302551

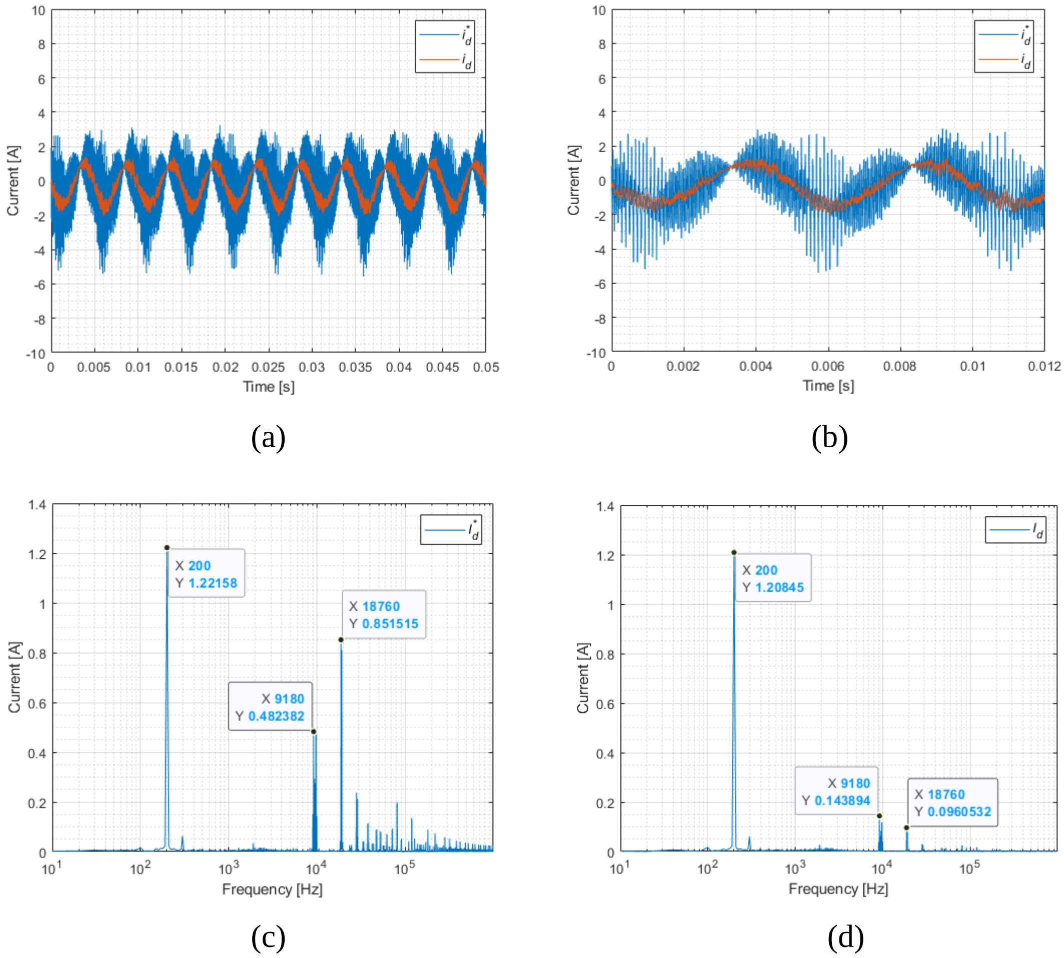

Fig. 4.20 The comparison diagram for the d-axis reference current and feedback current in the time domain and the frequency domain under ISCF simulation with CPIR control (a) The d-axis current comparison between the reference current and the feedback current in the time domain (b) The zoom-in version of d-axis current comparison in the time domain (c) The d-axis reference current in the frequency domain (d) The d-axis feedback current in the frequency domain.

doi:10.6342/NTU202302551

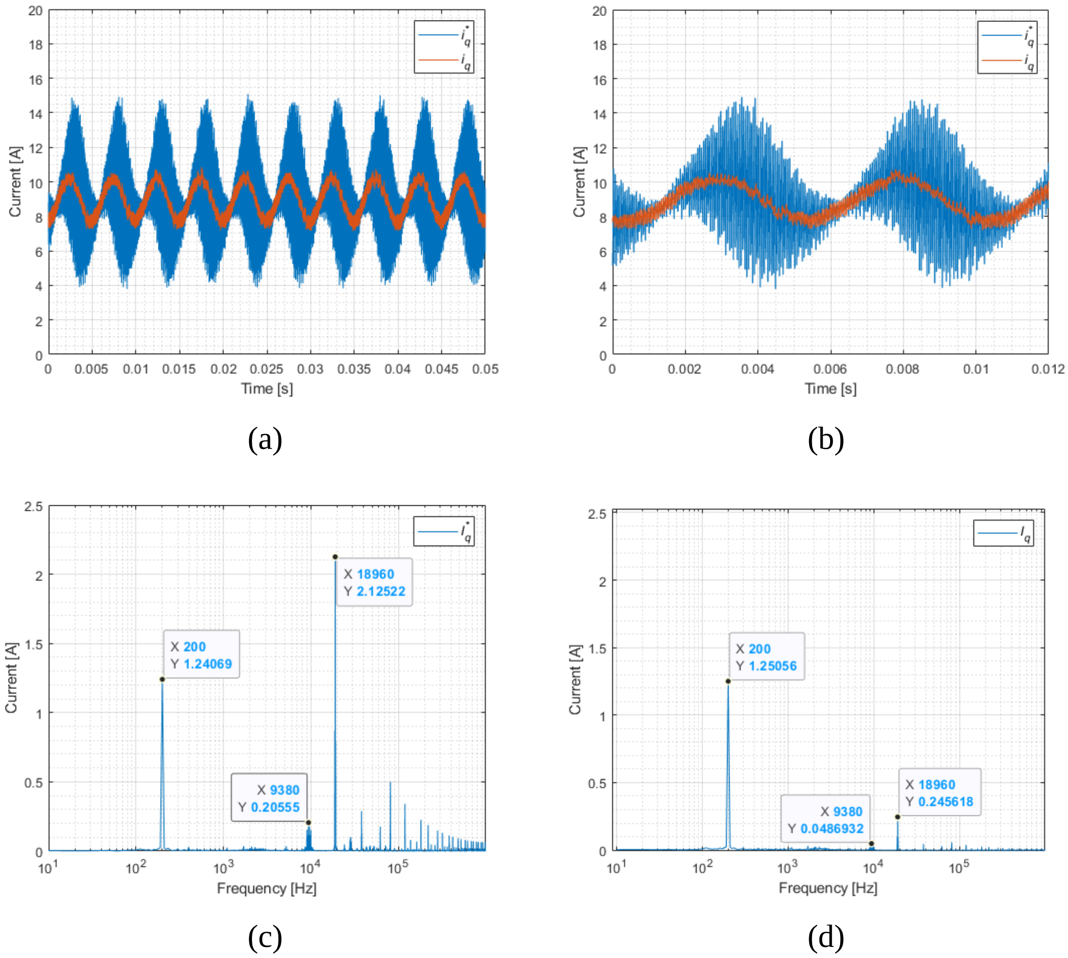

Fig. 4.21 The comparison diagram for the q-axis reference current and feedback current in the time domain and the frequency domain under ISCF simulation with CPIR control (a) The q-axis current comparison between the reference current and the feedback current in the time domain (b) The zoom-in version of q-axis current comparison in the time domain (c) The q-axis reference current in the frequency domain (d) The q-axis feedback current in the frequency domain.

doi:10.6342/NTU202302551

Chapter 5 Experiment Verifications

In the previous chapter, the simulation results are presented to demonstrate that the PHIL-based test-bench can emulate the motor under different fault scenarios. Moreover, it is evident that the proposed CPIR control can enhance the performance of motor emulation compared to the traditional PI control. Therefore, in Chapter 5, the goal is to implement the PHIL-based test-bench in real world, referred to Section 5.1 , and perform the experiments under different fault scenarios with the same specifications and load profile shown in Table 4.1,

Table 4.2 and Fig. 4.3, referred to Section 5.2, 5.3, and 5.4, to verify that the results from experiments are similar to the corresponding simulation results. Additionally, a comprehensive comparison of the improvements achieved by implementing the CPIR control across each discussed fault scenario is provided in the end of Section 5.5.

5.1 Test-bench Implementation

5.1.1 Hardware Development

Fig. 5.1 illustrates the schematic diagram of PHIL-based test-bench. It is worth noting that while the primary focus of this thesis is on the development of PHIL, it is essential to build our own motor driver to replicate the experimental setup as closely as possible to the simulation. The prototype of PHIL-based motor test-bench is shown in Fig. 5.2.

It is intuitive that the critical aspects of hardware development lie in the capability of the three-phase inverter and the selection of the MCU to effectively implement the PHIL functions.

For the three-phase inverter, the CAS120M12BM2 SiC Half-Bridge Power Module

doi:10.6342/NTU202302551

from Wolfspeed combined with the ADuM4135 driver IC from Analog Devices are utilized. Note that the power module ensures stress capabilities with a minimum breakdown voltage of 1200V and a maximum output current of $150A_{rms}$ at a switching frequency of 100kHz. These specifications make it well-suited for PHIL applications.

The TMS320F28379D controlCard from Texas Instrument (TI) is adopted as the MCU for both the PHIL and the MUT. Along with the MCU, the interface board is designed to provide some key features, including the anti-aliasing filters for ADC inputs, the differential drivers and receivers for driver ICs and fault signals, the encoder emulator circuit designed for transmitting the angel and speed information to the motor driver, and the power supplies for the peripheral circuits and the MCU.

With the prototype shows in Fig. 5.2, a 30kW emulation using a balanced motor model is achieved, thereby ensuring that this experimental setup can withstand the current stress associated with the emulations for motor under different fault scenarios.

doi:10.6342/NTU202302551

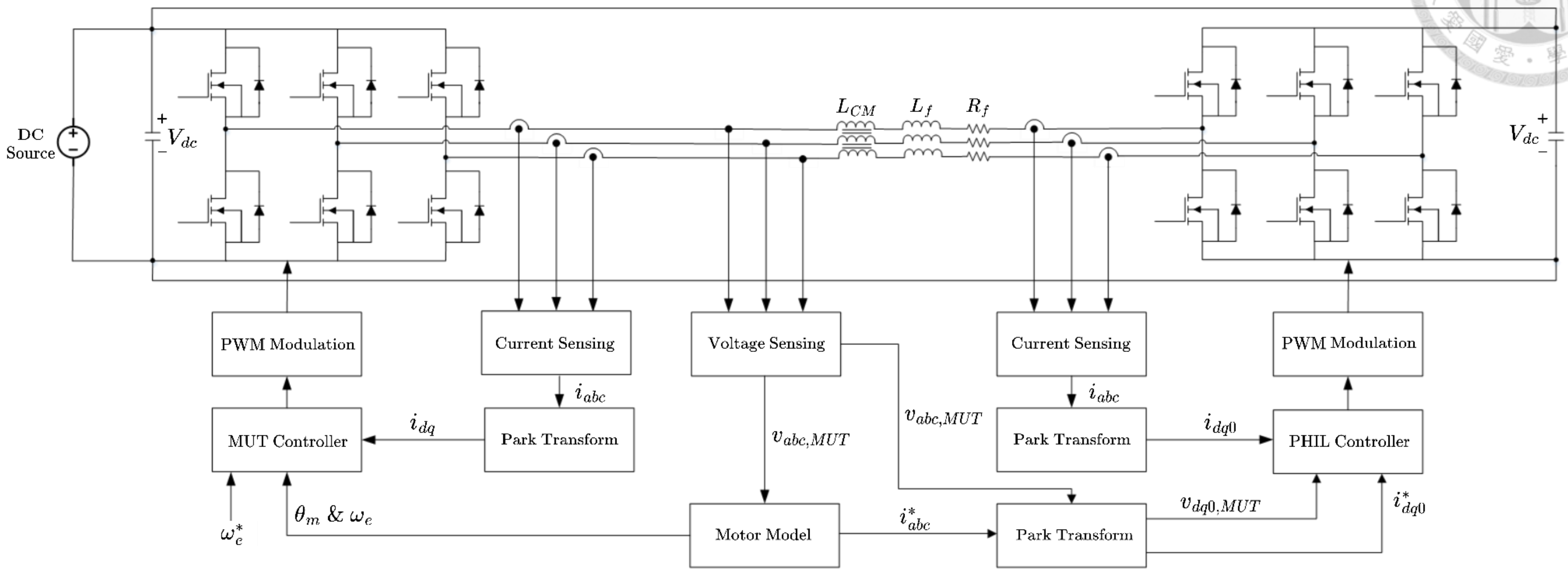

Fig. 5.1 The schematic diagram of PHIL-based motor test-bench.

doi:10.6342/NTU202302551

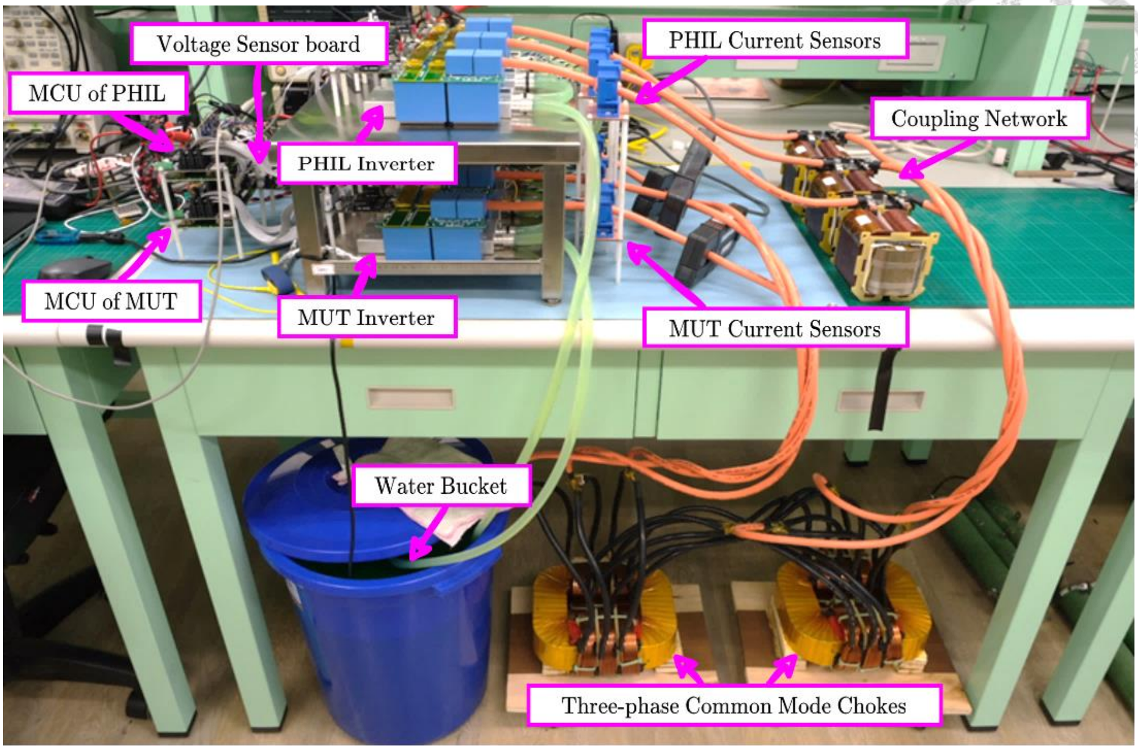

Fig. 5.2 The prototype of PHIL-based motor test-bench.

5.1.2 Firmware Development

The TMS320F28379D controlCard offers several notable features, with the Control Law Accelerator (CLA) and the presence of 4 12-bit ADC modules, each equipped with 6 channels, for synchronized sampling being the most crucial ones. The CLA enables parallel computation alongside the CPU, while the 12-bit ADC modules ensure accurate and synchronized data acquisition. The flowchart of PHIL firmware is shown in Fig. 5.3 and the overall process can be briefly described as follows:

Initially, the sensing signals can be separated into two groups. The switching node voltages used in the motor model calculation, namely v_a, v_b, and v_c, are sampled synchronously with the same frequency utilized for model calculation, specifically 312.5kHz, as the first group; meanwhile, the three-phase currents and the DC bus voltage used in the control programme and SPWM modulation, namely i_a, i_b, i_c, and V_{dc}, are

doi:10.6342/NTU202302551

sampled synchronously at the switching frequency of the PHIL, specifically 100kHz, as the second group.

When the end-of-conversion (EOC) flag of the first group is set, the CLA task is initiated. At the beginning of the CLA task, the 12-bit switching node voltages are converted into real values with the unit of volt. Subsequently, the motor model calculation commences. Once the calculation is completed, the obtained results, representing the future step of the model currents, are updated in the CLA memories as the current step. These updated values will be utilized for model calculation during the subsequent CLA task, thus concluding the current CLA task.

Meanwhile, when the EOC flag of the second group is set, the ADC interrupt is initiated. The ADC interrupt begins by checking whether the PHIL is manually stopped or not; If it is stopped, all the output signals for the switches are pulled low, resulting in a complete shutdown of the inverter. Following this, the 12-bit three-phase currents and DC bus voltage are converted into real values with the unit of ampere and volt, respectively. The converted currents are then examined to determine if they exceed the current limit of the test-bench. If any of the currents surpass the limitation, the overcurrent protection (OCP) flag is set, and all switches are turned off. Subsequently, the CPU accesses the CLA memories to retrieve the switching node voltages and model currents obtained from the CLA. These data are then utilized within the ADC interrupt to execute the control programme. Once the control programme is completed, the resulting control outputs are updated in the memories as the previous step, ready for use in the next control programme. Last but not least, the control outputs are normalized by the sensed DC bus voltage. The normalized control outputs are then employed in SPWM modulation to generate the output signals for the switches.

doi:10.6342/NTU202302551

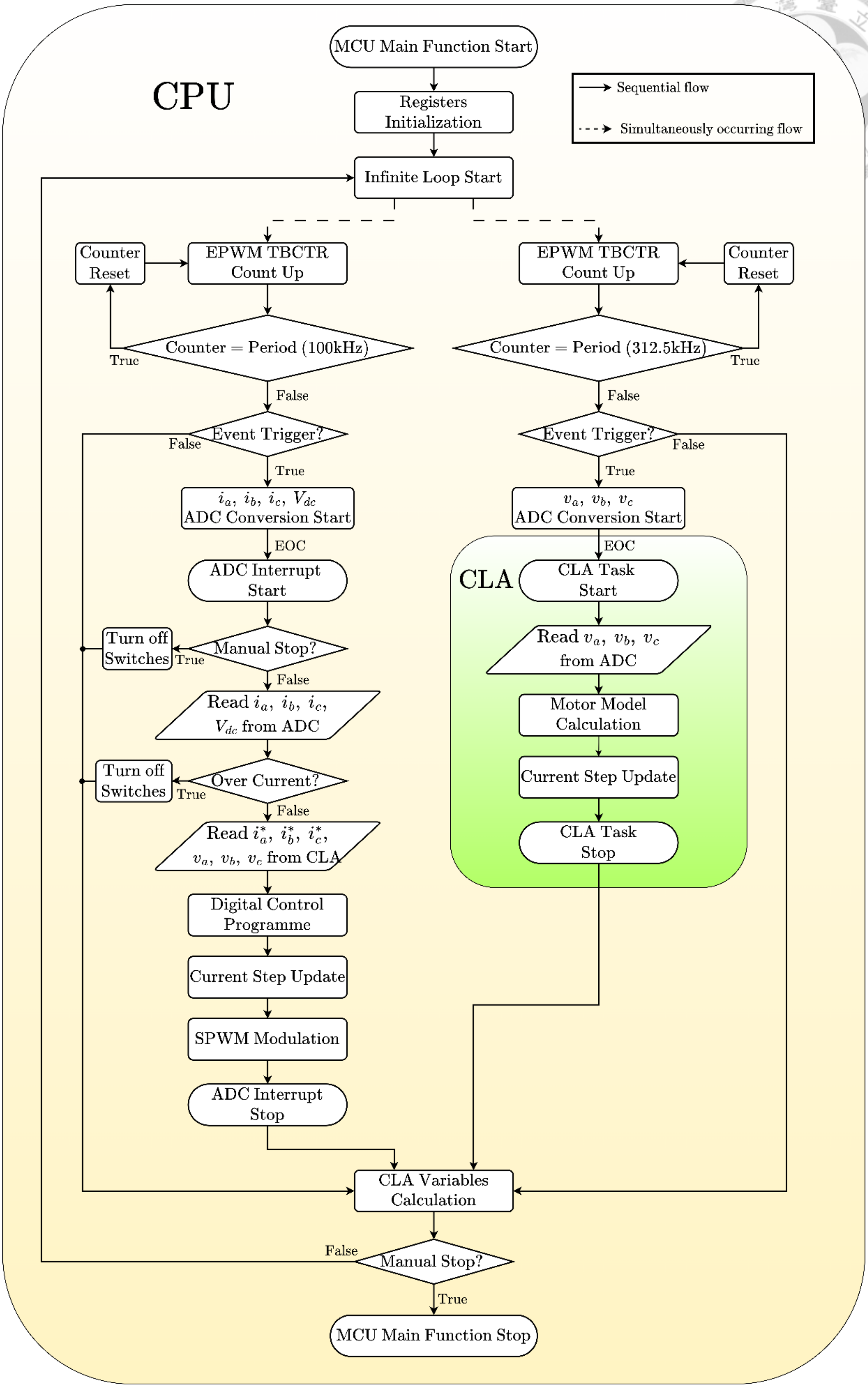

Fig. 5.3 The flowchart of PHIL firmware.

doi:10.6342/NTU202302551

5.2 Experiment under R-Unbalance Scenario

5.2.1 R-Unbalance Experiment with PI Control

First of all, Fig. 5.4 illustrates the oscilloscope screenshot of three-phase currents under R-Unbalance experiment with PI control. The acquired data from the oscilloscope can then be saved and further analyzed using MATLAB for detailed comparison.

Fig. 5.5 shows the three-phase currents in the time domain and the αβ-axis currents in stationary frame under R-Unbalance experiment with PI control for the comparison. Note that the comparison for the experiment focuses on the difference between the ideal currents obtained from the corresponding simulation, $i_{a.ideal}$, $i_{b.ideal}$, and $i_{c.ideal}$, and the real three-phase currents flowing through the power stage ,i_a, i_b, and i_c, which are referred to as actual currents in this thesis.

From Fig. 5.5(a) and Fig. 5.5(b), it can be found that the difference between the ideal currents and the actual currents are unnoticeable, which is a decent result already.

Fig. 5.6 and Fig. 5.7 show the dq-axis reference currents and feedback currents in the time domain and the frequency domain under R-Unbalance experiment with PI control for the comparison, where i_d^*, i_q^*, i_d, and i_q are the dq-axis reference currents and feedback currents, respectively.

From Fig. 5.6(a), Fig. 5.6(b), Fig. 5.7(a), and Fig. 5.7(b), it is evident that there is a notable error between the dq-axis reference currents and feedback currents in the time domain. Moreover, Fig. 5.6(c), Fig. 5.6(d), Fig. 5.7(c), and Fig. 5.7(d) show the main difference in dq-axis is attributed to the steady-state error in the second harmonic, which is the same conclusion as the corresponding simulation. It is important to mention that in addition to the second harmonic, there is also the presence of the first harmonic (100Hz) in the experimental results. This first harmonic is primarily caused by the offset

doi:10.6342/NTU202302551

differences between the switching node voltage sensors. Despite our initial calibration efforts, it is inevitable that the first harmonic exists in the experimental results for all motor models discussed in this thesis.

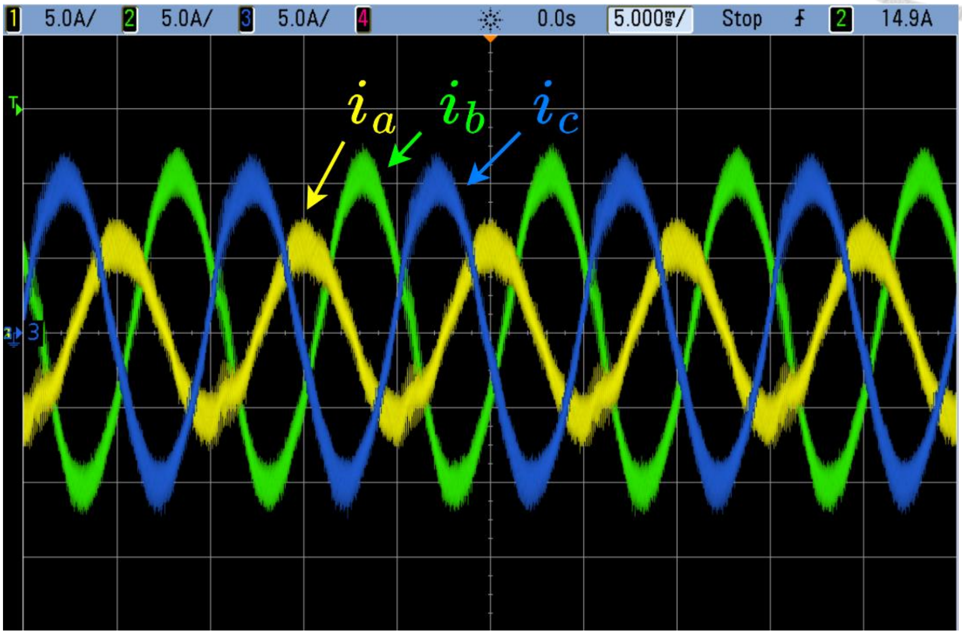

Fig. 5.4 The oscilloscope screenshot of three-phase currents under R-Unbalance experiment with PI control.

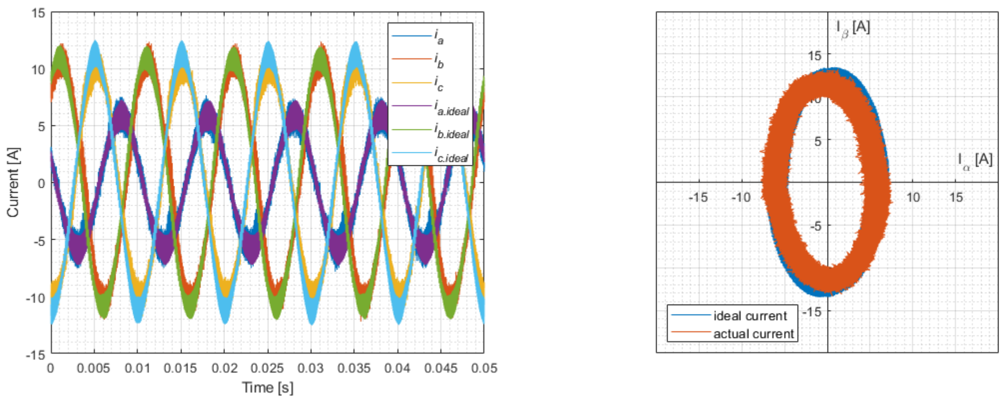

(a) (b)

Fig. 5.5 The comparison diagram for three-phase currents in the time domain and αβ-axis currents in stationary frame under R-Unbalance experiment with PI control (a) The three-phase current comparison between actual currents and ideal currents (b) The αβ-axis current comparison between actual currents and ideal currents.

doi:10.6342/NTU202302551

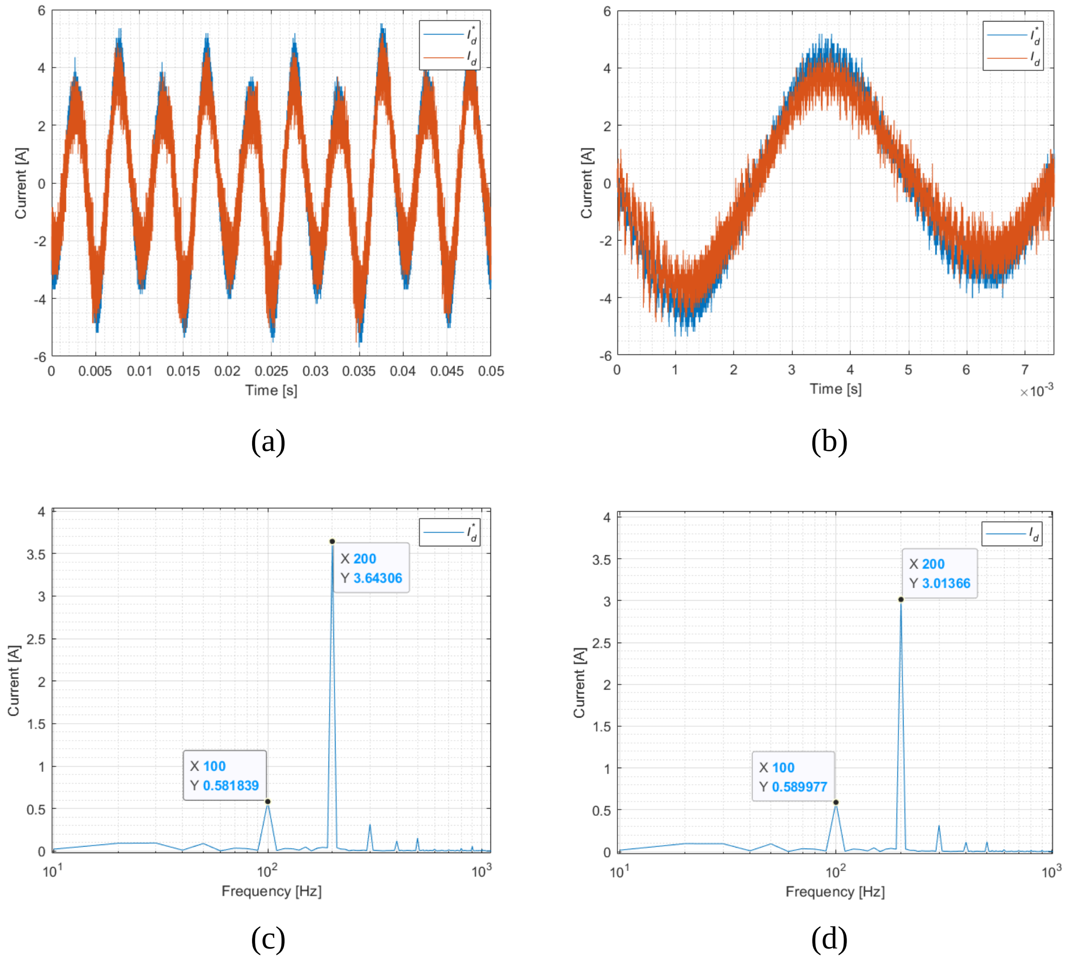

Fig. 5.6 The comparison diagram for the d-axis reference current and feedback current in the time domain and the frequency domain under R-Unbalance experiment with PI control (a) The d-axis current comparison between the reference current and the feedback current in the time domain (b) The zoom-in version of d-axis current comparison in the time domain (c) The d-axis reference current in the frequency domain (d) The d-axis feedback current in the frequency domain.

doi:10.6342/NTU202302551

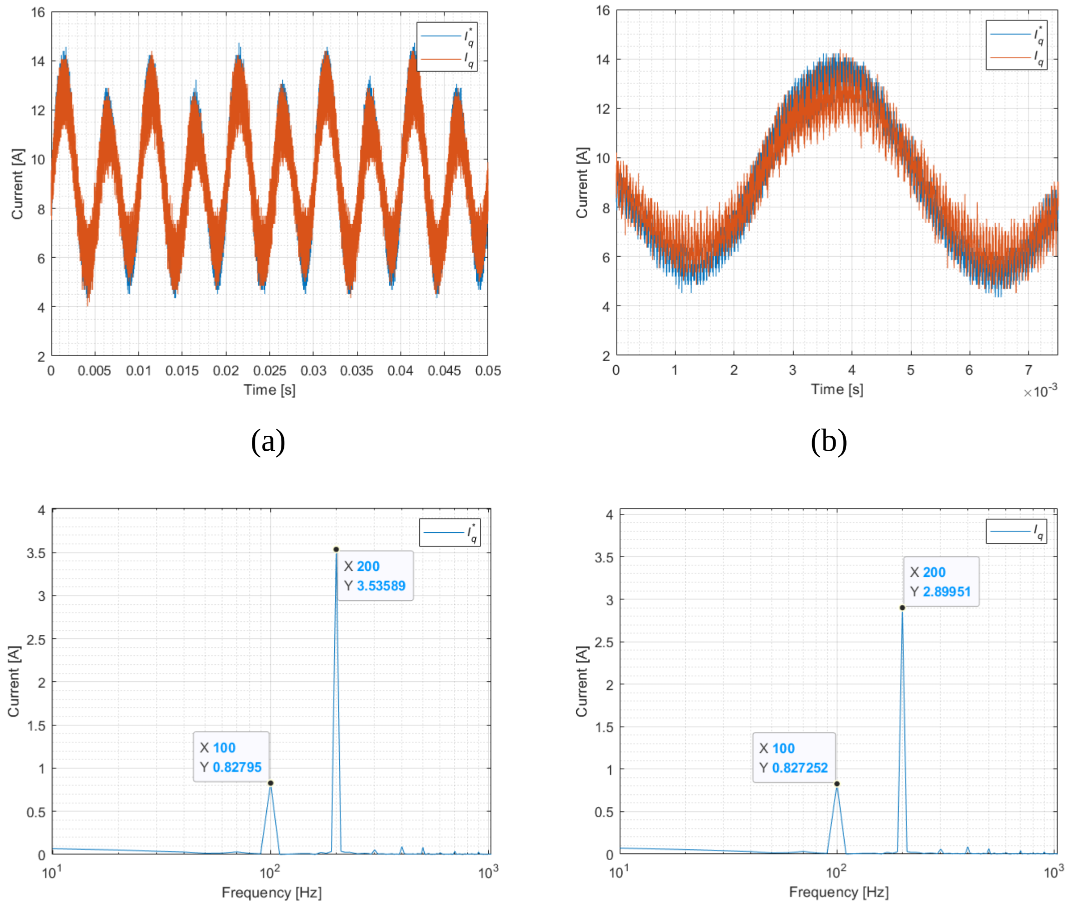

(a) (b)

(c) (d)

Fig. 5.7 The comparison diagram for the q-axis reference current and feedback current in the time domain and the frequency domain under R-Unbalance experiment with PI control (a) The q-axis current comparison between the reference current and the feedback current in the time domain (b) The zoom-in version of q-axis current comparison in the time domain (c) The q-axis reference current in the frequency domain (d) The q-axis feedback current in the frequency domain.

doi:10.6342/NTU202302551

5.2.2 R-Unbalance Experiment with CPIR Control

Fig. 5.8 illustrates the oscilloscope screenshot of three-phase currents under R-Unbalance experiment with CPIR control, and Fig. 5.9 shows the three-phase currents in the time domain and the $\alpha\beta$-axis currents in stationary frame under R-Unbalance experiment with CPIR control for the comparison.

From Fig. 5.9(a) and Fig. 5.9(b), it is evident that the improvement achieved by adopting the CPIR control is not significant, as the original results obtained with the PI control are already satisfactory.

Fig. 5.10 and Fig. 5.11 show the dq-axis reference currents and feedback currents in the time domain and the frequency domain under R-Unbalance experiment with CPIR control for the comparison.

Based on the observations from Fig. 5.10(a), Fig. 5.10(b), Fig. 5.11(a), and Fig. 5.11(b), it is evident that the considerable error between the reference currents and the feedback currents, which is present with the usage of the PI control, is completely eliminated with the adoption of the CPIR control. Additionally, the results depicted in Fig. Fig. 5.10(c), Fig. 5.10(d), Fig. 5.11(c), and Fig. 5.11(d) demonstrate that the proposed CPIR control achieves a steady-state error of less than 1% for the second harmonic, which is the same with the results shown in Section 4.2.2 .

doi:10.6342/NTU202302551

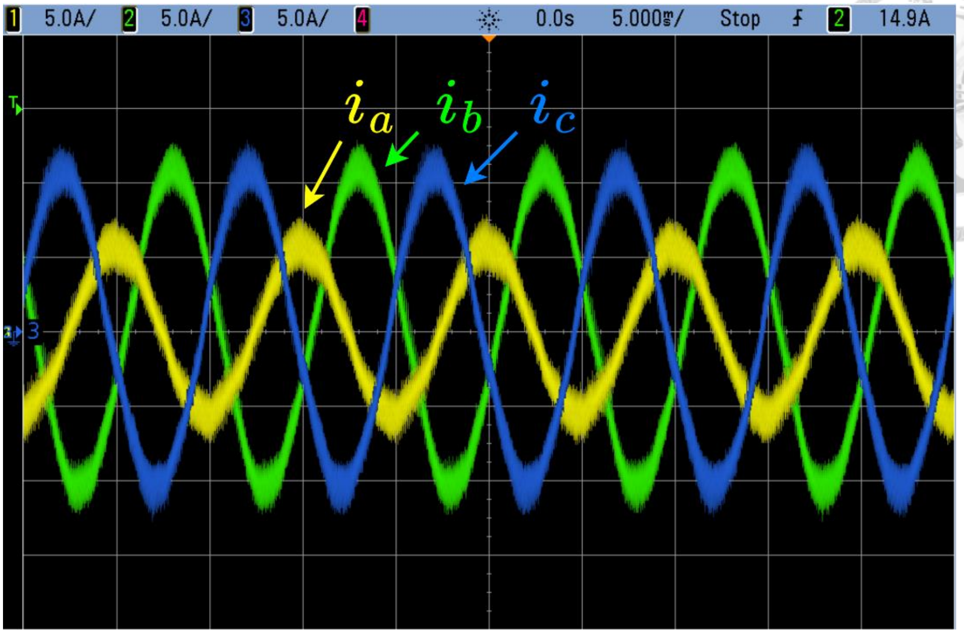

Fig. 5.8 The oscilloscope screenshot of three-phase currents under R-Unbalance experiment with CPIR control.

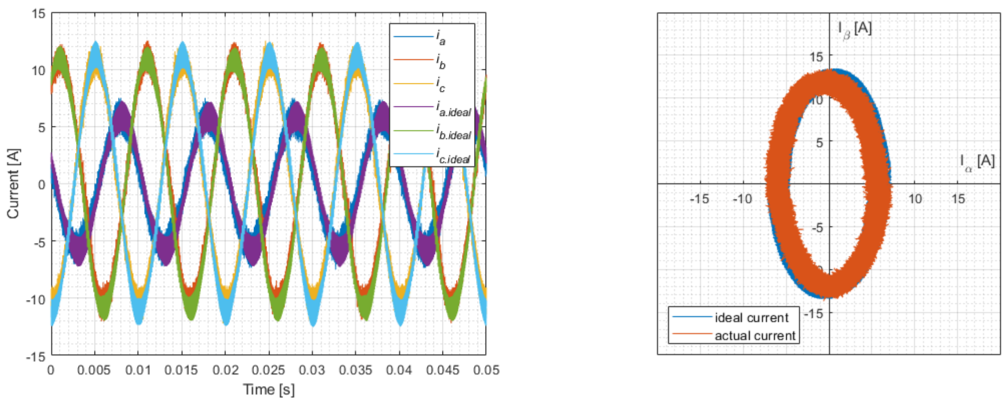

(a) (b)

Fig. 5.9 The comparison diagram for three-phase currents in the time domain and αβ-axis currents in stationary frame under R-Unbalance experiment with CPIR control (a) The three-phase current comparison between actual currents and ideal currents (b) The αβ-axis current comparison between actual currents and ideal currents.

doi:10.6342/NTU202302551

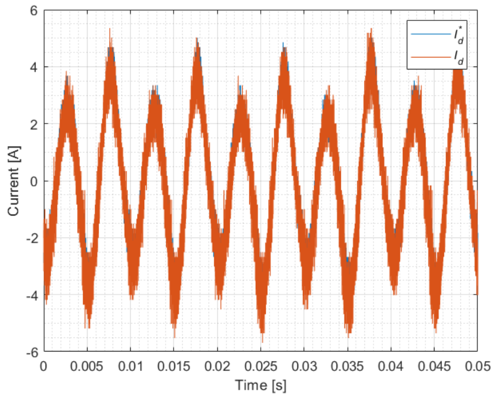

(a)

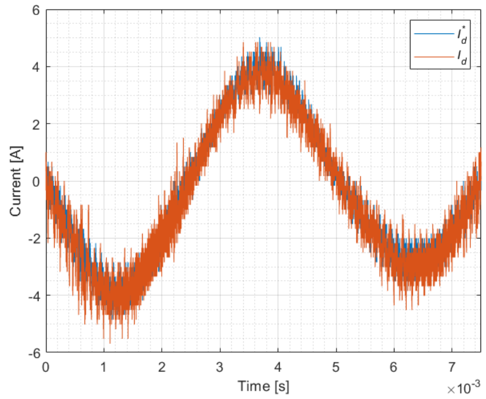

(b)

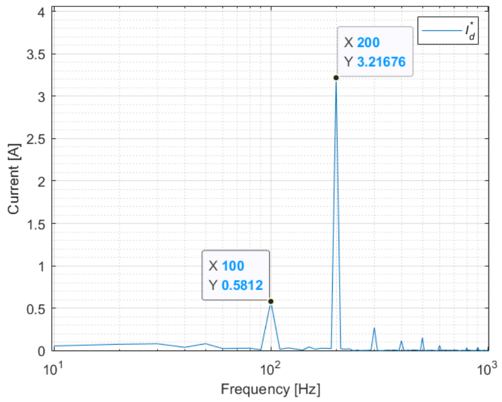

(c)

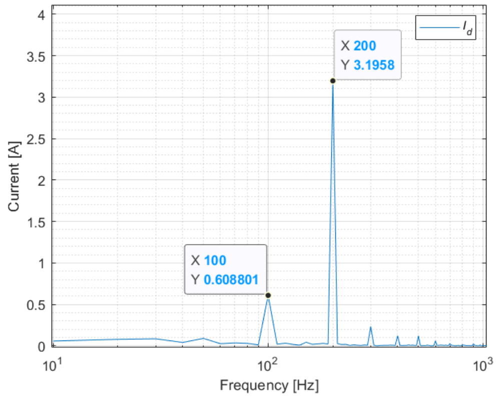

(d)

Fig. 5.10 The comparison diagram for the d-axis reference current and feedback current in the time domain and the frequency domain under R-Unbalance experiment with CPIR control (a) The d-axis current comparison between the reference current and the feedback current in the time domain (b) The zoom-in version of d-axis current comparison in the time domain (c) The d-axis reference current in the frequency domain (d) The d-axis feedback current in the frequency domain.

doi:10.6342/NTU202302551

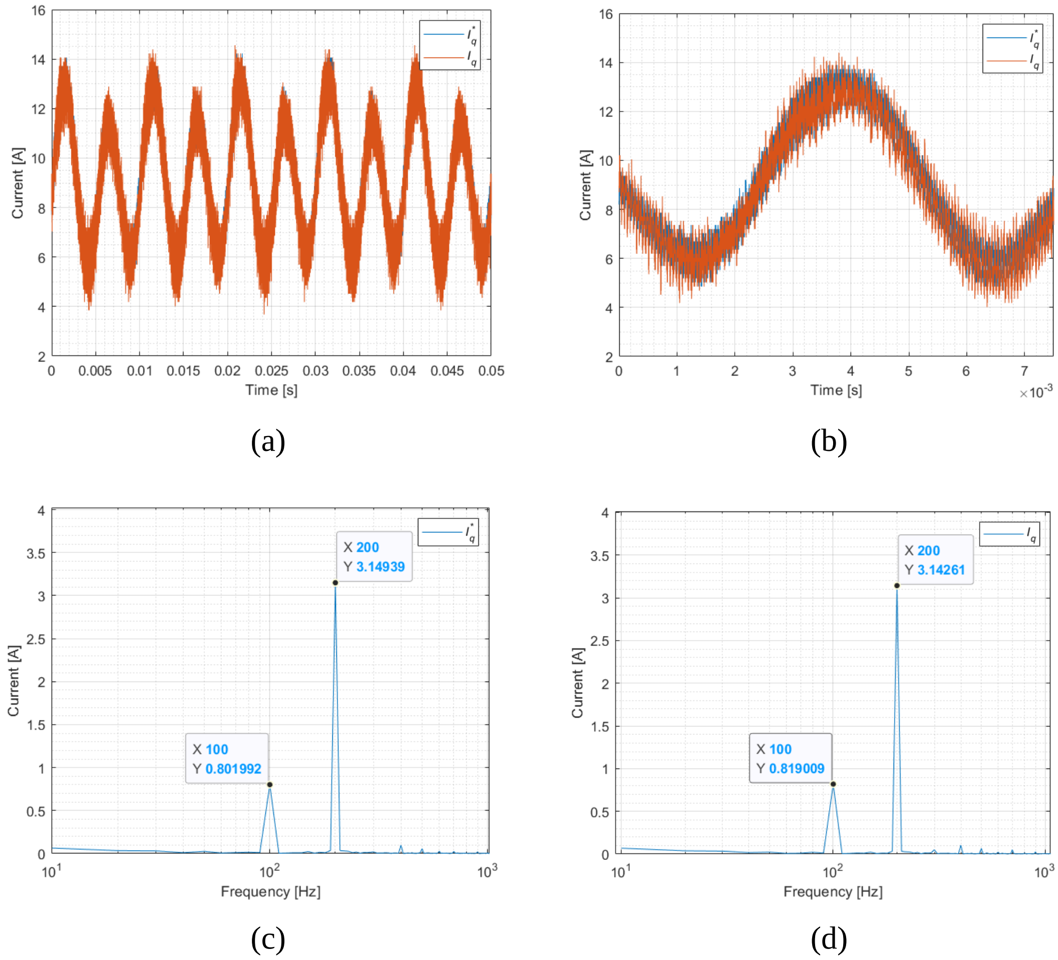

Fig. 5.11 The comparison diagram for the q-axis reference current and feedback current in the time domain and the frequency domain under R-Unbalance experiment with CPIR control (a) The q-axis current comparison between the reference current and the feedback current in the time domain (b) The zoom-in version of q-axis current comparison in the time domain (c) The q-axis reference current in the frequency domain (d) The q-axis feedback current in the frequency domain.

doi:10.6342/NTU202302551

5.3 Experiment under OPF Scenario

5.3.1 OPF Experiment with PI Control

Fig. 5.12 illustrates the oscilloscope screenshot of three-phase currents under OPF experiment with PI control, and Fig. 5.13 shows the three-phase currents in the time domain and the $\alpha\beta$-axis currents in stationary frame under OPF experiment with PI control for the comparison.

From Fig. 5.13(a), it is apparent that there is a noticeable difference between the ideal currents and the actual currents. As a result, the graph illustrating the actual currents in Fig. 5.13(b) deviates from the desired straight line shape that is expected for the OPF scenario.

Fig. 5.14 and Fig. 5.15 show the dq-axis reference currents and feedback currents in the time domain and the frequency domain under OPF experiment with PI control for the comparison.

From Fig. 5.14(a), Fig. 5.14(b), Fig. 5.15(a), and Fig. 5.15(b), it is clear that there is a significant error between the dq-axis reference currents and feedback currents in the time domain. Furthermore, Fig. 5.14(c), Fig. 5.14(d), Fig. 5.15(c), and Fig. 5.15(d) highlight that the difference in the dq-axis is primarily attributed to the presence of steady-state error in the second harmonic as expect.

doi:10.6342/NTU202302551

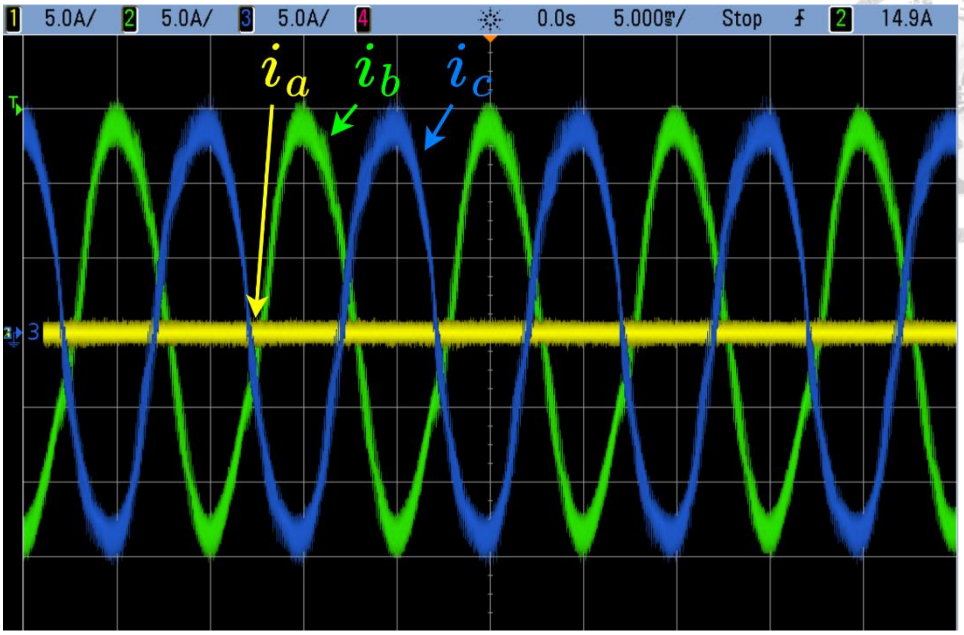

Fig. 5.12 The oscilloscope screenshot of three-phase currents under OPF experiment with PI control.

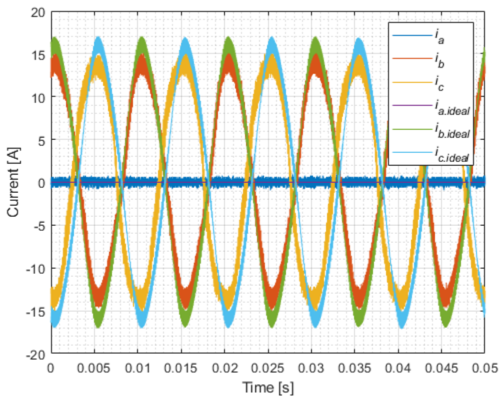

(a)

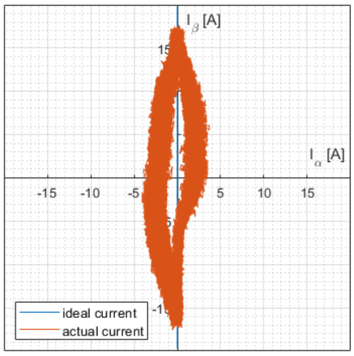

(b)

Fig. 5.13 The comparison diagram for three-phase currents in the time domain and αβ-axis currents in stationary frame under OPF experiment with PI control (a) The three-phase current comparison between actual currents and ideal currents (b) The αβ-axis current comparison between actual currents and ideal currents.

doi:10.6342/NTU202302551

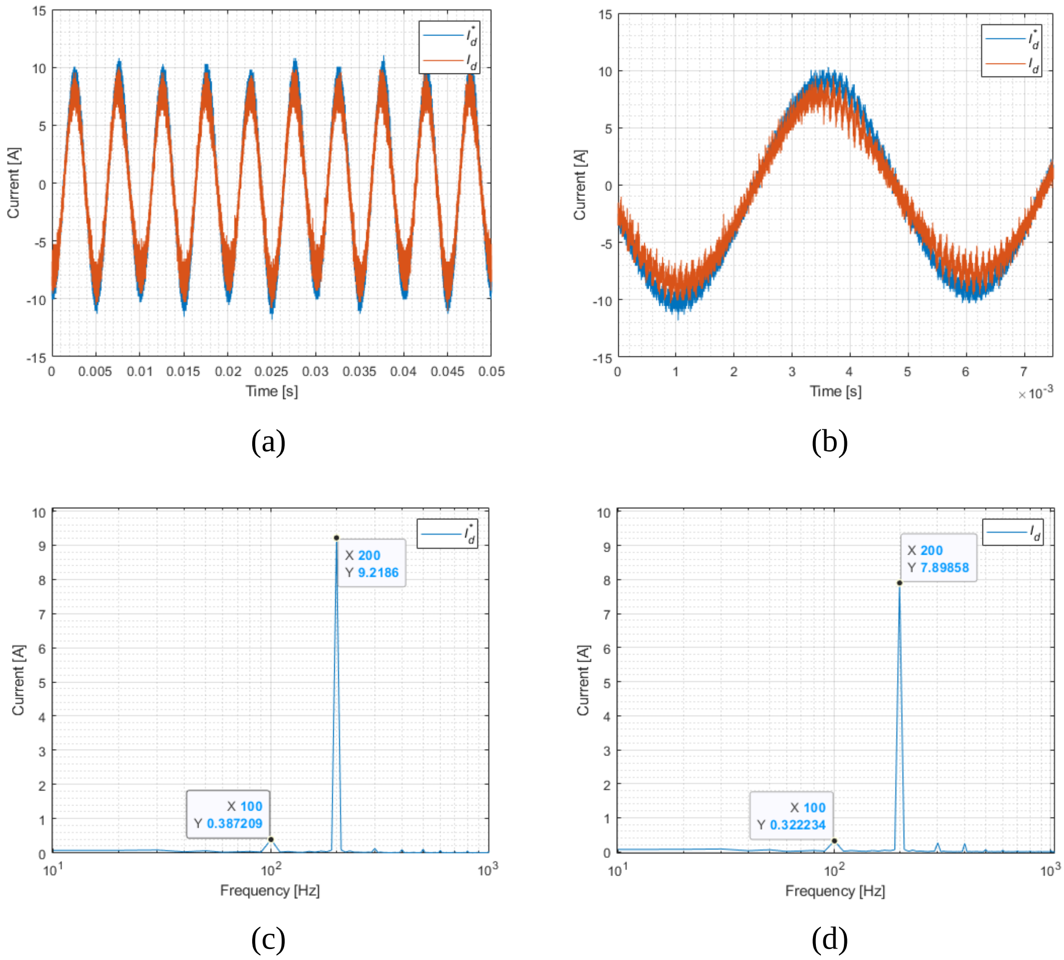

Fig. 5.14 The comparison diagram for the d-axis reference current and feedback current in the time domain and the frequency domain under OPF experiment with PI control (a) The d-axis current comparison between the reference current and the feedback current in the time domain (b) The zoom-in version of d-axis current comparison in the time domain (c) The d-axis reference current in the frequency domain (d) The d-axis feedback current in the frequency domain.

doi:10.6342/NTU202302551

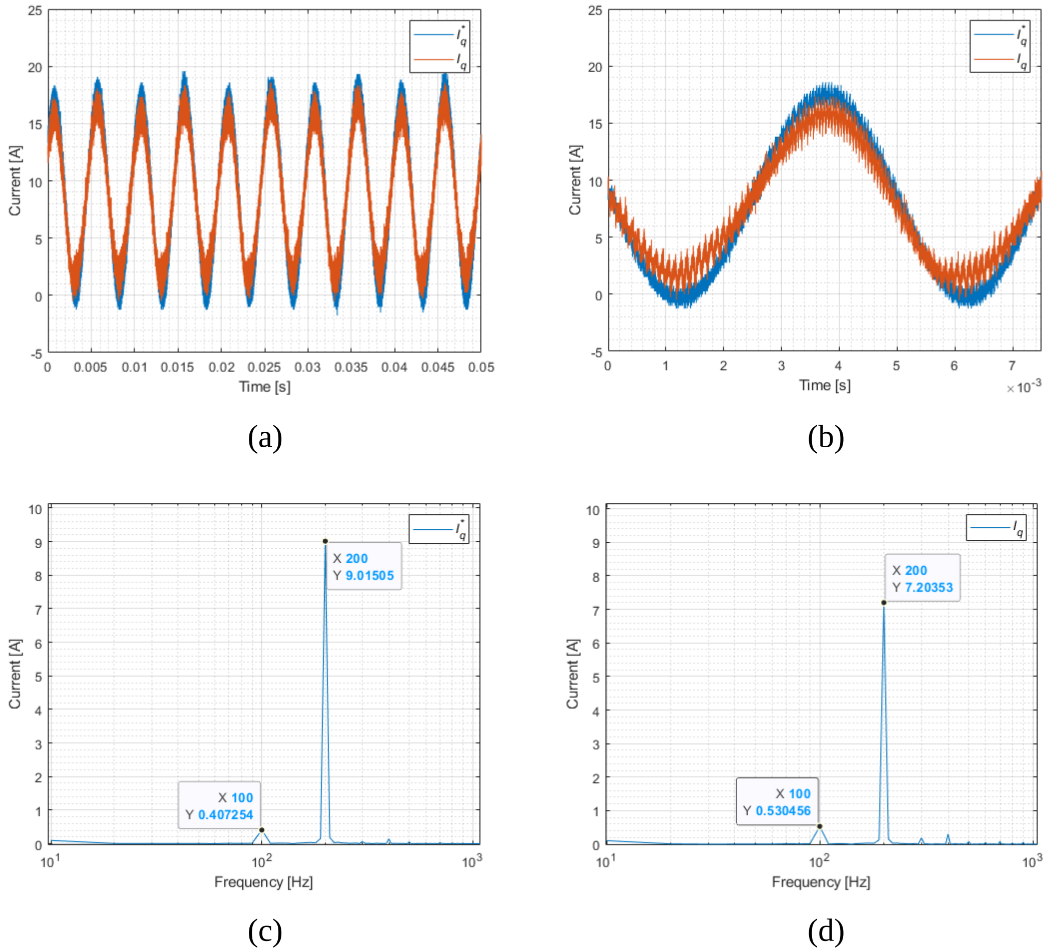

Fig. 5.15 The comparison diagram for the q-axis reference current and feedback current in the time domain and the frequency domain under OPF experiment with PI control (a) The q-axis current comparison between the reference current and the feedback current in the time domain (b) The zoom-in version of q-axis current comparison in the time domain (c) The q-axis reference current in the frequency domain (d) The q-axis feedback current in the frequency domain.

doi:10.6342/NTU202302551

5.3.2 OPF Experiment with CPIR Control

Fig. 5.16 illustrates the oscilloscope screenshot of three-phase currents under OPF experiment with CPIR control, and Fig. 5.17 shows the three-phase currents in the time domain and the $\alpha\beta$-axis currents in stationary frame under OPF experiment with CPIR control for the comparison.

From Fig. 5.17(a), it is evident that the difference between the ideal currents and the actual currents is dramatically reduced compared to the results obtained with the PI control. Consequently, the graph illustrating the actual currents in Fig. 5.17(b) closely approximates a straight line, indicating enhanced performance and increased accuracy.

Fig. 5.18 and Fig. 5.19 show the dq-axis reference currents and feedback currents in the time domain and the frequency domain under OPF experiment with CPIR control for the comparison.

Based on the observations from Fig. 5.18(a), Fig. 5.18(b), Fig. 5.19(a), and Fig. 5.19(b), it is obvious that the CPIR control effectively mitigates the substantial error observed between the reference currents and the feedback currents, which is present when using the PI control. Moreover, the results shown in Fig. 5.18(c), Fig. 5.18(d), Fig. 5.19(c), and Fig. 5.19(d) demonstrate the achievement of the CPIR control in suppressing the second harmonic, with a steady-state error of approximately 3%.

doi:10.6342/NTU202302551

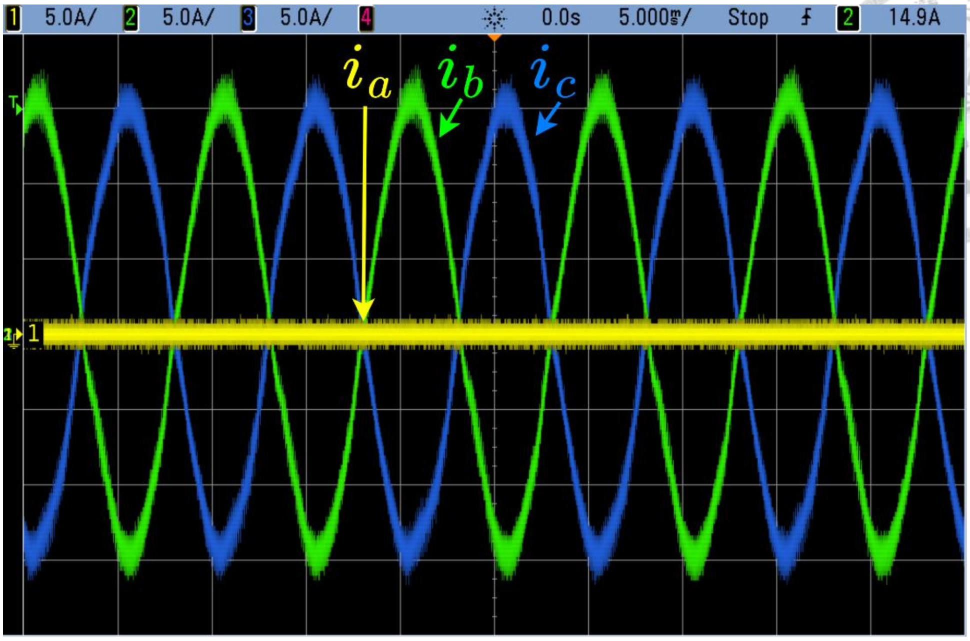

Fig. 5.16 The oscilloscope screenshot of three-phase currents under OPF experiment with CPIR control.

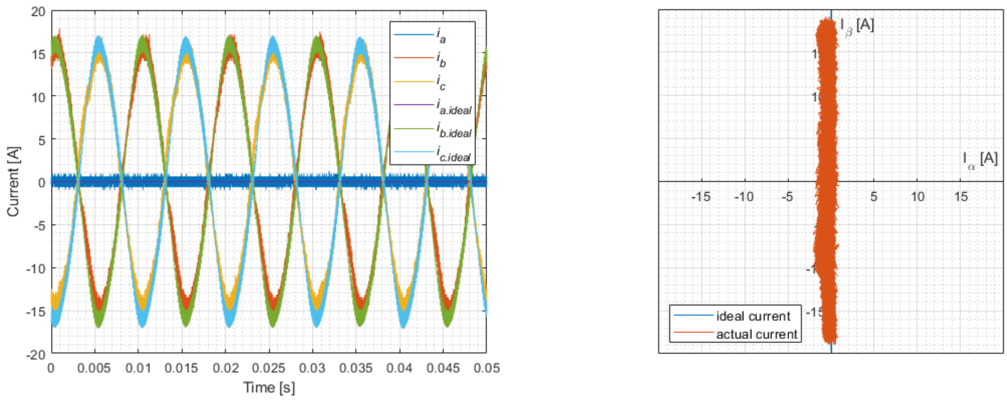

(a) (b)

Fig. 5.17 The comparison diagram for three-phase currents in the time domain and αβ-axis currents in stationary frame under OPF experiment with CPIR control (a) The three-phase current comparison between actual currents and ideal currents (b) The αβ-axis current comparison between actual currents and ideal currents.

doi:10.6342/NTU202302551

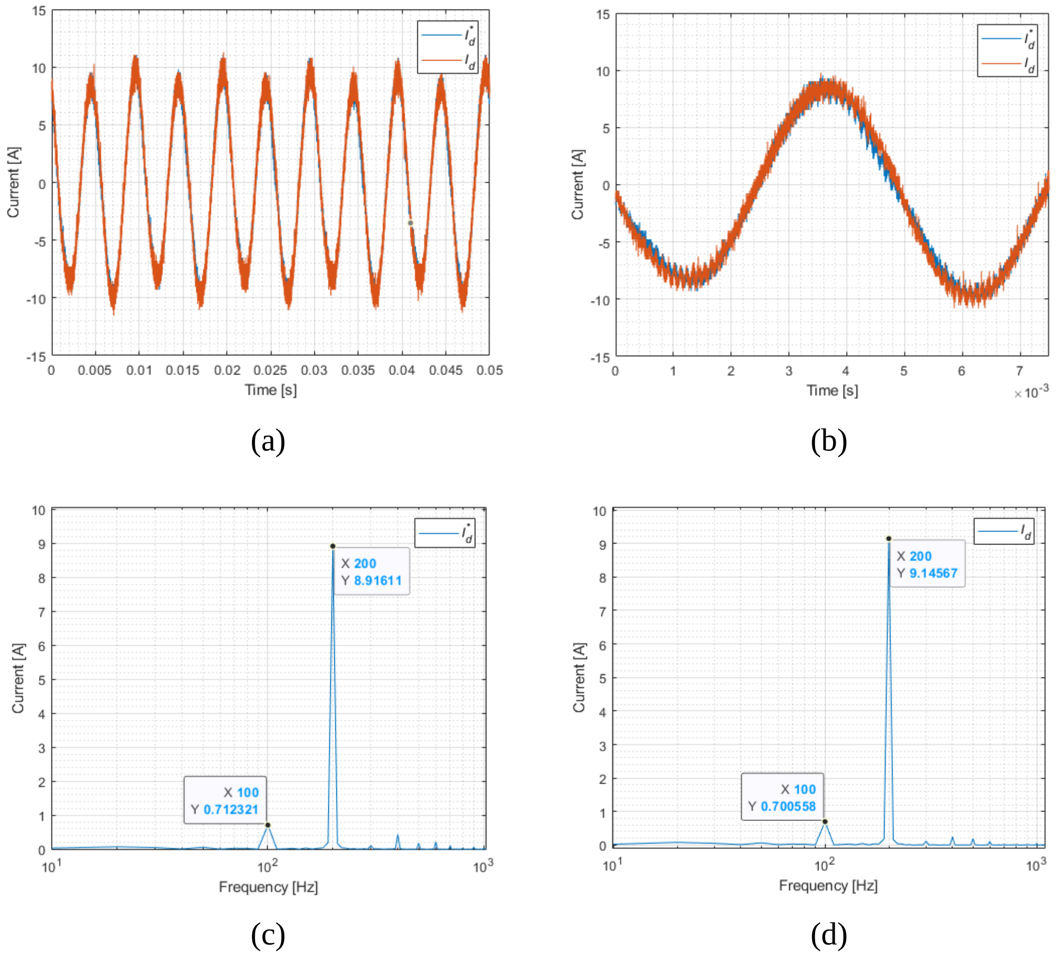

Fig. 5.18 The comparison diagram for the d-axis reference current and feedback current in the time domain and the frequency domain under OPF experiment with CPIR control (a) The d-axis current comparison between the reference current and the feedback current in the time domain (b) The zoom-in version of d-axis current comparison in the time domain (c) The d-axis reference current in the frequency domain (d) The d-axis feedback current in the frequency domain.

doi:10.6342/NTU202302551

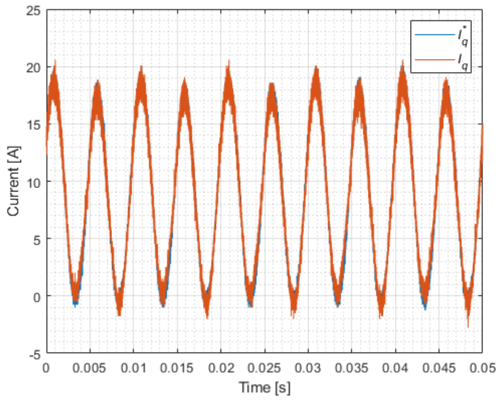

(a)

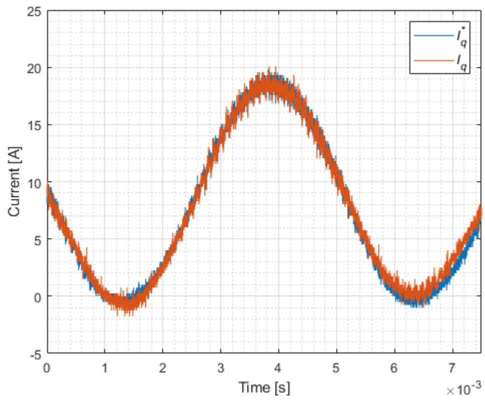

(b)

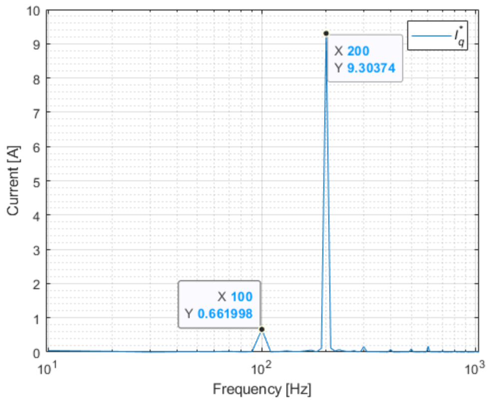

(c)

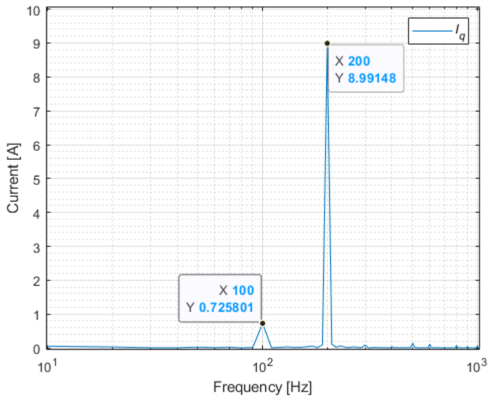

(d)

Fig. 5.19 The comparison diagram for the q-axis reference current and feedback current in the time domain and the frequency domain under OPF experiment with CPIR control (a) The q-axis current comparison between the reference current and the feedback current in the time domain (b) The zoom-in version of q-axis current comparison in the time domain (c) The q-axis reference current in the frequency domain (d) The q-axis feedback current in the frequency domain.

doi:10.6342/NTU202302551

5.4 Experiment under ISCF Scenario

5.4.1 ISCF Experiment with PI Control

Fig. 5.20 illustrates the oscilloscope screenshot of three-phase currents under ISCF experiment with PI control, and Fig. 5.21 shows the three-phase currents in the time domain and the αβ-axis currents in stationary frame under ISCF experiment with PI control for the comparison.

From Fig. 5.21(a) and Fig. 5.21(b), it is clear that the difference between the ideal currents and the actual currents primarily occurs at the switching-related frequency, especially for A-phase current, where the short-circuit fault occurred.

Fig. 5.22 and Fig. 5.23 show the dq-axis reference currents and feedback currents in the time domain and the frequency domain under ISCF experiment with PI control for the comparison.

Based on the observations from Fig. 5.22(a), Fig. 5.22(b), Fig. 5.23(a), and Fig. 5.23(b), it is apparent that there is a notable error between the dq-axis reference currents and feedback currents in the time domain. These results differ from the simulation results shown in Fig. 4.17(a), Fig. 4.17(b), Fig. 4.18(a), and Fig. 4.18(b). To explain this difference, Fig. 5.22(c), Fig. 5.22(d), Fig. 5.23(c), and Fig. 5.23(d) are referred, where it is evident that the first harmonic contributes significantly to the dq-axis currents. Additionally, the magnitude of the components at switching-related frequencies, which are 9.5kHz and 19kHz, in the reference currents is considerably smaller compared to the simulation results. This difference may arise from the limited ability of the voltage sensors to fully capture the switching-related harmonics, likely due to the presence of anti-aliasing filters in the implementation.

doi:10.6342/NTU202302551

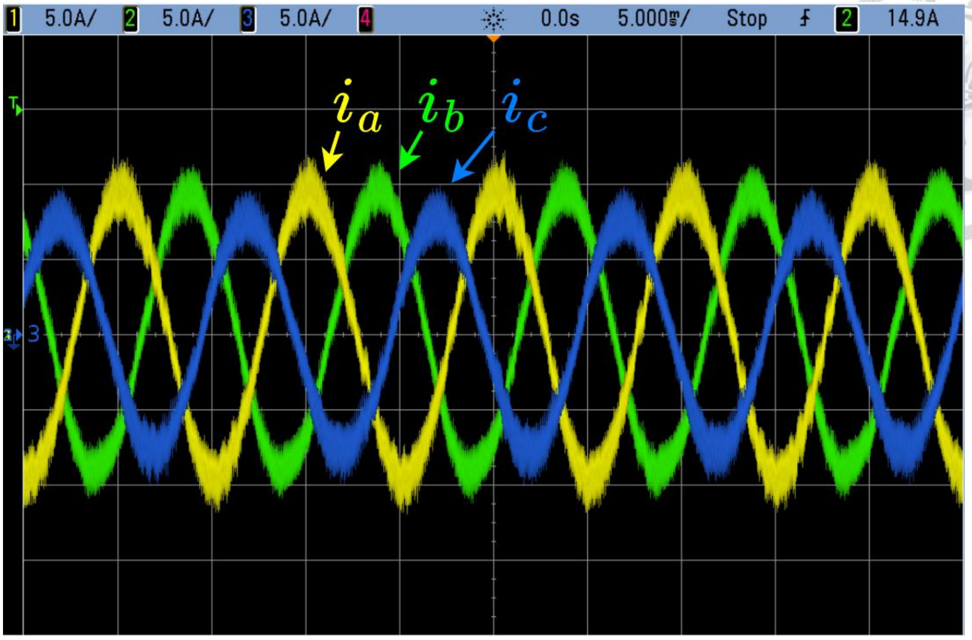

Fig. 5.20 The oscilloscope screenshot of three-phase currents under ISCF experiment with PI control.

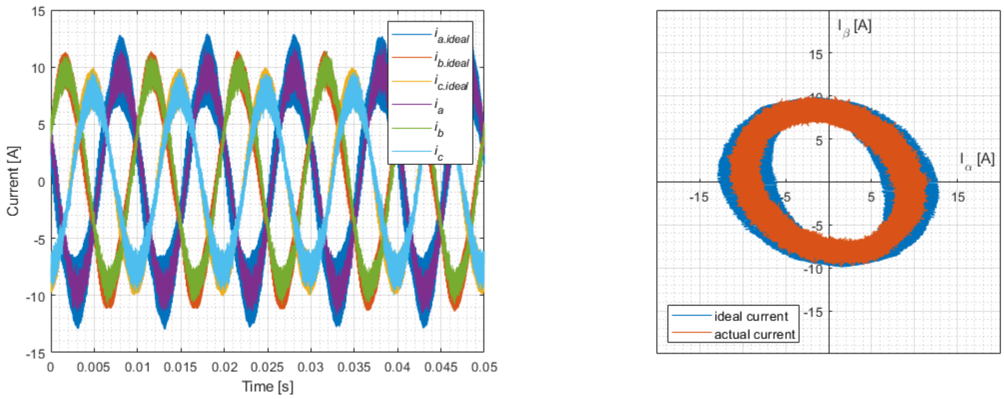

(a) (b)

Fig. 5.21 The comparison diagram for three-phase currents in the time domain and αβ-axis currents in stationary frame under ISCF experiment with PI control (a) The three-phase current comparison between actual currents and ideal currents (b) The αβ-axis current comparison between actual currents and ideal currents.

doi:10.6342/NTU202302551

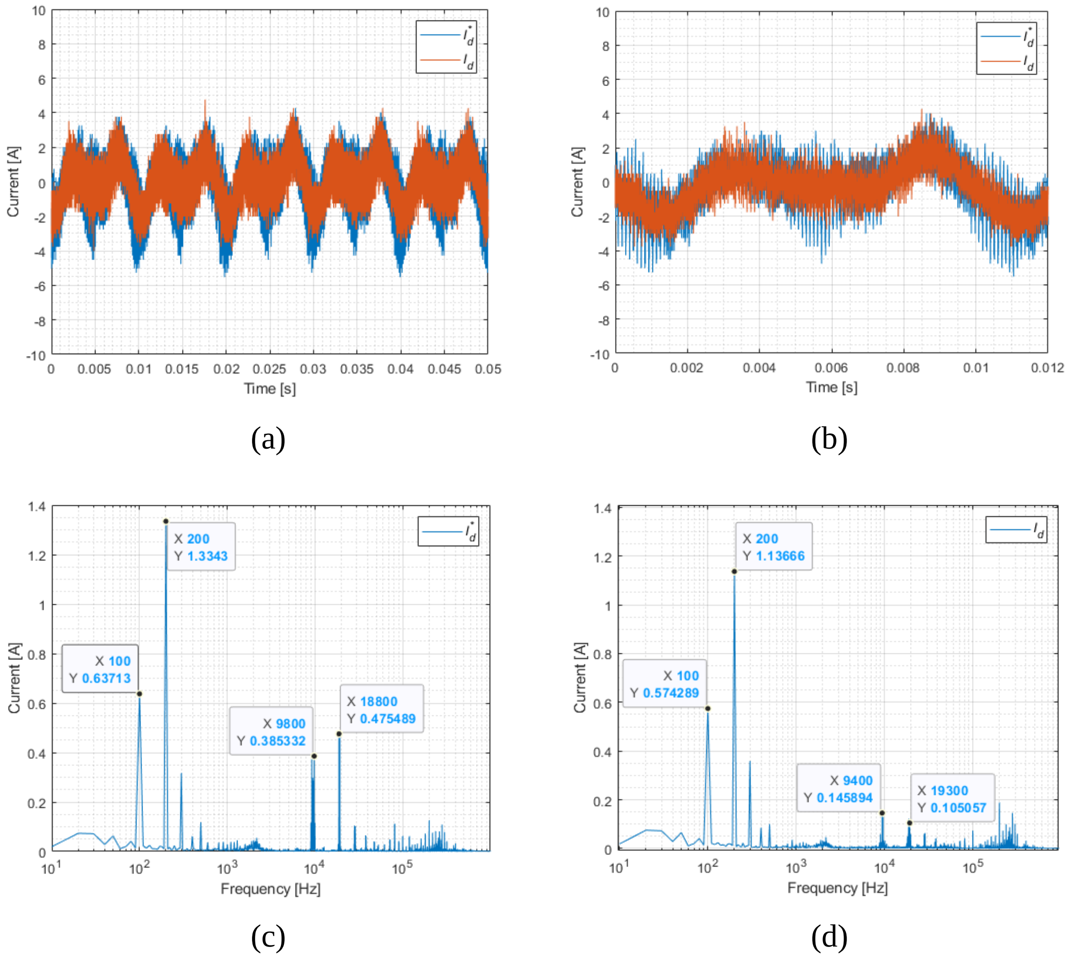

Fig. 5.22 The comparison diagram for the d-axis reference current and feedback current in the time domain and the frequency domain under ISCF experiment with PI control (a) The d-axis current comparison between the reference current and the feedback current in the time domain (b) The zoom-in version of d-axis current comparison in the time domain (c) The d-axis reference current in the frequency domain (d) The d-axis feedback current in the frequency domain.

doi:10.6342/NTU202302551

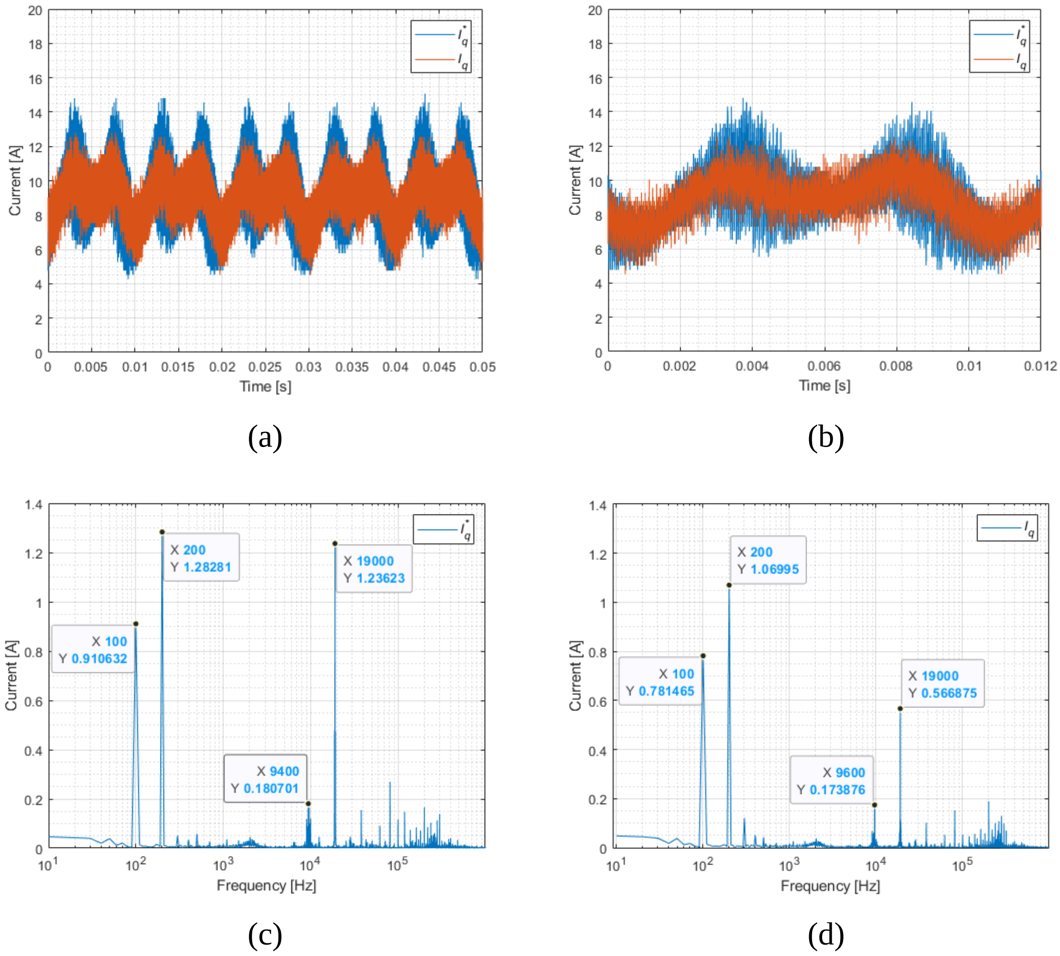

Fig. 5.23 The comparison diagram for the q-axis reference current and feedback current in the time domain and the frequency domain under ISCF experiment with PI control (a) The q-axis current comparison between the reference current and the feedback current in the time domain (b) The zoom-in version of q-axis current comparison in the time domain (c) The q-axis reference current in the frequency domain (d) The q-axis feedback current in the frequency domain.

doi:10.6342/NTU202302551

5.4.2 ISCF Experiment with CPIR Control

Fig. 5.24 illustrates the oscilloscope screenshot of three-phase currents under ISCF experiment with CPIR control, and Fig. 5.25 shows the three-phase currents in the time domain and the $\alpha\beta$-axis currents in stationary frame under ISCF experiment with CPIR control for the comparison.

From Fig. 5.25(a) and Fig. 5.25(b), it is clear that the current results obtained with the CPIR control suffer from the same issues as those obtained with the PI control, specifically the switching-related harmonics.

Fig. 5.26 and Fig. 5.27 show the dq-axis reference currents and feedback currents in the time domain and the frequency domain under ISCF experiment with CPIR control for the comparison.

Based on the observations from Fig. 5.26(a), Fig. 5.26(b), Fig. 5.27(a), and Fig. 5.27(b), there are no significant discernible differences between the outcomes obtained with the CPIR control and those obtained with the PI control. However, as shown in Fig. 5.26(c), Fig. 5.26(d), Fig. 5.27(c), and Fig. 5.27(d), the CPIR control successfully suppress the steady-state error in the second harmonic, as expected. Nonetheless, it is important to note that the errors arising from the near 9.5kHz, which is the switching frequency of the MUT, and near 19kHz, whitch is twice the switching frequency of the MUT, components remain unsolved.

doi:10.6342/NTU202302551

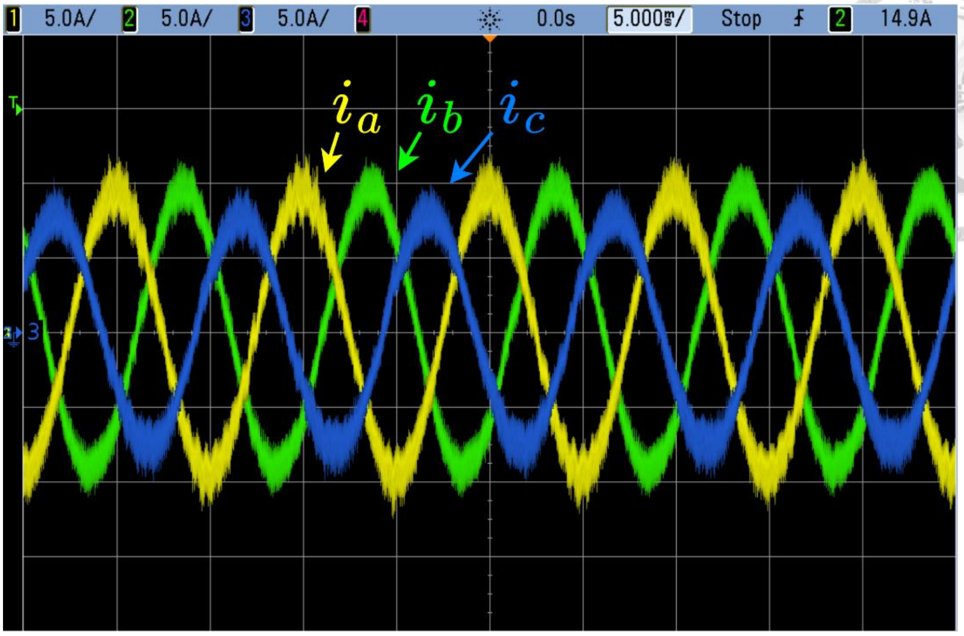

Fig. 5.24 The oscilloscope screenshot of three-phase currents under ISCF experiment with CPIR control.

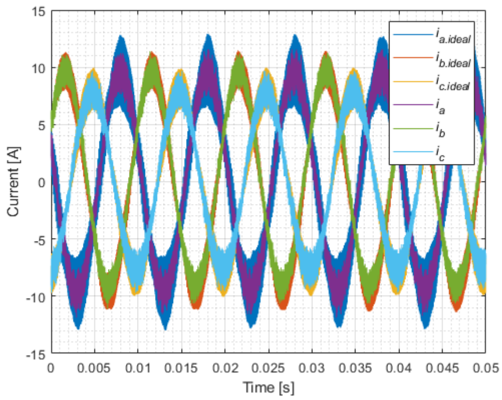

(a)

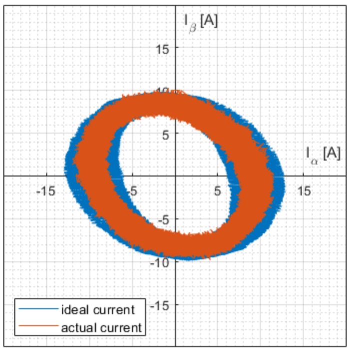

(b)

Fig. 5.25 The comparison diagram for three-phase currents in the time domain and αβ-axis currents in stationary frame under ISCF experiment with CPIR control (a) The three-phase current comparison between actual currents and ideal currents (b) The αβ-axis current comparison between actual currents and ideal currents.

doi:10.6342/NTU202302551

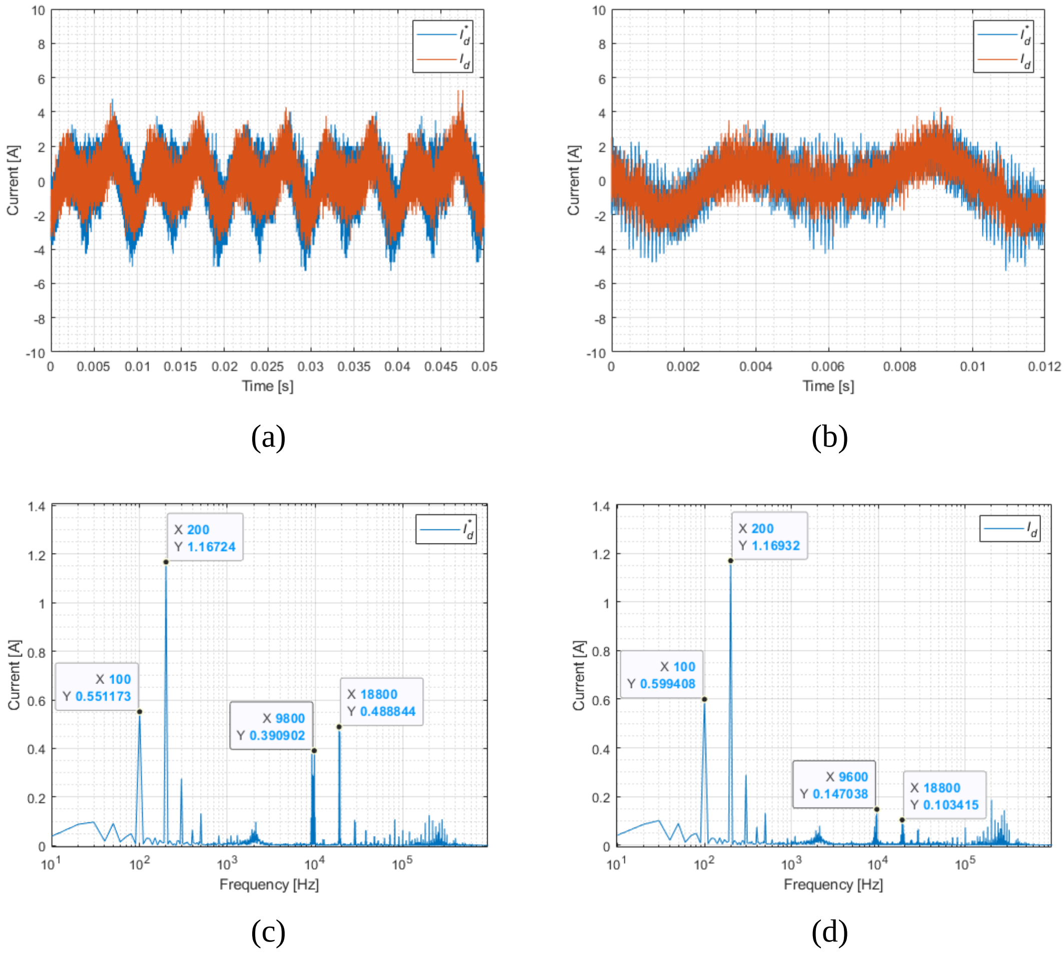

Fig. 5.26 The comparison diagram for the d-axis reference current and feedback current in the time domain and the frequency domain under ISCF experiment with CPIR control (a) The d-axis current comparison between the reference current and the feedback current in the time domain (b) The zoom-in version of d-axis current comparison in the time domain (c) The d-axis reference current in the frequency domain (d) The d-axis feedback current in the frequency domain.

doi:10.6342/NTU202302551

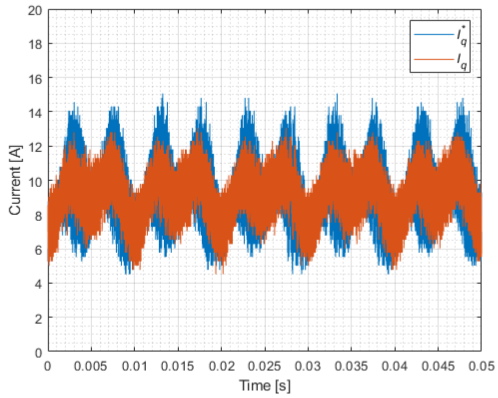

(a)

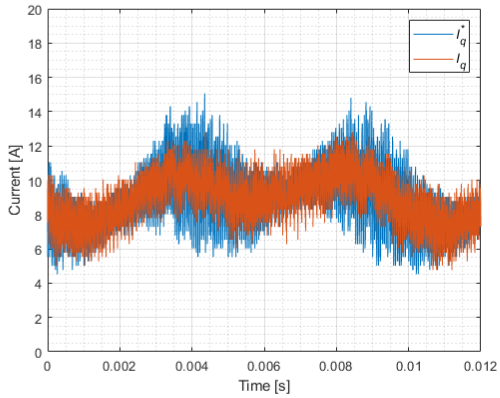

(b)

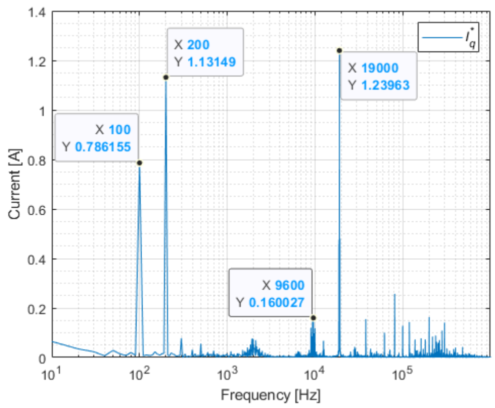

(c)

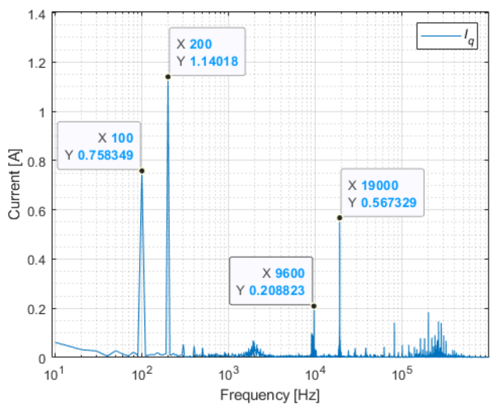

(d)

Fig. 5.27 The comparison diagram for the q-axis reference current and feedback current in the time domain and the frequency domain under ISCF experiment with CPIR control (a) The q-axis current comparison between the reference current and the feedback current in the time domain (b) The zoom-in version of q-axis current comparison in the time domain (c) The q-axis reference current in the frequency domain (d) The q-axis feedback current in the frequency domain.

doi:10.6342/NTU202302551

5.5 Comparative Data

To showcase the performance of PHIL emulation utilizing CPIR control, a comprehensive comparison is needed apparently. Thus, in this section, three comparative data are provided to convince the readers from different aspects.

5.5.1 Second Order Harmonic

First, the most intuitive way to demonstrate the control performance is through the comparison of second order harmonic tracking ability between the traditional decoupling PI control to the proposed CPIR control, since the CPIR control is designed to track the second order harmonic with zero steady-state error.

The diagram of the error index with the aspect of second order harmonic is shown in Fig. 5.28, where the error index is calculated based on the results from Fig. 5.6, Fig. 5.7, Fig. 5.10, Fig. 5.11, Fig. 5.14, Fig. 5.15, Fig. 5.18, Fig. 5.19, Fig. 5.22, Fig. 5.23, Fig. 5.26, and Fig. 5.27 while the error index is defined as (5.1).

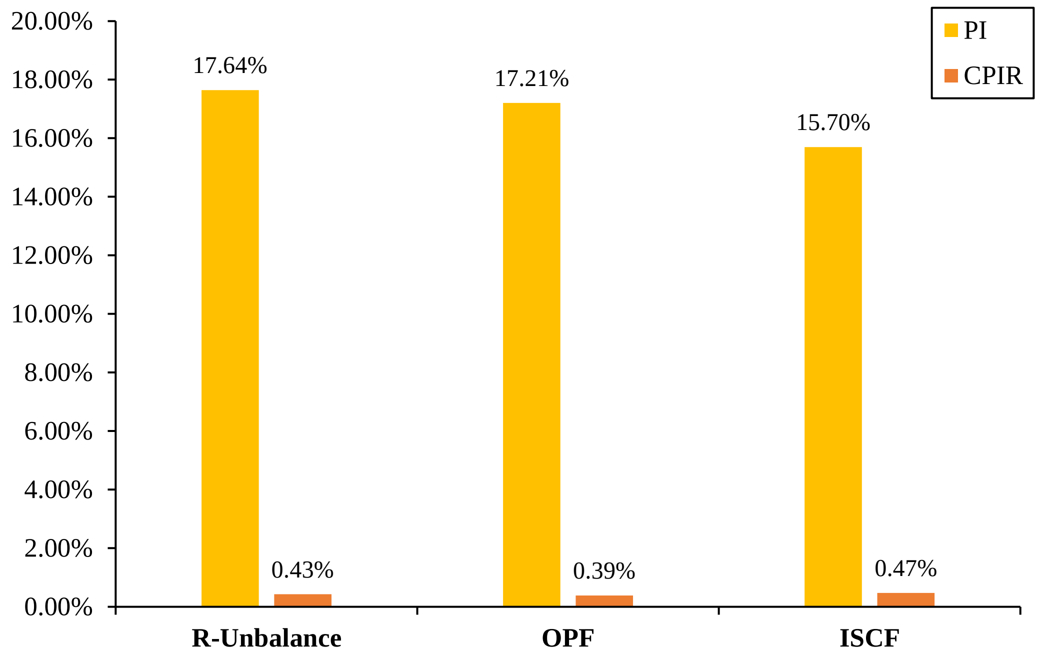

Fig. 5.28 The diagram of the error index with the aspect of second order harmonic.

$$error\ index(\%) = \frac{1}{2}\left(\left|\frac{i^*_{d@200Hz} - i_{d@200Hz}}{i^*_{d@200Hz}}\right| + \left|\frac{i^*_{q@200Hz} - i_{q@200Hz}}{i^*_{q@200Hz}}\right|\right) \cdot 100\% \quad (5.1)$$

From Fig. 5.28, it is clear that by adopting the CPIR control, the error index of second order harmonic can drop from roughly 16% to 0.4%, indicating the significant improvement for the control performance. However, for the emulation capability, it is

doi:10.6342/NTU202302551

incomplete to just compare the performance of differen control method. The experiment results should be directly compared to the ideal currents obtained from the simulation shown in Fig. 4.2. Therefore, the next comparative data is provided.

5.5.2 Root-Mean-Square Error

To perform the comprehensive comparson for the emulation capability, the frequently used measure called Root-Mean-Square Error (RMSR) is applied to the three-phase actual current and ideal current, which is obatained from experiment and simulation, respectively. The RMSE calculation in this thesis can be expressed as (5.2).

$$i_{abc.RMSE} = \sqrt{\frac{\left(i_{abc.ideal}(t) - i_{abc}(t)\right)^2}{T}} \tag{5.2}$$

By utilizing the RMSE, the diagram of the error index with the aspect of RMSE is shown in Fig. 5.29, where the error index can be calculated by (5.3).

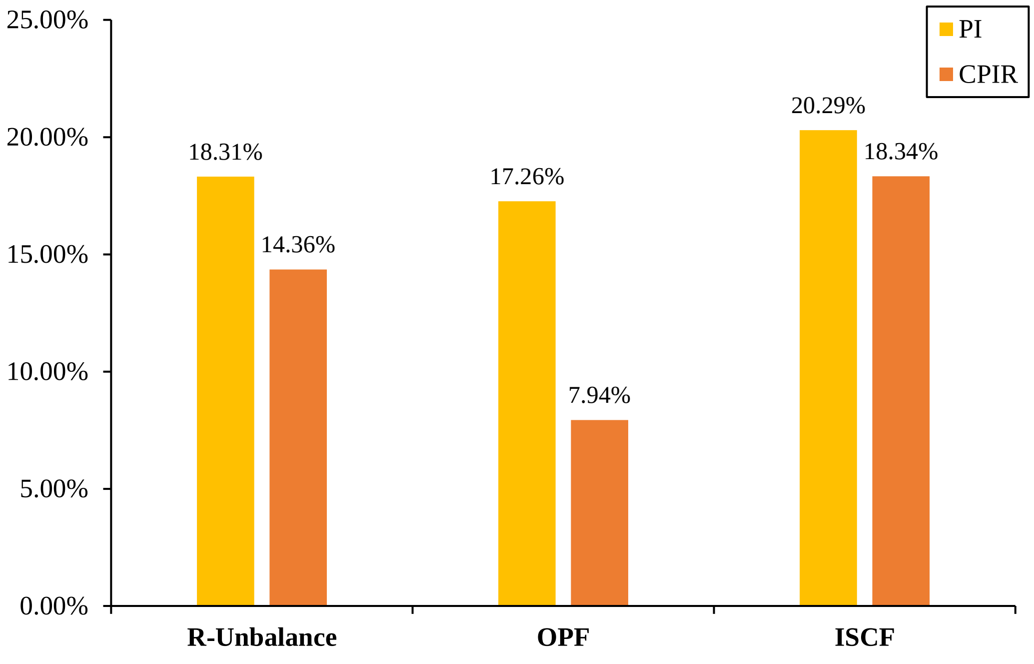

Fig. 5.29 The diagram of the error index with the aspect of RMSE.

$$error\ index(\%) = \frac{1}{3}\left(\frac{i_{a.RMSE}}{i_{a.ideal.RMS}} + \frac{i_{b.RMSE}}{i_{b.ideal.RMS}} + \frac{i_{c.RMSE}}{i_{c.ideal.RMS}}\right) \cdot 100\%, \tag{5.3}$$

where $i_{a.ideal.RMS}$, $i_{b.ideal.RMS}$, and $i_{c.ideal.RMS}$ are the root-mean-square value of three-phase ideal current obtained from corresponding simulatios.

From Fig. 5.29, it is evident that by adopting the CPIR control, the error index in the aspect of RMSE can be reduced. The most significant drop is observed in the OPF

doi:10.6342/NTU202302551

scenario, decreasing from 17.26% to 7.94%. However, since the angular velocity has disturbance due to the fault condition, there is no way to match the phase between actual current and ideal current perfectly. Thus, this comparison is not accurate enough to stand for the emulation capability. Therefore, the next comparative data is provided.

5.5.3 Total Harmonic Distortion Plus Noise

To avoid the error resulted from the phase difference in the aspect of RMSE, the total harmonic distortion plus noise ($THD + N$) is utilized to calculate the proposed Similarity Index (SI) since the calculation is implemented in frequency domain.

The SI is defined as the index of how similar the three-phase actual current obtained from experiment are compared to the ideal currents from corresponding simulation, and the procedure for the SI calculation is shown in Fig. 5.30.

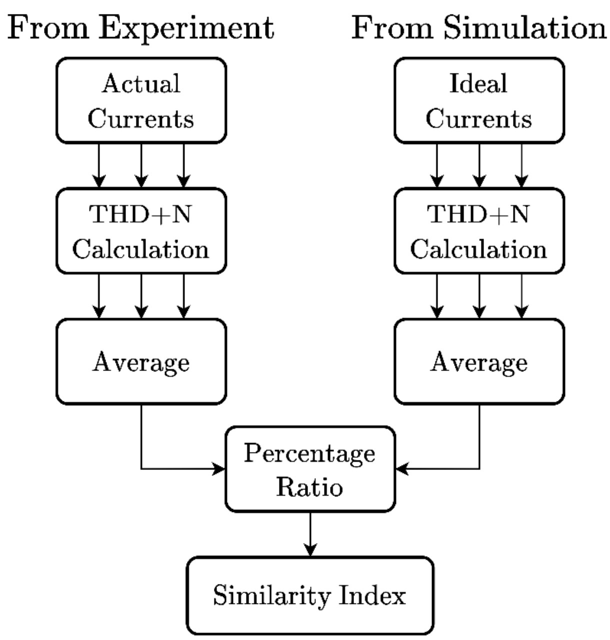

Fig. 5.30 The procedure for the Similarity Index calculation.

The calculation process is shown as follows:

First of all, the $THD + N$ of the three-phase actual currents and the three-phase ideal currents are calculated, and the definition of $THD + N$ can be expressed as:

doi:10.6342/NTU202302551

$$THD + N(i) = \sqrt{\frac{\sum_{n=2}^{\infty} {i_n}^2 + i_{noise}^2}{{i_1}^2}} = \sqrt{\frac{\|i\|^2 - \|i_1\|^2}{\|i_1\|^2}}. \tag{5.4}$$

Next, the $THD + N$ of the three-phase actual currents and the three-phase ideal currents are averaged to obtained the averaged *THD+N* results, which can be shown as:

$$THD + N_{actual} = \frac{THD + N(i_a) + THD + N(i_b) + THD + N(i_c)}{3}, \tag{5.5}$$

$$THD + N_{ideal} = \frac{THD + N(i_{a.ideal}) + THD + N(i_{b.ideal}) + THD + N(i_{c.ideal})}{3}, \tag{5.6}$$

where the $THD + N_{acutal}$ and $THD + N_{ideal}$ are the averaged *THD+N* from experiment and the averaged *THD+N* from simulation, respectively.

Then, the Similarity Index (SI) can be obtained by finding the percentage ratio between the $THD + N_{acutal}$ and $THD + N_{ideal}$. The expression can be shown as:

$$SI = \begin{cases} \frac{THD + N_{acutal}}{THD + N_{ideal}} \cdot 100\%, & for\ THD + N_{ideal} > THD + N_{acutal} \\ \frac{THD + N_{idael}}{THD + N_{actual}} \cdot 100\%, & for\ THD + N_{ideal} < THD + N_{actual} \end{cases}. \tag{5.7}$$

Fig. 5.31 illustrates the diagram of the SI with the aspect of THD+N. It is worth noting that the R-Unbalance scenario with CPIR control achieves the highest SI of 97.33%. On the other hand, the OPF scenario exhibits the greatest improvement from 55.64% to 84.31% since the CPIR control can achieve effective tracking for the dominant second harmonic present in this scenario. However, the ISCF scenario has the lowest similarity index of 64.07%, primarily due to challenges in regulating the switching-related harmonics.

doi:10.6342/NTU202302551

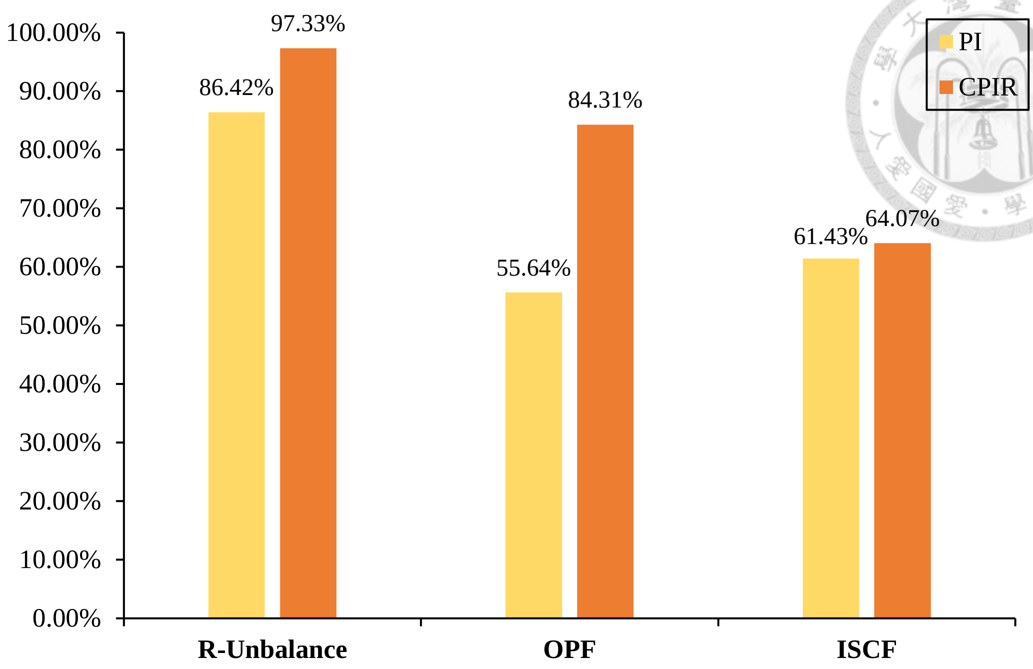

Fig. 5.31 The diagram of the Similarity Index (SI) with the aspect of THD+N.

Lastly, it is evident that the motor emulation exhibits superior performance for the motor under R-Unbalance scenario. As a result, an example of control verification for the motor driver is conducted with the PHIL-based motor test-bench under R-Unbalance scenario in this thesis. The details of the verification can be found in Appendix B, which reveals a substantial reduction in the second harmonic in the dq-axis. This reduction is attributed to the effective current control implemented in the MUT, further demonstrating the capability of the PHIL-based motor test-bench to validate the performance of the MUT.

doi:10.6342/NTU202302551

Chapter 6 Summary and Future Works

6.1 Conclusions and Major Contributions

Power Hardware-in-the-Loop (PHIL) motor emulation is an emerging research area that offers significant advantages over traditional motor test-bench that employ real motors and dynamometers. One of the key advantages of PHIL is its ability to emulate motors under different fault scenarios without the risk of damaging a real motor. Therefore, this thesis focuses on demonstrating the PHIL emulations for Surface Permanent Magnet Synchronous Motors (SPMSM) under three different fault scenarios through computer simulations and real-world experiments. Furthermore, this thesis introduces a novel control method for PHIL current control, resulting in notable improvements in motor emulation performance under fault scenarios. Additionally, Appendix B showcases a control verification for the motor driver by using the PHIL-based test-bench, serving as a compelling example that highlights the capabilities of the PHIL-based test-bench.

The major contributions of this thesis can be summarized as follows:

a. Some brief introductions are provided in this thesis, including the advantages for utilizing Power Hardware-in-the-Loop (PHIL) in motor test-bench, the basic concepts of PHIL, the basic Surface Permanent Magnet Synchronous Motor (SPMSM) model in abc-axis and dq-axis, and the traditional control design.

b. Motor models of the most common fault scenarios, including Resistance Unbalance(R-Unbalance), Open-Phase Fault (OPF), and Inter-Turn Short-Circuit (ISCF) are derived in state-space form so as to utilize the numerical method to calculate the reference currents.

doi:10.6342/NTU202302551

c. A new control method called Coupling-Proportional-Integral-Resonant (CPIR) control is proposed in this thesis. By employing this method, PHIL can achieve zero steady-state error for the negative sequence current without additional notch filters compares to the DSRF control methodology.

d. A 30kW PHIL-based test-bench is implemented in this thesis so as to endure the current stress for the faulty motor emulation. By utilizing the TMS320F28379D MCU from Texas Instrument (TI), the CLA1 is set to calculate the motor model with 312.5kHz, and set the CPU1 to process the ADC interrupt for performing the control routine to obtain the control signals for three-phase inverter with 100kHz.

e. Simulation results are presented to demonstrate the emulation capabilities of the PHIL-based test-bench under different fault scenarios. Moreover, experiment results are provided to verify the feasibility of the CPIR control and assess its overall performance in real-world applications.

doi:10.6342/NTU202302551

6.2 Suggestions for Future Research

In addition to the research conducted in this thesis, several potential future research topics are suggested for further investigation:

a. Advanced Control Methodologies: Develop and utilize advanced control methods, such as model predictive control (MPC), linear–quadratic–Gaussian (LQG) control, or adaptive control, to improve the performance and stability of the PHIL emulation.

b. Fault Diagnosis and Fault-Tolerant Control: Investigate fault diagnosis techniques and develop fault-tolerant control algorithms for motor drivers, then utilizing PHIL-based test-bench to verify the detecting ability of fault diagnosis and performance of fault-tolerant control. This research focuses on the motor driver side. However, it also showcases the ability of emulation a faulty motor for the PHIL.

c. Multi-Physics Integration: Investigate the integration of multiple physical domains, such as thermal, mechanical, or electromagnetic aspects, with the electrical domain in PHIL-based test-bench. This research can provide a comprehensive understanding of the interactions and interdependencies between different physical phenomena and their impact on motor performance.

d. Emulation Optimization: Explore methods for optimizing the Real-Time simulation performance of PHIL, whether through hardware or firmware approaches. These methods may result in improving sensor accuracy, reducing computational requirements, or enhancing the fidelity of the model iteration.

e. PHIL Validation: Develop appropriate strategies for validating the accuracy and reliability of the PHIL-based test-bench, including benchmarking and comparison with the experimental results of real-world motors.

doi:10.6342/NTU202302551

Appendix

A. Field-Oriented Control for Motor Driver

The schematic diagram of Field-Oriented Control (FOC) for implementing speed control in motor driver is illustrated in Fig. A1.

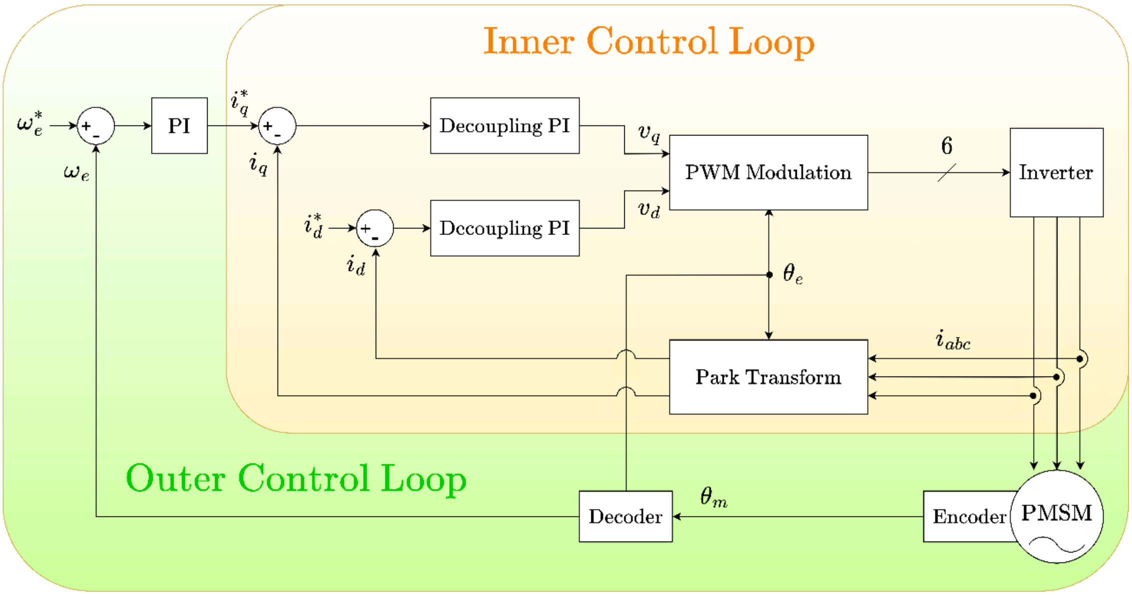

Fig. A1 The schematic diagram of Field-Oriented Control.

It is worth noting that there are two control loop in this structure, namely the inner control loop and outer control loop.

The inner control loop, commonly referred to as the current control loop in motor driving, bears resemblance to the current control loop in PHIL discussed in this thesis. Therefore, the traditional decoupling PI control is widely utilized as the current control method. The design procedure for this is discussed in Section 3.2 , and the only difference is that the control plant is altered from Fig. 3.2 to Fig. 2.3.

For the outer control loop, it is often referred to as the speed control loop for motor driving. The most important concept about this control loop is to design the current controller in the q-axis first, as it forms part of the control plant in speed control loop. Once the q-axis controller is designed, the PI controller can be designed for speed control.

doi:10.6342/NTU202302551

B. Motor Driver Control Verification Example

One of the most important applications for PHIL-based motor test-bench is the control verification for MUT. An example of MUT control verification under R-Unbalance scenario is shown below.

From Fig. B1 and Fig. B2, it is evident that if the motor driver employs the proposed CPIR control in the inner control loop of FOC, the severity of unbalance is significantly reduced, indicating a notable improvement in the performance of the motor driver.

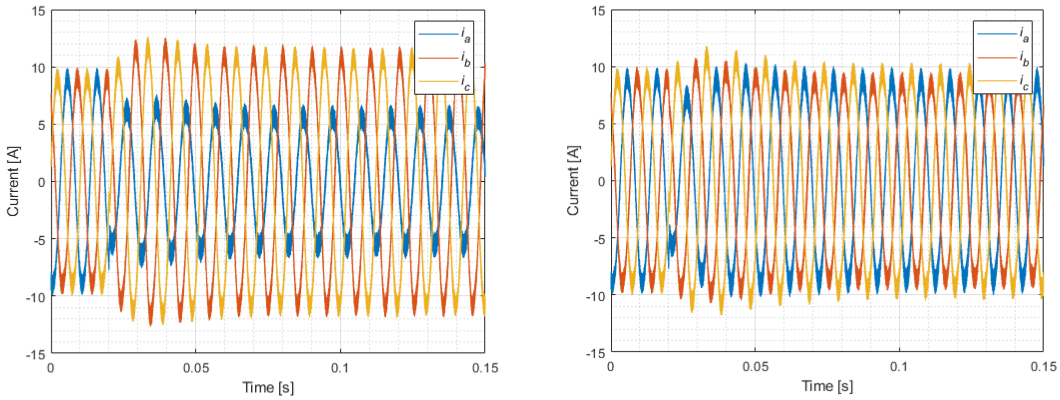

(a) (b)

Fig. B1 The comparison diagram for three-phase currents under R-Unbalance scenario with different current control in MUT (a) PI control (b) CPIR control.

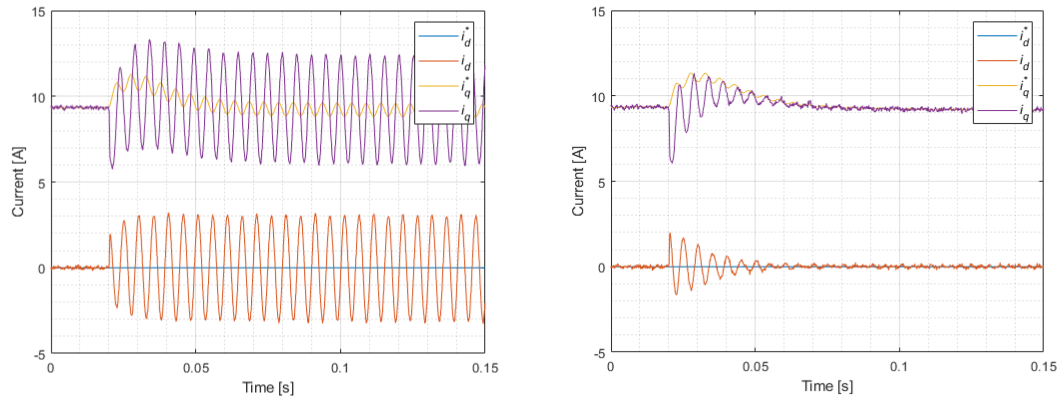

(a) (b)

Fig. B2 The comparison diagram for the dq-axis reference currents and feedback currents under R-Unbalance scenario with different current control in MUT (a) PI control (b) CPIR control.

doi:10.6342/NTU202302551

Reference

[1] Y. Song, R. Cheng, and K. Ma, "Mission profile emulator for permanent magnet synchronous machine based on three-phase power electronic converter," International Power Electronics Conference, Niigata, 2018, pp. 3877-3883.

[2] R. S. Kaarthik, K. S. Amitkumar and P. Pillay, "Emulation of a Permanent-Magnet Synchronous Generator in Real-Time Using Power Hardware-in-the-Loop," in IEEE Transactions on Transportation Electrification, vol. 4, no. 2, pp. 474-482, June 2018, doi: 10.1109/TTE.2017.2778149.

[3] A. Schmitt, M. Gommeringer, C. Rollbuhler, P. Pomnitz, and M. Braun, "A novel modulation scheme for a modular multiphase multilevel converter in a power hardware-in-the-loop emulation system," Annual Conference of the IEEE Industrial Electronics Society, Yokohama, 2015, pp. 001276-001281.

[4] K. Saito and H. Akagi, "A power hardware-in-the-loop-simulation (P-HILS) system using two modular multilevel DSCC converters for a synchronous-motor drive," 2017 IEEE Energy Conversion Congress and Exposition (ECCE), Cincinnati, OH, USA, 2017, pp. 2692-2699, doi: 10.1109/ECCE.2017.8096506.

[5] Y. Song, R. Cheng and K. Ma, "Mission Profile Emulator for Permanent Magnet Synchronous Machine Based on Three-phase Power Electronic Converter," 2018 International Power Electronics Conference (IPEC-Niigata 2018 -ECCE Asia), Niigata, Japan, 2018, pp. 3877-3883, doi: 10.23919/IPEC.2018.8507438.

[6] K. Ma, S. Xia, Y. Qi, X. Cai, Y. Song and F. Blaabjerg, "Power-Electronics-Based Mission Profile Emulation and Test for Electric Machine Drive System—Concepts, Features, and Challenges," in IEEE Transactions on Power Electronics, vol. 37, no. 7, pp. 8526-8542, July 2022, doi: 10.1109/TPEL.2022.3149996.

[7] B. Zhang, H. -N. Chiu and Y. -M. Chen, "Coupling Network State Equation Control For Permanent Magnet Synchronous Motor Emulators," 2021 IEEE International Future Energy Electronics Conference (IFEEC), Taipei, Taiwan, 2021, pp. 1-5, doi: 10.1109/IFEEC53238.2021.9662007.

[8] Y. Luo, M. A. Awal, W. Yu and I. Husain, "FPGA-Based High-Bandwidth Motor Emulator for Interior Permanent Magnet Machine Utilizing SiC Power Converter," in IEEE Journal of Emerging and Selected Topics in Power Electronics, vol. 9, no. 4, pp. 4340-4353, Aug. 2021, doi: 10.1109/JESTPE.2020.3015179.

doi:10.6342/NTU202302551

[9] F. E. Fleming and C. S. Edrington, "Real-Time Emulation of Switched Reluctance Machines via Magnetic Equivalent Circuits," in IEEE Transactions on Industrial Electronics, vol. 63, no. 6, pp. 3366-3376, June 2016, doi: 10.1109/TIE.2016.2521343.

[10] K. Saito and H. Akagi, "A Real-Time Real-Power Emulator of a Medium-Voltage High-Speed Induction Motor Coupled with a Mechanical Load," 2018 IEEE Energy Conversion Congress and Exposition (ECCE), Portland, OR, USA, 2018, pp. 5242-5249, doi: 10.1109/ECCE.2018.8557371.

[11] K. Saito and H. Akagi, "A Real-Time Real-Power Emulator of a Medium-Voltage High-Speed Induction Motor Loaded With a Centrifugal Compressor," in IEEE Transactions on Industry Applications, vol. 55, no. 5, pp. 4821-4833, Sept.-Oct. 2019, doi: 10.1109/TIA.2019.2928498.

[12] K. Saito and H. Akagi, "A Real-Time Real-Power DSCC-Based Emulator Capable of Reproducing Both Bending and Torsional Vibrations of a Motor and Load," 2019 IEEE Energy Conversion Congress and Exposition (ECCE), Baltimore, MD, USA, 2019, pp. 306-312, doi: 10.1109/ECCE.2019.8912884.

[13] K. Saito and H. Akagi, "A Real-Time Real-Power Emulator for a Medium-Voltage High-Speed Electrical Drive: Discussion on Mechanical Vibrations," in IEEE Transactions on Industry Applications, vol. 57, no. 2, pp. 1482-1494, March-April 2021, doi: 10.1109/TIA.2021.3054605.

[14] Y. Rahmoun, P. Winzer, A. Schmitt and H. Hammerer, "Six-Phase PMSM Drive Inverter Testing on a High Performance Power Hardware-in-the-Loop Testbed," 2020 22nd European Conference on Power Electronics and Applications (EPE'20 ECCE Europe), Lyon, France, 2020, pp. P.1-P.10, doi: 10.23919/EPE20ECCEEurope43536.2020.9215638.

[15] K. S. Amitkumar, P. Pillay and J. Bélanger, "An Investigation of Power-Hardware-in-the-Loop- Based Electric Machine Emulation for Driving Inverter Open-Circuit Faults," in IEEE Transactions on Transportation Electrification, vol. 7, no. 1, pp. 170-182, March 2021, doi: 10.1109/TTE.2020.3006720.

[16] Gonzalo Abad (Ed.), "Power Electronics and Electric Drives for Traction Applications," John Wiley and Sons Ltd., Sep. 2016.

[17] X. Ma and C. Bi, "A technology for online parameter identification of permanent magnet synchronous motor," in CES Transactions on Electrical Machines and

doi:10.6342/NTU202302551

Systems,vol.4,no.3, pp. 237-242, Sept. 2020, doi: 10.30941/CESTEMS.2020.00029.

[18] P. Pramod, A. Saha, K. Namburi and R. Mitra, "Modeling, Analysis and Compensation of Resistance Imbalance in Permanent Magnet Synchronous Motor Drives for Mass Manufacturing Applications," 2019 IEEE International Electric Machines & Drives Conference (IEMDC), San Diego, CA, USA, 2019, pp. 1106-1109, doi: 10.1109/IEMDC.2019.8785260.

[19] Zou Xunhao, Shenghua Huang, Qin Zhuqian, Xiaodong Hu and Kan Guangqiang, "A control method for permanent-magnet synchronous motor with unbalanced cable resistor," 2015 6th International Conference on Power Electronics Systems and Applications (PESA), Hong Kong,2015, pp. 1-3, doi: 10.1109/PESA.2015.7398921.

[20] J. C. Das, " Understanding Symmetrical Components for Power System Modeling," Wiley-IEEE Press., Jan. 2017.

[21] W. Li, P. Song, Q. Li, Z. Li and N. C. Kar, "Open-Phase Fault Modeling for Dual Three-Phase PMSM Using Vector Space Decomposition and Negative Sequence Components," in IEEE Transactions on Magnetics, vol. 58, no. 8, pp. 1-6, Aug. 2022, Art no. 8204106, doi: 10.1109/TMAG.2022.3168780.

[22] W. Xu, O. M. Elbabo Mohammed, Y. Liu and M. R. Islam, "Negative Sequence Voltage Compensating for Unbalanced Standalone Brushless Doubly-Fed Induction Generator," in IEEE Transactions on Power Electronics, vol. 35, no. 1, pp. 667-680, Jan. 2020, doi: 10.1109/TPEL.2019.2912820.

[23] R. A. Vainshtein, N. V. Kolomiets and V. V. Shestakova, "The impact of load, comprising asynchronous motors, on the negative-sequence currents in the generator circuit in unbalanced conditions," 2016 2nd International Conference on Industrial Engineering, Applications and Manufacturing (ICIEAM), Chelyabinsk, Russia, 2016, pp. 1-4, doi: 10.1109/ICIEAM.2016.7911478.

[24] A. Khlaief, M. Boussak and A. Châari, "A real-time open phase faults detection for IPMSM drives based on Discrete Fourier Transform phase analysis," 2013 International Conference on Electrical Engineering and Software Applications, Hammamet, Tunisia, 2013, pp. 1-6, doi: 10.1109/ICEESA.2013.6578436.

[25] X. Zhou, J. Sun, H. Li and X. Song, "High Performance Three-Phase PMSM Open-Phase Fault-Tolerant Method Based on Reference Frame Transformation," in IEEE Transactions on Industrial Electronics, vol. 66, no. 10, pp. 7571-7580, Oct. 2019, doi: 10.1109/TIE.2018.2877197.

doi:10.6342/NTU202302551

[26] Y. Qi, E. Bostanci, M. Zafarani and B. Akin, "Severity Estimation of Interturn Short Circuit Fault for PMSM," in IEEE Transactions on Industrial Electronics, vol. 66, no. 9, pp. 7260-7269, Sept. 2019, doi: 10.1109/TIE.2018.2879281.

[27] S. -T. Lee and J. Hur, "Simplified Equivalent Model of PMSM With Inter-Turn Fault," in IEEE Transactions on Industry Applications, vol. 55, no. 3, pp. 2629-2636, May-June 2019, doi: 10.1109/TIA.2019.2897269.

[28] B. -G. Gu, "Study of IPMSM Interturn Faults Part I: Development and Analysis of Models With Series and Parallel Winding Connections," in IEEE Transactions on Power Electronics, vol. 31, no. 8, pp. 5931-5943, Aug. 2016, doi: 10.1109/TPEL.2015.2496142.

[29] L. Romeral, J. C. Urresty, J. -R. Riba Ruiz and A. Garcia Espinosa, "Modeling of Surface-Mounted Permanent Magnet Synchronous Motors With Stator Winding Interturn Faults," in IEEE Transactions on Industrial Electronics, vol. 58, no. 5, pp. 1576-1585, May 2011, doi: 10.1109/TIE.2010.2062480.

[30] X. Liu, W. Miao, Q. Xu, L. Cao, C. Liu and P. W. T. Pong, "Inter-Turn Short-Circuit Fault Detection Approach for Permanent Magnet Synchronous Machines Through Stray Magnetic Field Sensing," in IEEE Sensors Journal, vol. 19, no. 18, pp. 7884-7895, 15 Sept.15, 2019, doi: 10.1109/JSEN.2019.2918018.

[31] I. Jeong, B. J. Hyon and K. Nam, "Dynamic Modeling and Control for SPMSMs With Internal Turn Short Fault," in IEEE Transactions on Power Electronics, vol. 28, no. 7, pp. 3495-3508, July 2013, doi: 10.1109/TPEL.2012.2222049.

[32] B. -G. Gu, J. -H. Choi and I. -S. Jung, "Development and Analysis of Interturn Short Fault Model of PMSMs With Series and Parallel Winding Connections," in IEEE Transactions on Power Electronics, vol. 29, no. 4, pp. 2016-2026, April 2014, doi: 10.1109/TPEL.2013.2265400.

[33] Y. Qin, G. J. Li, C. Jia and P. McKeever, "PWM Voltage-based Modeling for PM Machines with Inter-Turn Short Circuit Fault Considering the Effect of Drives," in IEEE Transactions on Industrial Electronics, doi: 10.1109/TIE.2022.3229357.

[34] Richard L. Burden, J. Douglas Faires and Annette M. Burden, " Numerical Analysis," Cengage Learning., Nov. 2015.

[35] Snehashish Chakraverty, Nisha Mahato, Perumandla Karunakar and Tharasi Dilleswar Rao, "Advanced Numerical and Semi-Analytical Methods for Differential Equations," Wiley Telecom., Apr. 2019.

doi:10.6342/NTU202302551

[36] T. M. Rowan and R. J. Kerkman, "A New Synchronous Current Regulator and an Analysis of Current-Regulated PWM Inverters," in IEEE Transactions on Industry Applications, vol. IA-22, no. 4, pp. 678-690, July 1986, doi: 10.1109/TIA.1986.4504778.

[37] K. S. Amitkumar, R. S. Kaarthik and P. Pillay, "A Versatile Power-Hardware-in-the-Loop-Based Emulator for Rapid Testing of Transportation Electric Drives," in IEEE Transactions on Transportation Electrification, vol. 4, no. 4, pp. 901-911, Dec. 2018, doi: 10.1109/TTE.2018.2857216.

[38] A. H. Kadam and S. S. Williamson, "Single Loop Control of a Common DC-Bus-Configured Traction Motor Emulator Using State Feedback Linearization Method," 2021 IEEE Southern Power Electronics Conference (SPEC), Kigali, Rwanda, 2021, pp. 1-6, doi: 10.1109/SPEC52827.2021.9709486.

[39] S. Grubic, B. Amlang, W. Schumacher and A. Wenzel, "A High-Performance Electronic Hardware-in-the-Loop Drive–Load Simulation Using a Linear Inverter (LinVerter)," in IEEE Transactions on Industrial Electronics, vol. 57, no. 4, pp. 1208-1216, April 2010, doi: 10.1109/TIE.2009.2037656.

[40] S. Lentijo, S. D'Arco and A. Monti, "Comparing the Dynamic Performances of Power Hardware-in-the-Loop Interfaces," in IEEE Transactions on Industrial Electronics, vol. 57, no. 4, pp. 1195-1207, April 2010, doi: 10.1109/TIE.2009.2027246.

[41] A. H. Kadam, R. Menon and S. S. Williamson, "A novel bidirectional three-phase AC-DC/DC-AC converter for PMSM virtual machine system with common DC bus," 2018 IEEE Applied Power Electronics Conference and Exposition (APEC), San Antonio, TX, USA, 2018, pp. 1944-1951, doi: 10.1109/APEC.2018.8341284.

[42] Jong-Woo Choi and S. -K. Sul, "Fast current controller in three-phase AC/DC boost converter using d-q axis crosscoupling," in IEEE Transactions on Power Electronics, vol. 13, no. 1, pp. 179-185, Jan. 1998, doi: 10.1109/63.654973.

[43] G. Feng, C. Lai and N. C. Kar, "Speed Harmonic Based Decoupled Torque Ripple Minimization Control for Permanent Magnet Synchronous Machine With Minimized Loss," in IEEE Transactions on Energy Conversion, vol. 35, no. 4, pp. 1796-1805, Dec. 2020, doi: 10.1109/TEC.2020.2992487.

[44] K. Günther, F. Bendrat and C. Sourkounis, "Analysis of optimization Strategies for Grid-Side Converter Control during Grid Faults using DSRF Control," 2019

doi:10.6342/NTU202302551

Fourteenth International Conference on Ecological Vehicles and Renewable Energies (EVER), Monte-Carlo, Monaco, 2019, pp. 1-6, doi: 10.1109/EVER.2019.8813513.

[45] S. Zhou, J. Liu, L. Zhou and H. She, "Dual sequence current controller without current sequence decomposition implemented on DSRF for unbalanced grid voltage conditions," 2014 IEEE Energy Conversion Congress and Exposition (ECCE), Pittsburgh, PA, USA, 2014, pp. 60-67, doi: 10.1109/ECCE.2014.6953376.

[46] X. Du, S. Gu, G. Wang, P. Sun, H. -M. Tai and Y. Ji, "A simple current control method for three-phase VSC in DSRF under unbalanced grid condition," IECON 2017 - 43rd Annual Conference of the IEEE Industrial Electronics Society, Beijing, China, 2017, pp. 6841-6846, doi: 10.1109/IECON.2017.8217195.

[47] R. Kabiri, D. G. Holmes and B. P. McGrath, "Double synchronous frame current regulation of distributed generation systems under unbalanced voltage conditions without sequence current separation," 2015 IEEE Applied Power Electronics Conference and Exposition (APEC), Charlotte, NC, USA, 2015, pp. 1822-1829, doi: 10.1109/APEC.2015.7104594.

[48] L. B. Larumbe, Z. Qin and P. Bauer, "On the Importance of Tracking the Negative-Sequence Phase-Angle in Three-Phase Inverters with Double Synchronous Reference Frame Current Control," 2020 IEEE 29th International Symposium on Industrial Electronics (ISIE), Delft, Netherlands, 2020, pp. 1284-1289, doi: 10.1109/ISIE45063.2020.9152442.

[49] M. Schubert, W. -K. Lee and B. -Y. Ooi, "Quantization and Sampling Effects in Fast Digitally Controlled Switch-Mode DC/DC Buck Converters," 2021 IEEE Industrial Electronics and Applications Conference (IEACon), Penang, Malaysia, 2021, pp. 56-61, doi: 10.1109/IEACon51066.2021.9654272.

[50] M. A. Al-Alaoui, "Novel stable higher order s-to-z transforms," in IEEE Transactions on Circuits and Systems I: Fundamental Theory and Applications, vol. 48, no. 11, pp. 1326-1329, Nov. 2001, doi: 10.1109/81.964421.

[51] T. -B. Deng, S. Chivapreecha and K. Dejhan, "Unified Pascal Matrix for First-Order s-z Domain Transformations," in IEEE Transactions on Signal Processing, vol. 57, no. 6, pp. 2130-2139, June 2009, doi: 10.1109/TSP.2009.2013895.

doi:10.6342/NTU202302551